

Regression of Functions by Quantum Neural Networks Circuits

Fernando M. de Paula Neto^{1*}, Lucas dos Reis Silva¹,
Paulo S. G. de Mattos Neto¹, Felipe F. Fanchini^{2,3}

¹*Center of Informatics, Federal University of Pernambuco - UFPE, Av. Jorn. Aníbal Fernandes, Recife, 50.740-560, Pernambuco, Brazil.

²Department of Physics and Meteorology, São Paulo State University - UNESP, Av. Eng. Luiz Edmundo Carrijo Coube, Bauru, 17033-360, São Paulo, Brazil.

³QuaTI - Quantum Technology & Information, Major José Inácio Street, São Carlos, 13560-161, São Paulo, Brazil.

*Corresponding author(s). E-mail(s): fernando@cin.ufpe.br;
Contributing authors: lsr5@cin.ufpe.br; pgsmn@cin.ufpe.br;
felipe.fanchini@unesp.br;

Abstract

The performance of quantum neural network models depends strongly on architectural decisions, including circuit depth, placement of parametrized operations, and data-encoding strategies. Selecting an effective architecture is challenging and closely related to the classical difficulty of choosing suitable neural-network topologies, which is computationally hard. This work investigates automated quantum-circuit construction for regression tasks and introduces a genetic-algorithm framework that discovers Reduced Regressor QNN architectures. The approach explores depth, parametrized gate configurations, and flexible data re-uploading patterns, formulating the construction of quantum regressors as an optimization process. The discovered circuits are evaluated against seventeen classical regression models on twenty-two nonlinear benchmark functions and four analytical functions. Although classical methods often achieve comparable results, they typically require far more parameters, whereas the evolved quantum models remain compact while providing competitive performance. We further analyze dataset complexity using twelve structural descriptors and show, across five increasingly challenging meta-learning scenarios, that these measures can reliably predict which quantum architecture will perform best. The results

demonstrate perfect or near-perfect predictive accuracy in several scenarios, indicating that complexity metrics offer powerful and compact representations of dataset structure and can effectively guide automated model selection. Overall, this study provides a principled basis for meta-learning-driven quantum architecture design and advances the understanding of how quantum models behave in regression settings—a topic that has received limited exploration in prior work. These findings pave the way for more systematic and theoretically grounded approaches to quantum regression.

Keywords: Quantum Neural Networks, Genetic Algorithms, Metalearning, Regression

1 Introduction

Quantum computing promises algorithmic speed-ups for problems that are conjectured to be intractable for classical computation. A landmark example is Shor’s polynomial-time quantum algorithm for integer factorization and discrete logarithms [1]. Beyond algorithmic constructions, experimental demonstrations of *quantum supremacy*—including boson sampling and instantaneous quantum polynomial-time (IQP) circuits—have shown that even shallow quantum devices can generate probability distributions that cannot be efficiently reproduced by classical machines unless the polynomial hierarchy collapses [2]. These results underscore the intrinsic expressive richness of quantum models and their potential to outperform classical methods in specific computational regimes.

Motivated by these developments, the field of *quantum machine learning* (QML) seeks to combine quantum computation with modern machine-learning methodologies [3]. Quantum learning models exploit high-dimensional Hilbert spaces, controllable entanglement, and quantum interference to construct expressive hypothesis classes that can be difficult to emulate classically [4]. A prominent line of research has focused on quantum kernel methods [5], which map classical data into quantum-enhanced feature spaces where linear classifiers can achieve separations that are provably hard for classical models. In this direction, Liu *et al.* [6] construct a classification task for which a quantum kernel method, implemented via efficiently parameterized unitary circuits and requiring only classical data access, achieves an end-to-end quantum advantage under standard cryptographic assumptions.

More recently, the scope of QML has expanded beyond kernel-based approaches toward more general parametrized quantum models. In particular, quantum neural networks (QNNs) and hybrid quantum–classical architectures have been proposed as flexible learning frameworks capable of achieving large effective dimension and improved trainability compared to classical neural networks [7]. These models have been successfully applied to a wide range of learning paradigms [8–10].

Beyond classification, QML techniques have also been explored in structured learning settings and real-world applications, such as efficient quantum convolutional neural networks designed under hardware constraints [11], long-term time-series forecasting [12], and financial modeling for institutional algorithmic trading [13]. At

the methodological level, recent advances in quantum feature engineering, including digitized counterdiabatic protocols [14] and quenched quantum feature maps [15], further highlight the growing interest in designing expressive yet trainable quantum embeddings. Collectively, these works illustrate the rapid evolution of QML from theoretically motivated kernel methods toward versatile, application-driven quantum learning architectures.

QNNs can be naturally viewed as instances of *variational quantum circuits* (VQCs) [16]. These hybrid quantum-classical models employ parameterized quantum gates whose trainable weights are optimized to minimize a task-dependent loss function. Several QNN architectures have been proposed in the literature, ranging from early perceptron-inspired models [17, 18], tensor-network embeddings [19], and quantum convolutional networks [20], to recurrent and reuploading-based designs [21]. Recently, a study demonstrated the universality of quantum neural networks of the random type [22], and other study demonstrates that deep data re-uploading QNNs can approximate arbitrary continuous functions, and that the attainable expressive power heavily depends on the structure of the measurement operators and the entangling topology [23]. There are also important analyses in terms of the learning capacity of intelligent quantum models [24–26]. Some studies have demonstrated the ability of quantum neural networks to solve nonlinear problems in classification tasks [27–29].

The performance, trainability, and robustness of QNNs depend critically on the chosen variational ansatz. Architectural factors such as gate placement, entanglement patterns, circuit depth, and data-encoding strategies play central roles in determining the expressive capacity and optimization landscape of the model. Indeed, the representational power of parameterized quantum circuits is tightly constrained by the interplay between feature maps and circuit topology [2, 30], and suboptimal architectural choices may lead to barren plateaus [31], excessive depth requirements, or undesirable sensitivity to device noise. Consequently, the principled design of QNN architectures—especially those intended for regression—remains a challenging open problem and a key motivation for automated circuit-synthesis approaches.

This has motivated the rapidly growing field of *Quantum Architecture Search* (QAS), which aims to automatically discover quantum circuit structures tailored to specific learning tasks. Approaches based on evolutionary algorithms, reinforcement learning, neural predictors, and differentiable search have shown that automatically synthesized circuits can outperform expert-crafted ansätze while using fewer parameters and shallower depth [32–34].

These observations highlight a fundamental open challenge: identifying circuit architectures that are expressive enough for the target learning task while respecting constraints on depth, noise resilience, and hardware feasibility. This challenge is analogous to the classical NP-complete problem of selecting optimal multilayer perceptron topologies. Previous work has already explored optimal constructions of quantum circuits for specific tasks, such as the preparation of quantum states and the synthesis of arbitrary unitaries [35]. A recent study performs systematic comparisons between quantum learning models and classical classifiers [28]. Consequently, there is a compelling need for automated, data-driven, and hardware-adapted methodologies for synthesizing variational quantum circuits suitable for regression tasks.

In this work, we address this challenge by conducting a systematic comparative analysis between automatically synthesized quantum circuits and three widely used variational ansatz families in the QML literature—*Strongly Entangling Layers*, *Simplified Two Design*, and *Basic Entangler Layers*. We propose a genetic-algorithm-based framework for constructing Reduced Regressor Quantum Neural Network (RRQNN) architectures and treat quantum circuits as design objects whose topology, depth, and data-reuploading patterns must be synthesized rather than manually specified. This approach enables fine-grained exploration of quantum regressors under stringent depth constraints while making their architectural design responsive to the complexity of the underlying function.

Beyond circuit synthesis, we also address the orthogonal yet fundamental question of *model selection for quantum regressors*: given a dataset, which quantum architecture is likely to achieve the best performance? While prior works in Quantum Architecture Search (QAS) have explored architecture optimization using evolutionary search [32], differentiable search [36], reinforcement learning [37], or meta-trained predictors [33], these methods primarily aim at efficiently discovering a single circuit structure. Similarly, QML research on meta-learning has focused on accelerating training or improving initialization [38], but not on predicting the most suitable quantum model for a given regression task. In contrast, our work integrates meta-feature analysis into the QML pipeline and demonstrates, for the first time in quantum regression, that structural descriptors of the dataset can be used to predict—with optimal accuracy in our experiments—which among several competing quantum circuit families (including the GA-generated RRQNNs and the three standard ansätze) yields the best performance. This combination of automated circuit synthesis and meta-learning-based model selection differentiates our approach from existing QAS and QML methodologies.

The paper is structured to progressively introduce the proposed methodology, its experimental validation, and the resulting insights. Section 2 provides the necessary background on quantum computing, while Section 3 introduces quantum neural networks, focusing on the concepts required to contextualize the learning models studied in this work. Section 4 presents the regression complexity measures employed as meta-features, which form the basis of the subsequent meta-learning analysis. The proposed Reduced Regressor Quantum Neural Network (RRQNN) and the genetic-algorithm-based architecture search are detailed in Section 5, including the chromosome encoding and the deterministic mapping to quantum circuits. The experimental protocol is described in Section 6. Finally, Section 7 discusses the empirical results, statistical analyses, and limitations of the study, while Section 8 summarizes the main findings and outlines directions for future work.

2 Quantum Computing: Background and Notation

This section provides only the minimum background required for readers from the machine learning community; more comprehensive treatments of quantum computing fundamentals can be found in standard quantum computing textbooks [39].

2.1 Quantum Bits

In quantum information theory, the fundamental unit of data is the quantum bit (qubit). A qubit is formally represented as a normalized vector in the complex Hilbert space \mathbb{C}^2 , i.e., a two-dimensional complex vector space. Unlike classical bits, which assume deterministic states, a qubit can exist in a coherent superposition of the computational basis states $|0\rangle$ and $|1\rangle$. Mathematically, any pure qubit state $|\psi\rangle$ can be expressed as a linear combination of the basis vectors, as shown in Equation 1:

$$|\psi\rangle = \alpha|0\rangle + \beta|1\rangle, \text{ where } \alpha, \beta \in \mathbb{C} \text{ and } |\alpha|^2 + |\beta|^2 = 1. \quad (1)$$

The complex amplitudes α and β encode probabilistic information about the outcome of a projective measurement in the computational basis. The probability of obtaining $|0\rangle$ is $|\alpha|^2$, while the probability of measuring $|1\rangle$ is $|\beta|^2$. Throughout this manuscript, i denotes the imaginary unit, such that $i^2 = -1$. Composite quantum systems are described via the tensor product operation, denoted by \otimes . For two qubits $|a\rangle$ and $|b\rangle$, the joint system is given by $|\mathbf{g}\rangle = |a\rangle \otimes |b\rangle$, often denoted succinctly as $|ab\rangle$. If $|a\rangle = \alpha_1|0\rangle + \beta_1|1\rangle$ and $|b\rangle = \alpha_2|0\rangle + \beta_2|1\rangle$, then the composite state expands to:

$$|ab\rangle = \alpha_1\alpha_2|00\rangle + \alpha_1\beta_2|01\rangle + \beta_1\alpha_2|10\rangle + \beta_1\beta_2|11\rangle. \quad (2)$$

In the general case of states $|\mathbf{p}\rangle \in \mathbb{C}^{2^n}$ and $|\mathbf{q}\rangle \in \mathbb{C}^{2^m}$, the tensor product $|\mathbf{p}\mathbf{q}\rangle = |\mathbf{p}\rangle \otimes |\mathbf{q}\rangle$ produces a vector in $\mathbb{C}^{2^{n+m}}$, as detailed in Equation 3.

$$\begin{bmatrix} \alpha_1 \\ \alpha_2 \\ \dots \\ \alpha_{2^n} \end{bmatrix} \otimes \begin{bmatrix} \beta_1 \\ \beta_2 \\ \dots \\ \beta_{2^m} \end{bmatrix} = \begin{bmatrix} \alpha_1 \begin{bmatrix} \beta_1 \\ \beta_2 \\ \dots \\ \beta_{2^m} \end{bmatrix} \\ \alpha_2 \begin{bmatrix} \beta_1 \\ \beta_2 \\ \dots \\ \beta_{2^m} \end{bmatrix} \\ \dots \\ \alpha_{2^n} \begin{bmatrix} \beta_1 \\ \beta_2 \\ \dots \\ \beta_{2^m} \end{bmatrix} \end{bmatrix} = \begin{bmatrix} \alpha_1\beta_1 \\ \alpha_1\beta_2 \\ \dots \\ \alpha_1\beta_{2^m} \\ \alpha_2\beta_1 \\ \alpha_2\beta_2 \\ \dots \\ \alpha_2\beta_{2^m} \\ \dots \\ \alpha_{2^n}\beta_1 \\ \alpha_{2^n}\beta_2 \\ \dots \\ \alpha_{2^n}\beta_{2^m} \end{bmatrix}. \quad (3)$$

This tensor construction is essential for representing multi-qubit systems and modeling quantum entanglement. A state $|\psi\rangle \in Q \otimes R$ is entangled if it cannot be factorized as $|\psi\rangle \neq |q\rangle \otimes |r\rangle$ with $|q\rangle \in Q$ and $|r\rangle \in R$. Entanglement constitutes one of the fundamental non-classical features enabling quantum computational advantage.

2.2 Quantum Operators

Quantum evolution is governed by unitary transformations, known as quantum operators or quantum gates. An operator \mathbf{U} acting on n qubits is a unitary matrix of

dimension $2^n \times 2^n$, satisfying $\mathbf{U}^\dagger \mathbf{U} = \mathbf{I}$. For a single qubit, common elementary gates include the Identity (**I**), Pauli-X (**X**), and Hadamard (**H**) operators, defined as follows:

$$\mathbf{I} = \begin{bmatrix} 1 & 0 \\ 0 & 1 \end{bmatrix}; \mathbf{I}|0\rangle = |0\rangle; \mathbf{I}|1\rangle = |1\rangle; \mathbf{X} = \begin{bmatrix} 0 & 1 \\ 1 & 0 \end{bmatrix}; \mathbf{X}|0\rangle = |1\rangle; \mathbf{X}|1\rangle = |0\rangle \quad (4)$$

$$\mathbf{H} = \frac{1}{\sqrt{2}} \begin{bmatrix} 1 & 1 \\ 1 & -1 \end{bmatrix}; \mathbf{H}|0\rangle = 1/\sqrt{2}(|0\rangle + |1\rangle); \mathbf{H}|1\rangle = 1/\sqrt{2}(|0\rangle - |1\rangle) \quad (5)$$

While **I** leaves the qubit invariant, **X** performs a bit-flip operation analogous to the classical NOT gate. The Hadamard gate **H** induces an equal superposition of $|0\rangle$ and $|1\rangle$, playing a central role in quantum parallelism. More general single-qubit rotations are represented by the rotation operators **R_x**, **R_y**, and **R_z**:

$$\mathbf{R}_x(\theta) = \begin{pmatrix} \cos(\theta/2) & -i \cdot \sin(\theta/2) \\ -i \cdot \sin(\theta/2) & \cos(\theta/2) \end{pmatrix}, \quad (6)$$

$$\mathbf{R}_y(\theta) = \begin{pmatrix} \cos(\theta/2) & -\sin(\theta/2) \\ \sin(\theta/2) & \cos(\theta/2) \end{pmatrix}, \quad (7)$$

$$\mathbf{R}_z(\theta) = \begin{pmatrix} e^{-i \cdot \theta/2} & 0 \\ 0 & e^{i \cdot \theta/2} \end{pmatrix}, \quad (8)$$

$$\mathbf{U}(\theta, \beta, \gamma) = \begin{pmatrix} \cos(\theta/2) & -e^{i \cdot \gamma} \cdot \sin(\theta) \\ e^{i \cdot \beta} \sin(\theta) & e^{i \cdot (\beta + \gamma)} \cos(\theta) \end{pmatrix}. \quad (9)$$

Any arbitrary single-qubit unitary operator can be decomposed as a product of these rotation gates, $\mathbf{U} = \mathbf{R}_z(\alpha)\mathbf{R}_y(\beta)\mathbf{R}_z(\gamma)$, or equivalently expressed in the general parametric form shown in Equation 10:

$$\mathbf{U}(\theta, \beta, \gamma) = \begin{pmatrix} \cos(\theta/2) & -e^{i \cdot \gamma} \cdot \sin(\theta) \\ e^{i \cdot \beta} \sin(\theta) & e^{i \cdot (\beta + \gamma)} \cos(\theta) \end{pmatrix}. \quad (10)$$

Multi-qubit interactions are typically introduced via controlled operations. The controlled-NOT (CNOT) gate, for instance, acts on two qubits—a control and a target—and applies **X** to the target if and only if the control qubit is in the $|1\rangle$ state:

$$\mathbf{CNOT} = \begin{bmatrix} 1 & 0 & 0 & 0 \\ 0 & 1 & 0 & 0 \\ 0 & 0 & 0 & 1 \\ 0 & 0 & 1 & 0 \end{bmatrix}; \begin{aligned} \mathbf{CNOT}|00\rangle &= |00\rangle \\ \mathbf{CNOT}|01\rangle &= |01\rangle \\ \mathbf{CNOT}|10\rangle &= |11\rangle \\ \mathbf{CNOT}|11\rangle &= |10\rangle \end{aligned} \quad (11)$$

This construction generalizes to controlled-**U** gates, where any unitary transformation **U** can be applied conditionally on the state of one or more control qubits. The set **H**, **R_z**, **CNOT** forms a universal gate set capable of implementing any quantum computation [39].

2.3 Quantum Measurement

Quantum measurement constitutes a non-unitary and irreversible process that projects a superposed state into one of the basis states of the measurement operator. Given a single-qubit state $|\psi\rangle = \alpha|0\rangle + \beta|1\rangle$, a projective measurement in the computational basis collapses the state to $|0\rangle$ with probability $|\alpha|^2$ or to $|1\rangle$ with probability $|\beta|^2$. For a general multi-qubit state $|\mathbf{g}\rangle$, the probability of observing a configuration $|\phi\rangle$ is given by $|\langle\phi|\mathbf{g}\rangle|^2$. The expectation value of an observable \mathbf{Z} in the state $|\psi\rangle$ is defined as:

$$\langle Z \rangle = \langle \psi | \mathbf{Z} | \psi \rangle, \quad \mathbf{Z} = \begin{bmatrix} 1 & 0 \\ 0 & -1 \end{bmatrix}, \quad (12)$$

yielding real outcomes in the interval $[-1, 1]$. Measurement plays a crucial role in extracting classical information from quantum systems and forms the interface between quantum and classical computation layers.

2.4 Quantum Circuits

Quantum algorithms are typically modeled as quantum circuits, which provide a graphical abstraction of the sequence of quantum operations applied to a register of qubits. In this representation, qubits are depicted as horizontal wires, and gates correspond to unitary transformations applied along these wires, with computation proceeding from left to right. An example of a circuit containing a **CNOT** gate, a controlled **R_z** rotation, and a single-qubit **R_x** rotation is illustrated in Figure 1.

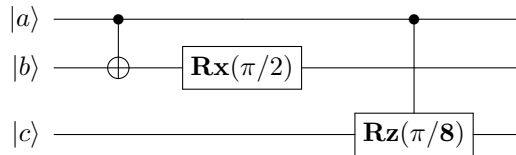


Fig. 1 An example of quantum circuit with one **CNOT** operator and two rotation gates, **R_x** and **R_z**, one of them being controlled (controlled rotation).

3 Quantum Neural Networks

As stated in [40], modern quantum neural networks combine variational quantum circuits with classical optimization techniques, allowing for efficient training of small quantum circuits. The variational quantum circuit, also known as the parametric quantum circuit (PQC), was introduced in [16] as a strategy to construct quantum circuits with a limited number of gates, or equivalently, low circuit depth. A PQC typically consists of two main stages: an information encoding stage and a parameterized operation stage. Figure 2 illustrates a general representation of a PQC, in which a layer dedicated to loading input data, called Input Embedding, as well as one (or n) layer for loading circuit parameters, called Parametric Layer. Quantum circuits with tunable parameters have demonstrated their capability to solve complex real-world

problems [18, 27, 29, 41]. As discussed in [42], the expressive power of a parameterized circuit—namely, the number of functions it can approximate—increases as the number of repeated layers grows. Furthermore, the results in [43] show that the entanglement difference between layers tends to converge as the number of parameterized layers increases, highlighting a form of structural saturation in deep PQCs.

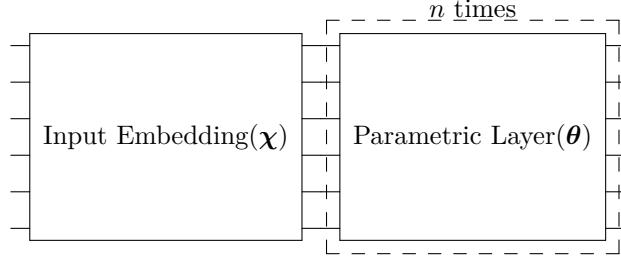


Fig. 2 Traditional generic architecture of a parametric quantum circuit where the Parametric Layer can be repeated n times.

3.1 Encoding Classical Data

There are several strategies for **encoding classical data** into quantum states [44]. A common strategy for loading a classical input vector $\mathbf{x} = (x_1, \dots, x_d) \in \mathbb{R}^d$ into a variational quantum circuit is to encode each component x_j into the rotation angle of a single-qubit gate. More precisely, one selects a rotation operator $R_\alpha(\cdot)$, with $\alpha \in \{x, y, z\}$, and applies these gates *in parallel* to d qubits, each receiving the information of one coordinate of \mathbf{x} .

A single-qubit rotation around axis α is defined as

$$R_\alpha(\theta) = \exp\left(-\frac{i\theta}{2} \sigma_\alpha\right), \quad \alpha \in \{x, y, z\}, \quad (13)$$

where σ_α denotes the corresponding Pauli operator. Thus, a general phase-embedding unitary takes the form

$$U_{\text{embed}}(\mathbf{x}) = \bigotimes_{j=1}^d R_\alpha(\phi_j(x_j)), \quad (14)$$

where $\phi_j : \mathbb{R} \rightarrow \mathbb{R}$ is typically a linear function, such as

$$\phi_j(x_j) = \omega_j x_j, \quad (15)$$

with ω_j being a frequency or scaling hyperparameter.

The resulting quantum state after embedding is

$$|\psi(\mathbf{x})\rangle = U_{\text{embed}}(\mathbf{x}) |0\rangle^{\otimes d} = \left(\bigotimes_{j=1}^d R_\alpha(\phi_j(x_j)) \right) |0\rangle^{\otimes d}. \quad (16)$$

When encoding through Z -axis rotations, we have explicitly

$$R_z(\theta) = \exp\left(-\frac{i\theta}{2}Z\right) = \begin{pmatrix} e^{-i\theta/2} & 0 \\ 0 & e^{i\theta/2} \end{pmatrix}, \quad (17)$$

and therefore the corresponding phase embedding is

$$U_{\text{embed}}^{(Z)}(\mathbf{x}) = \bigotimes_{j=1}^d R_z(\omega_j x_j). \quad (18)$$

This type of encoding through parallel single-qubit rotations is widely used in variational quantum neural networks and data reuploading models due to its simplicity and because it introduces controlled phase contributions that are later processed by trainable variational blocks. In practice, phase rotations such as R_z are most meaningful once the quantum states have been brought into superposition—typically via the application of Hadamard gates—since global or relative phases become observable only in the presence of interference. Under this condition, R_z -based embeddings effectively modulate relative phases across computational basis components, which are subsequently transformed into measurable amplitudes by entangling and variational layers. A detailed discussion of such encoding strategies in regression-oriented quantum neural networks can be found in Panadero *et al.* [45], where the authors show how phase embeddings contribute to the Fourier expressive structure of QNNs.

There are some works that demonstrate the effect of repeatedly loading data into the circuit. This routine is called *reuploading*. In [21], a reuploading approach shows the universality of the proposed quantum classifier. In [42], it is possible to verify that variational quantum circuits with reuploading can be represented as Fourier series, where the more repetitions of data applied to variational quantum circuits, the closer the circuit function is to its true value.

3.2 Parametric Layers

In the context of parametric quantum circuits, any composition of quantum gates containing tunable rotation parameters can serve as a valid architecture. To train such circuits, it is essential to define a loss function that quantifies the prediction error for a given input and parameter configuration. This loss function guides a classical optimization algorithm, which iteratively updates the circuit parameters to minimize the loss value, thereby improving the model's predictive performance. Figure 3 illustrates a generic overview of the parameter optimization process in a variational quantum circuit.

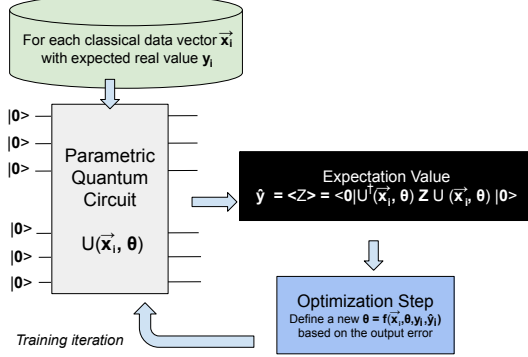


Fig. 3 Learning process of a parametric quantum circuit. The classical optimizer iteratively updates the parameters θ based on the feedback from quantum measurements.

3.2.1 Strongly Entangling Layers

Among the most widely used variational templates in quantum machine learning is the *Strongly Entangling Layers* architecture, which provides an expressive yet hardware-efficient structure for parametrized quantum circuits [46]. Each layer consists of two components arranged sequentially: a block of single-qubit rotations followed by a pattern of fixed, non-parametric two-qubit entangling gates. The parameter tensor supplied to the template has shape $(L, M, 3)$, where L denotes the number of layers, M the number of qubits, and the final dimension corresponds to the three rotation angles applied to each qubit in every layer. Thus, each layer implements three learnable single-qubit rotations on all M wires, contributing a total of $3M$ trainable parameters. The circuit template is drawn in 4.

Following the local rotations, the layer applies a set of entangling operations designed to generate strong, globally distributed correlations across the register. These entanglers are instantiated through a fixed two-qubit gate—typically a CNOT, although other non-parametric two-qubit operation may be used—and are arranged according to a cyclic connectivity rule governed by the range hyperparameter r . For a given qubit i , the template couples it with qubit $(i + r) \bmod M$, ensuring that every qubit interacts with a partner displaced by r positions along the register. By selecting different values of r across successive layers, the architecture sweeps through complementary coupling patterns, thereby enhancing the propagation of information and the circuit’s effective expressive power. If a single-qubit system is supplied, the template automatically omits entanglers, reducing to a purely local parametrized layer.

This construction yields a compact yet highly expressive variational block, capable of generating substantial entanglement with depth linear in the number of qubits. The design is inspired by the circuit-centric classifier *et al.* [46], and has become a standard choice in QML applications due to its balanced trade-off between expressivity, trainability, and compatibility with gradient-based optimization methods. Its layered structure, consisting of parametrized rotations interleaved with deterministic entanglers, makes it well suited for supervised learning, quantum neural network models,

and general variational tasks where strong entanglement and efficient parameterization are required.

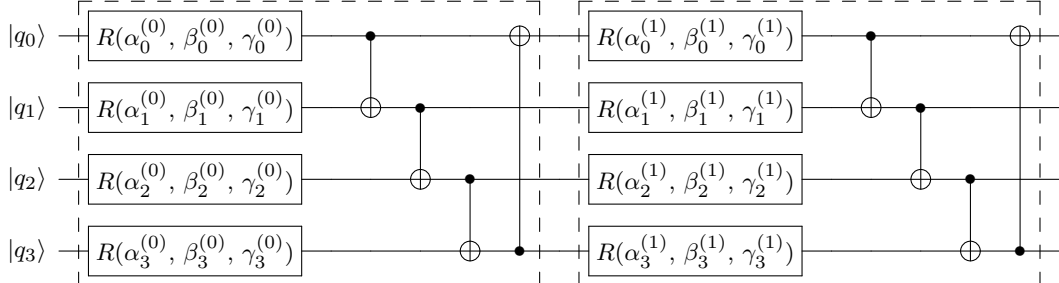


Fig. 4 Strongly Entangling Layers (PennyLane implementation). Each layer applies three-parameter rotations $R(\alpha, \beta, \gamma)$ on every qubit, followed by CNOTs with periodic pattern: in layer l with range $r = l \bmod M$, each qubit i controls qubit $(i + r) \bmod M$. The weight tensor has shape $(L, M, 3)$ [47].

3.2.2 Basic Entangler Layer

Another commonly employed variational template in quantum machine learning is the *Basic Entangler Layers* architecture, which offers a simple yet effective mechanism for generating entanglement across a quantum register. Each layer of this template consists of a block of single-qubit rotations followed by a closed ring of fixed, non-parametric two-qubit entangling gates. The trainable parameters are supplied through a tensor of shape (L, M) , where L denotes the number of layers and M is the number of qubits acted upon by the template. Each element of this tensor specifies the angle of a one-parameter rotation applied to a corresponding qubit; unless otherwise specified through the `rotation` argument, these rotations default to R_X gates. Consequently, each layer contributes exactly M trainable parameters. The circuit template is drawn in 5.

Following the local rotations, the template applies a sequence of two-qubit entanglers arranged in a ring topology. In its standard configuration, each qubit i is coupled to its immediate neighbor $(i + 1) \bmod M$ via a CNOT gate, thereby forming a closed chain that wraps around the register. This cyclic structure ensures that correlations can propagate across the entire system, enabling the circuit to capture global features of the data with minimal depth. When the template operates on only two qubits, it follows the established convention of applying a single CNOT per layer, thereby avoiding repeated use of the same entangler on an identical pair of wires. If a single qubit is provided, the template naturally reduces to a purely local parametrized layer, since no entanglement can be generated.

The *Basic Entangler Layers* template is widely used due to its simplicity, hardware friendliness, and compatibility with gradient-based variational optimization. Its fixed entangling pattern minimizes architectural complexity while still enabling the formation of sufficiently expressive quantum states for many learning tasks. The combination of lightweight parameterization and an efficient entanglement structure

makes this template a standard baseline for benchmarking variational quantum circuits and serves as a natural point of comparison for more expressive or automatically synthesized architectures.

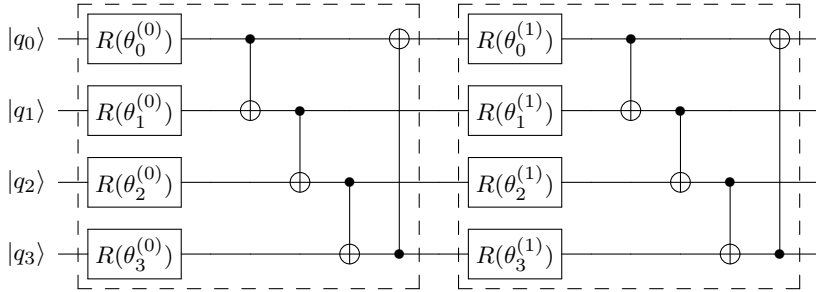


Fig. 5 Basic Entangler Layers (PennyLane implementation). Each layer applies single-parameter rotations (default R_X) on all qubits, followed by a closed ring of CNOT gates connecting neighboring qubits with periodic boundary conditions. The weight tensor has shape (L, M) where L is the number of layers and M the number of qubits; for two qubits, the periodic connection is omitted to avoid repeated entanglement [47].

3.2.3 Simplified Two Design

The *Simplified Two Design* architecture is a variational template inspired by the 2-design constructions analyzed by Cerezo *et al.* [48], proposed originally to study trainability and the emergence of barren plateaus in quantum optimization landscapes. In random quantum circuit theory, a unitary 2-design is an ensemble of unitaries whose first and second statistical moments match those of the Haar measure, thereby providing an efficient surrogate for sampling random unitaries. While the present template does not constitute a strict unitary 2-design—since it is not built from a universal set of two-qubit gates—it retains several of the structural properties associated with 2-designs and has been demonstrated to induce expressive quantum states suitable for the study of variational optimization behavior. The circuit template is drawn in 6.

The construction begins with an initial layer of single-qubit R_Y rotations, controlled by a vector of parameters of dimension M , where M denotes the number of qubits. This initialization is followed by L main layers, each designed to alternate entanglement patterns in a manner reminiscent of brickwork-style random circuits. Each layer is composed of two parts: an “even” block and an “odd” block. The even block applies controlled- Z (CZ) entanglers to qubit pairs $(0, 1)$, $(2, 3)$, and so forth, followed by a pair of parametrized R_Y rotations applied independently to each qubit in the entangled pair. The odd block then shifts this pattern by one qubit, applying CZ gates to pairs $(1, 2)$, $(3, 4)$, and so on, again followed by the corresponding local rotations. Through this alternating pattern, every qubit interacts with both of its neighbors across successive layers, promoting effective information scrambling and a diverse entanglement structure.

The parameterization of the template reflects this layered organization. The initial layer weights form a vector of shape (M) , while the weights for the main body of the

circuit are organized in a tensor of shape $(L, M - 1, 2)$, corresponding to $M - 1$ pairs of rotation angles per layer. As a result, each layer applies $2(M - 1)$ trainable single-qubit rotations interleaved with deterministic CZ gates. This structure preserves a relatively shallow depth while enabling the circuit to approximate, in practice, several of the expressivity properties expected from true 2-design ensembles.

Overall, the *Simplified Two Design* offers a balance between architectural simplicity and expressive richness, providing a template that is both theoretically motivated and practically useful in variational quantum algorithms. Its layered CZ– R_Y structure makes it well suited for analyzing optimization landscapes, benchmarking variational models, and comparing the trainability of different ansatz families under controlled entanglement and parameterization patterns.

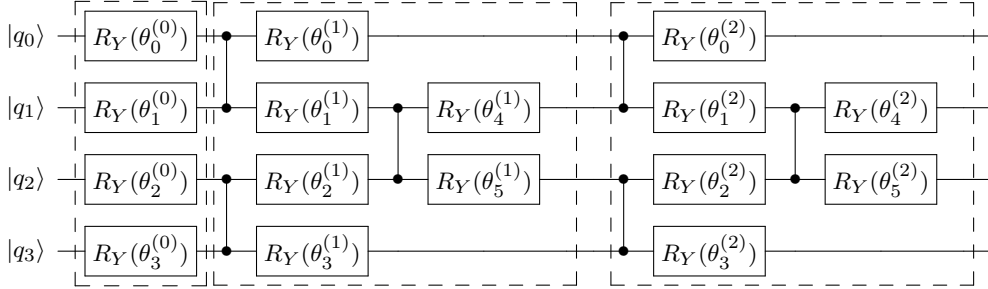


Fig. 6 Simplified Two-Design architecture (PennyLane implementation). The circuit consists of an initial layer of Pauli-Y rotations on all qubits, followed by two processing units (dashed boxes). Each unit implements a CZ entangler (alternating control positions between units) followed by two RY rotations per qubit. The weight tensor has shape $(L, M - 1, 2)$ where L is the number of layers and M is the number of qubits [47].

4 Complexity Measures for Regression

Metalearning investigates how to use metaknowledge to adapt machine-learning and data-mining processes more efficiently. Although many algorithms can produce good models, choosing the most appropriate one still requires a systematic strategy. Metalearning offers this strategy by enabling systems to improve their performance through accumulated experience [49]. In [50], it was introduced and evaluated novel regression complexity measures that effectively characterize the functional structure of regression datasets and serve as informative meta-features, enabling accurate prediction of function types, tuning of support vector regressor hyperparameters, and forecasting of regressor performance, often matching or surpassing classical meta-features in meta-learning tasks. This section introduces that collection of numerical indicators designed to quantify the intrinsic difficulty of regression tasks. These measures examine the learning problem from distinct viewpoints and are organized into four major groups:

- **Feature–output association:** characterizes how individual predictors relate to the target variable;

- **Linearity indicators:** evaluate whether linear functions are adequate to approximate the underlying data-generating process;
- **Smoothness criteria:** assess how smoothly the target varies with respect to the input features;
- **Geometric, topological, and density descriptors:** capture how samples are spatially arranged in the input–output domain.

Let \mathbf{X} denote the data matrix composed of n observations described by d predictors. The i -th instance is expressed as $\mathbf{x}_i \in \mathbb{R}^d$, whereas the j -th feature corresponds to the column vector \mathbf{x}_j . The response vector is given by $\mathbf{y} = (y_1, \dots, y_n)^\top$, where each $y_i \in \mathbb{R}$.

Several metrics rely on properties of a multiple linear regression model of the form

$$f(\mathbf{x}) = \beta_0 + \beta_1 x_1 + \dots + \beta_d x_d + \varepsilon,$$

where β_k are the regression coefficients and ε denotes the residual error.

4.1 Feature–Output Association

Measures in this category quantify the strength of dependence between each predictor and the target variable. High dependence implies that the regression function can be approximated using simpler models. These metrics treat each predictor independently—an intentional simplification that allows a coarse yet informative assessment of the factors contributing to task difficulty.

4.1.1 Maximum Correlation (C1)

For each feature \mathbf{x}_j , we compute the absolute Spearman rank correlation with \mathbf{y} , denoted by $|\rho(\mathbf{x}_j, \mathbf{y})|$. Since the correlation domain is $[-1, 1]$, large values (positive or negative) reflect strong monotonic associations. The measure $C1$ is defined as

$$C1 = \max_{j=1, \dots, d} |\rho(\mathbf{x}_j, \mathbf{y})|.$$

Spearman correlation is employed because it is nonparametric and does not assume any specific form for the predictor–target relationship. Computing $C1$ requires $O(d n \log n)$ operations. Larger values indicate simpler problems, as at least one predictor strongly aligns with the response.

4.1.2 Average Correlation (C2)

Instead of focusing on the best predictor, $C2$ summarizes the overall predictor–target dependency by averaging the absolute Spearman correlations:

$$C2 = \frac{1}{d} \sum_{j=1}^d |\rho(\mathbf{x}_j, \mathbf{y})|.$$

Its computational complexity is also $O(d n \log n)$. High values imply that many features contribute meaningful monotonic information regarding the target.

4.1.3 Individual Feature Efficiency (C3)

This measure evaluates how many samples must be progressively discarded from a dataset for a predictor to reach a high correlation threshold with the target. For every feature \mathbf{x}_j , we remove the minimum number of samples necessary so that $|\rho(\mathbf{x}_j, \mathbf{y})| > 0.9$. Let n_j denote the count of discarded samples. Then,

$$C3 = \min_{j=1, \dots, d} \frac{n_j}{n}.$$

A naive procedure would require cubic time in n , but an optimized version using ranking updates yields a worst-case complexity of $O(d n^2)$. Low values indicate simpler problems because a strong monotonic relationship emerges without removing many points.

4.1.4 Collective Feature Efficiency (C4)

This metric evaluates how effectively the full set of predictors, taken sequentially, can explain the data through simple linear fits. Starting from the most correlated feature, points whose absolute residuals satisfy $|\varepsilon_i| \leq 0.1$ are removed. The process repeats with the next most correlated feature applied to the remaining subset. If T_ℓ denotes the final data subset after ℓ iterations, the measure is

$$C4 = \frac{\#\{\mathbf{x}_i \in T_\ell \mid |\varepsilon_i| > 0.1\}}{|T_\ell|}.$$

The computational cost is $O(d^2 + d n \log n)$. Higher values indicate more complex datasets, as many points fail to align with simple linear explanations even when features are used sequentially.

4.2 Linearity Indicators

These metrics quantify the adequacy of a linear model to describe the dataset. When linear regression yields small residuals, the problem is considered inherently simpler.

4.2.1 Mean Absolute Residual (L1)

The first linearity measure is the mean absolute deviation of residuals obtained from a multiple linear regression:

$$L1 = \frac{1}{n} \sum_{i=1}^n |\varepsilon_i|.$$

Lower values denote problems that are well approximated by linear functions. The overall computational complexity is $O(nd^2)$ due to the regression estimation.

4.2.2 Residual Variance (L2)

The second measure computes the mean squared residual:

$$L2 = \frac{1}{n} \sum_{i=1}^n \varepsilon_i^2.$$

Smaller values again suggest that the target can be described with a linear model. This measure also requires $O(nd^2)$ time.

4.3 Smoothness Criteria

Smoothness indicators evaluate how gradually the target variable changes with respect to the input. Problems where nearby samples exhibit similar outputs tend to be easier for regression algorithms.

4.3.1 Output Variation Along a Minimum Spanning Tree (S1)

Following the spirit of MST-based measures in earlier literature, we construct a Minimum Spanning Tree on the input space, where vertices correspond to data points and edge weights represent Euclidean distances. Let MST denote the set of adjacent pairs (i, j) . The measure is defined as

$$S1 = \frac{1}{n} \sum_{(i,j) \in MST} |y_i - y_j|.$$

Low values imply that nearby points in the input space also have similar outputs. Constructing the MST requires $O(n^2d)$ for distance computation plus $O(n^2)$ for Prim's algorithm.

4.3.2 Input Variation Across Ordered Outputs (S2)

After sorting samples by their target values, we compute the Euclidean distance between successive samples:

$$S2 = \frac{1}{n} \sum_{i=2}^n \|\mathbf{x}_i - \mathbf{x}_{i-1}\|_2.$$

Low values indicate that samples with similar outputs lie close in the input space. The computation requires $O(n(d + \log n))$ operations.

4.3.3 Nearest-Neighbor Regression Error (S3)

This measure computes the leave-one-out mean squared error of a 1-nearest-neighbor regressor:

$$S3 = \frac{1}{n} \sum_{i=1}^n (NN(\mathbf{x}_i) - y_i)^2,$$

where $NN(\mathbf{x}_i)$ is the prediction given by the nearest neighbor of \mathbf{x}_i in the input space. High values correspond to irregular or sparse regions in the dataset. The asymptotic complexity is $O(d n^2)$.

4.4 Geometric, Topological, and Density Descriptors

These measures capture how samples populate the input space and how the regression function behaves under synthetic perturbations or geometric transformations.

4.4.1 Nonlinearity of Linear Regression (L3)

Adapted from earlier nonlinearity measures for classification, this metric evaluates how a linear regressor performs on artificially generated points. Pairs of samples with adjacent target values are linearly interpolated to form new test points (\mathbf{x}'_i, y'_i) . A linear model is fitted to the original data, and its mean squared error on the interpolated set is computed as

$$L3 = \frac{1}{\ell} \sum_{i=1}^{\ell} (f(\mathbf{x}'_i) - y'_i)^2,$$

where $\ell = n - 1$. Low values indicate that the linear model behaves consistently in regions between observed samples. The complexity is $O(n(d^2 + \log n))$.

4.4.2 Nonlinearity of Nearest-Neighbor Regression (S4)

Using the same interpolated points as $L3$, this measure replaces the linear regressor with a 1-nearest-neighbor predictor:

$$S4 = \frac{1}{\ell} \sum_{i=1}^{\ell} (NN(\mathbf{x}'_i) - y'_i)^2.$$

Datasets requiring highly nonlinear behaviors yield higher values. Using a KD-tree implementation results in an asymptotic complexity of $O(n d \log n)$.

4.4.3 Average Sample Density per Dimension (T2)

This simple indicator evaluates data sparsity by computing the average sample count per feature dimension:

$$T2 = \frac{n}{d}.$$

Low values correspond to sparse or high-dimensional datasets, which typically impose additional complexity on regression algorithms. Its complexity is linear in n and d , i.e $O(n + d)$.

5 Genetic Algorithm Search Proposed Approach: Reduced Regressor Quantum Neural Network

In this work, we introduce a Reduced Regressor Quantum Neural Network (RRQNN) whose variational architecture is automatically discovered through a Genetic Algorithm (GA). Each candidate quantum circuit is encoded as an integer vector

$$\boldsymbol{\Lambda}_i = [\Lambda_1, \Lambda_2, \dots, \Lambda_{3n_{\text{layers}}}], \quad (19)$$

whose total size is exactly $3n_{\text{gates}}$, where n_{gates} is the maximum quantity of gates in the circuit. This full vector represents the complete structural characterization of the quantum circuit discovered by the GA.

The chromosome is partitioned into three equal segments:

$$\boldsymbol{\Lambda}_i = \underbrace{[\Lambda_1, \dots, \Lambda_{n_{\text{gates}}}]}_{\text{Gate IDs}} \parallel \underbrace{[\Lambda_{n_{\text{gates}}+1}, \dots, \Lambda_{2n_{\text{gates}}}]}_{\text{Control Qubits}} \parallel \underbrace{[\Lambda_{2n_{\text{gates}}+1}, \dots, \Lambda_{3n_{\text{gates}}}]}. \quad (20)$$

Only the first segment, containing the Gate IDs, determines the type of operation applied at each layer. The second and third segments specify, respectively, the control and target qubits associated with the operations. These indices are meaningful only when the circuit has two or more qubits; when $n_{\text{qubits}} = 1$, controlled operations collapse into their single-qubit counterparts and the control/target entries are ignored.

For single-qubit architectures, each gate identifier satisfies $\Lambda_j \in \{0, \dots, 6\}$, while for two-qubit architectures the search space expands to $\Lambda_j \in \{0, \dots, 13\}$, enabling the encoding of controlled operations, where 6 and 13 indicate the index of the operators that will be mapped in the quantum circuit (explained in detail in Section 5.2).

The RRQNN receives as input a real-valued sample

$$\mathbf{x} = \{x_1, x_2, \dots, x_v\}, \quad (21)$$

where v corresponds to the dimensionality of the training set, and it contains a vector of trainable parameters

$$\theta = \{\theta_1, \theta_2, \dots, \theta_{n_{\text{gates}}}\}, \quad (22)$$

5.1 Genetic Algorithm Formulation

The genetic algorithm was implemented using the PyGAD Python library with default operator configurations. The algorithmic flow begins by instantiating a population of 20 randomly generated individuals, where each individual represents a distinct quantum circuit architecture. Each individual is subsequently evaluated and assigned a fitness score.

The fitness function is defined as $\text{Loss} = -1 \times R^2$, where lower values indicate superior performance. Fitness scores are computed based on the training performance of each circuit, as evaluated by the OPTAX optimizer on the training dataset. Following the evaluation phase, we employ a steady-state selection strategy combined with single-point crossover. The four best-performing individuals are identified and retained as elites. Two parents are randomly selected from this elite set to generate

offspring through single-point crossover, where a random gene index is chosen as the crossover point and genetic material is exchanged between parents at this location.

During offspring generation, a mutation operator is applied where 10% of the genome is randomly modified, with mutated genes assigned new randomly selected values drawn from the predefined gene space. The mutation operation has a per-individual probability of 20%.

After the new population is generated, fitness evaluation is repeated for all individuals. This iterative process continues until the termination criterion is satisfied. In our formulation, the algorithm evolves for 15 generations, after which the best individual in the population is selected as the final optimized quantum circuit. The complete algorithmic flow is illustrated in Fig. 8.

5.2 Deterministic Mapping from Chromosome to Quantum Circuit

Given the chromosome $\Lambda_i \in \mathbb{Z}^{3n_{\text{layers}}}$, the construction of the quantum circuit is performed deterministically and sequentially. For a circuit composed of n_{layers} gate positions, the chromosome is partitioned as follows as described in Equation 20.

Thus, each layer i of the circuit is fully specified by the triplet:

$$g_i = \Lambda_i, \quad c_i = \Lambda_{n_{\text{layers}}+i} \bmod n_{\text{qubits}}, \quad t_i = \Lambda_{2n_{\text{layers}}+i} \bmod n_{\text{qubits}}. \quad (23)$$

The value g_i selects the gate type; c_i and t_i determine the qubits involved in the operation. For multi-qubit circuits, this encoding supports both single-qubit and controlled operations. For single-qubit circuits ($n_{\text{qubits}} = 1$), control and target indices collapse trivially to the same qubit, and controlled gates automatically reduce to their single-qubit versions. This uniform representation allows the GA to explore architectures across any number of qubits while maintaining a fixed and consistent chromosome structure.

During circuit construction, gates that require trainable parameters or input-dependent angles simply draw their corresponding values in the order they appear in the parameter vector and in the input feature vector. In this way, the sequential progression of the chromosome naturally determines the order in which trainable weights and feature angles are consumed, ensuring that each gate receives the correct argument without the need for explicitly tracking additional indices or counters.

The mapping rules applied to each layer are:

- If $g_i = 0$, no operation is applied.
- If $g_i = 1$ or $(g_i = 5 \wedge c_i = t_i)$, apply $RX(\theta_k, \text{wires} = t_i)$.
- If $g_i = 2$ or $(g_i = 6 \wedge c_i = t_i)$, apply $RY(\theta_k, \text{wires} = t_i)$.
- If $g_i = 3$ or $(g_i = 7 \wedge c_i = t_i)$, apply $RZ(\theta_k, \text{wires} = t_i)$.
- If $g_i = 4$ and $c_i \neq t_i$, apply $CNOT([c_i, t_i])$.
- If $g_i \in \{5, 6, 7\}$ and $c_i \neq t_i$, apply:

$$g_i = 5 : CRX(\theta_k, [c_i, t_i]), \quad (24)$$

$$g_i = 6 : CRY(\theta_k, [c_i, t_i]), \quad (25)$$

$$g_i = 7 : CRZ(\theta_k, [c_i, t_i]). \quad (26)$$

- If $g_i = 8$ or $(g_i = 11 \wedge c_i = t_i)$, apply $RX(x_m, \text{wires} = t_i)$.
- If $g_i = 9$ or $(g_i = 12 \wedge c_i = t_i)$, apply $RY(x_m, \text{wires} = t_i)$.
- If $g_i = 10$ or $(g_i = 13 \wedge c_i = t_i)$, apply $RZ(x_m, \text{wires} = t_i)$.
- If $g_i \in \{11, 12, 13\}$ and $c_i \neq t_i$, apply:

$$g_i = 11 : CRX(x_m, [c_i, t_i]), \quad (27)$$

$$g_i = 12 : CRY(x_m, [c_i, t_i]), \quad (28)$$

$$g_i = 13 : CRZ(x_m, [c_i, t_i]). \quad (29)$$

Here, x_m denotes the feature angle and θ_k the trainable parameter associated with the operation.

An example of representative encoded individual [2, 4, 1, 6, 5] produces the quantum circuit shown in Figure 7.

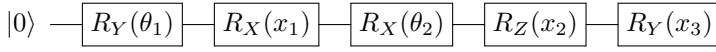


Fig. 7 Quantum circuit that is encoded by the chromosome vector [2, 4, 1, 6, 5] as explained in Section 5.

6 Experimental Protocol

This section describes the experimental methodology employed to evaluate and compare a broad spectrum of quantum and classical regression models under controlled and reproducible conditions. All experiments were conducted on a suite of 22 three-dimensional benchmark functions, comprising unimodal and multimodal landscapes of varying structural complexity and nonlinear behavior. Each benchmark dataset consisted of 900 samples, generated uniformly over the input domain. For every dataset, 70% of the samples were used for training, while the *entire dataset* (100%) was employed to evaluate each model's ability to reproduce the full underlying function, thus providing a comprehensive assessment of generalization performance and functional fidelity. For every model and every function, a total of ten independent runs were executed.

All experiments were conducted on a workstation equipped with 16 GB of RAM and a 12th Generation Intel® Core™ i7-12700H processor with 20 logical cores, and a 512 GB solid-state drive. The operating system was Ubuntu 22.04 LTS. The software stack used in the experiments included Python 3.11.5, **scikit-learn** 1.6.1 for classical regression models implementation, PennyLane 0.42.3 for quantum circuit simulation, and **jax** 0.6.2 together with **optax** 0.2.6 for differentiable programming and gradient-based optimization. The genetic algorithm experiments were implemented using the **pygad** library (version 2.5.0). The **problexity** library (version 0.5.11) [51] was used to generate the complexity metrics of the regression functions. This configuration ensured a stable and reproducible environment for the execution, optimization, and benchmarking of all quantum and classical regression models.

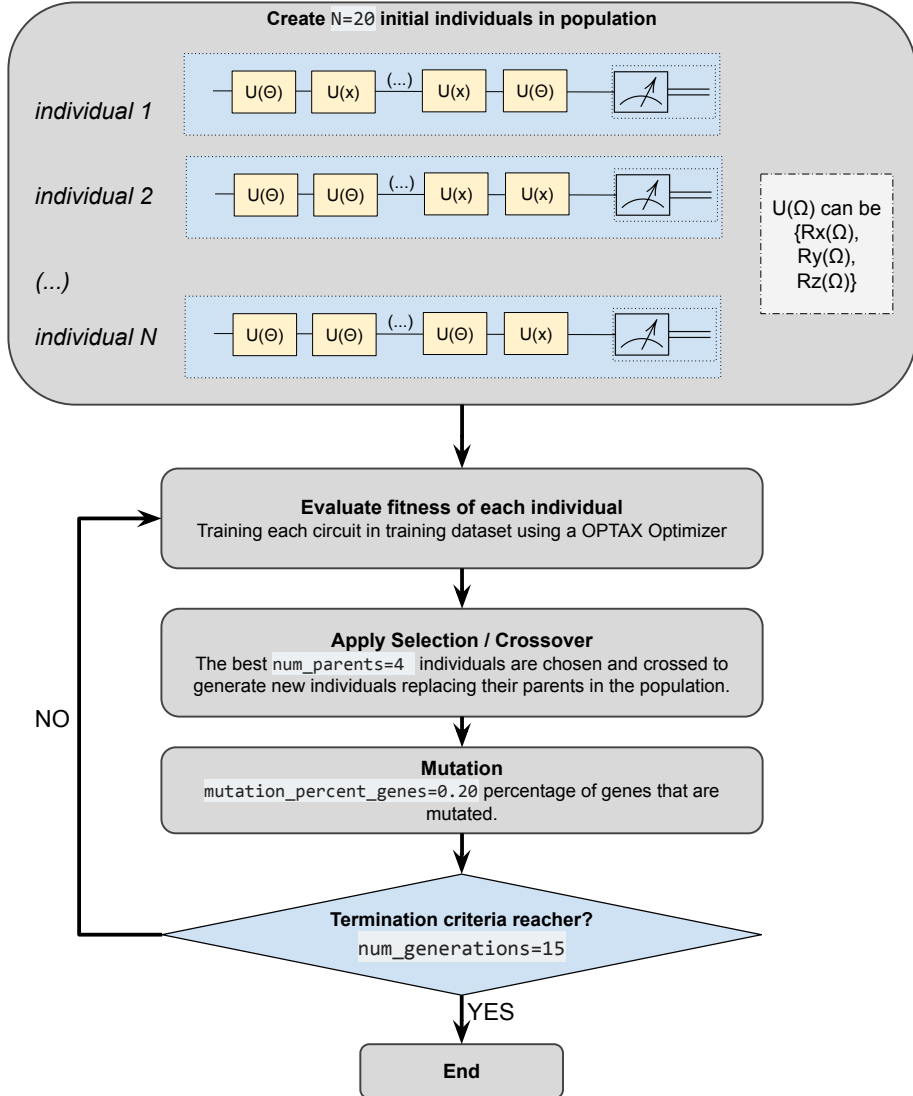


Fig. 8 Execution flow of the genetic algorithm generating reduced quantum neural networks with multiple input loading.

6.1 Quantum Models

A total of 44 quantum regression models were evaluated. These models fall into two major categories: (i) fixed QNN ansatz architectures widely adopted in the literature, and (ii) architectures automatically constructed by a Genetic Algorithm (GA). All

quantum models were trained using the Adam optimizer with a learning rate of 0.05, implemented via `optax` library and leveraging the parallelization capabilities of `JAX`.

6.1.1 Fixed QNNs Ansatz Families

We considered three well-established QNN as type of variational quantum circuit templates (explained in Sections 3.2.1, 3.2.3, and 3.2.2), i.e. $\text{QNN} \in \{\text{StronglyEntanglingLayers}, \text{SimplifiedTwoDesign}, \text{BasicEntanglerLayers}\}$. Each template was instantiated with different depths, corresponding to the following L numbers of layers, where $L \in \{1, 2, 3, 4, 5, 6, 7, 8, 9, 10, 20, 40, 60\}$. Given the three types of circuits and the twelve possible depths, this results in 36 distinct quantum models. We named each one of these models as $\text{QNN-}L$. Before each layer of the quantum ansatz, the input features are loaded in parallel using R_z rotation gates. That is, for an ansatz with L layers, the input is re-encoded L times, once before each layer. This repeated data re-uploading strategy significantly enhances the expressive capacity and supports the universal approximation properties of these models [23].

6.1.2 Genetic-Algorithm-Generated Quantum Circuits named as Reduced Regressor Quantum Neural Networks

Beyond fixed architectures, we explored model discovery through an evolutionary design process. A Genetic Algorithm (GA) was executed ten times independently, with each run allowed to construct circuits acting on either one or two qubits. To control model complexity, the GA was constrained by upper bounds on the number of optimizable parameters. The generated RRQNN circuits were limited to P_{max} quantum gates, where $P_{max} \in \{120, 60, 40, 20\}$, and q for both 1-qubit and 2-qubit configurations. This yields 8 RRQNNs configurations, named each one as $\text{RRQNN-}P_{max}\text{-}q$.

6.2 Classical Regression Models - Baselines

To contextualize the performance of quantum models, we employed a diverse suite of 17 classical regression baselines spanning distance-based, tree-based, kernel-based, and neural networks models. Each model and its settings are detailed in Table 1. The parameters not mentioned are the defaults in the `sklearn` library. The classical regressor models were executed ten times on each dataset, using data partitions identical to the quantum models.

The effective number of trainable parameters in each classical model reflects the intrinsic model capacity and serves as a baseline for discussing the expressive efficiency of quantum architectures. The parameter-counting procedure was systematically defined for each model family considered in this study, following the structural properties of their learning mechanisms. For K-Nearest Neighbors (KNN) regressors, it was considered that KNN does not learn parametric representations; instead, they store the training samples and make predictions through distance-based interpolation. Consequently, their number of trainable parameters is defined as zero, since no optimization is performed over a parametric function space.

For decision-tree regressors, the model complexity is directly tied to the structure of the learned tree. Each internal or terminal node corresponds to a decision rule or

leaf prediction, respectively. Therefore, the total number of trainable parameters is defined as the number of nodes in the learned tree, which captures the full set of data-dependent decisions encoded by the model. Random Forests aggregate multiple decision trees. Thus, their total number of trainable parameters is computed as the sum of the node counts of all individual trees in the ensemble. This definition reflects the distributed capacity of the model, as each tree contributes an independent substructure to the overall decision process.

For neural-network-based regressors, the total number of trainable parameters comprises all weight matrices and bias vectors across layers. Specifically, the number of parameters is obtained by summing the sizes (number of scalar entries) of all learned weight tensors and all corresponding bias vectors. This yields a comprehensive measure of the network’s expressive capacity, fully characterizing its parametric footprint.

The parameter count in SVR depends on the kernel employed. For linear kernels, the learned weight vector provides a direct parameterization of the decision function, and the parameter count is given by the total number of coefficients. In contrast, nonlinear kernels such as RBF, polynomial, or sigmoid do not maintain explicit weight vectors. Instead, their learned representation is defined through the support vectors, whose number and dimensionality jointly determine the effective parameter count. The total number of parameters is thus given by the size of the support-vector matrix.

Table 1 Classical Regressors used in the experiments.

Model acronym	Model name and configuration
DT	Decision Tree Regressor, default configuration
RF	Random Forest Regressor, default configuration
MLP100-ReLU	MLP, one hidden layer with 100 neurons, ReLU function
MLP500-ReLU	MLP, one hidden layer with 500 neurons, ReLU function
MLP100-100-ReLU	MLP, two hidden layers, 100 neurons, ReLU function
MLP500-500-ReLU	MLP, two hidden layers, 500 neurons, ReLU function
MLP100-Id	MLP, one hidden layer with 100 neurons, identity function
MLP500-Id	MLP, one hidden layer with 500 neurons, identity function
MLP100-100-Id	MLP, two hidden layers, 100 neurons, identity function
MLP500-500-Id	MLP, two hidden layers, 500 neurons, identity function
SVR-RBF	Support Vector Regressor, C = 1.0, Kernel = RBF, Gamma = Scale
SVR-linear	Support Vector Regressor, C = 1.0, Kernel = Linear, Gamma = Scale
SVR-sigmoid	Support Vector Regressor, C = 1.0, Kernel = Sigmoid, Gamma = Scale
SVR-poly	Support Vector Regression, C = 1.0, Kernel = Poly, Gamma = Scale
knn2, knn3, knn4	Regression based on k-nearest neighbors, k = 2
knn3	Regression based on k-nearest neighbors, k = 3
knn4	Regression based on k-nearest neighbors, k = 4

6.3 Training and Evaluation Procedure

For each of the 22 benchmark regression functions, the full dataset of 900 points was randomly split into 70% for training and 30% for testing. Only the training portion was used to fit the models. However, to enable direct comparison across all methods, all reported performance metrics— R^2 score and Root-Mean-Square Error (RMSE)—were computed on the *entire* dataset of 900 points. This protocol was repeated for ten independent random seeds, producing statistically meaningful performance estimates for every model [52].

The R^2 score is defined as:

$$R^2 = 1 - \frac{\sum_{i=1}^N (y_i - \hat{y}_i)^2}{\sum_{i=1}^N (y_i - \bar{y})^2}, \quad (30)$$

where y_i are the observed outputs, \hat{y}_i are the predicted values, and \bar{y} is the sample mean of the target variable.

The RMSE metric is computed as:

$$\text{RMSE} = \sqrt{\frac{1}{N} \sum_{i=1}^N (y_i - \hat{y}_i)^2}. \quad (31)$$

Both metrics were averaged over ten repetitions of the training–testing cycle for each model and each benchmark function.

6.4 Proof of concept - 1-dimensional functions

To assess whether a Genetic Algorithm (GA) is capable of discovering high-quality Regressor-Ready Quantum Neural Networks (RRQNNs) in low-dimensional settings, we conducted a proof-of-concept experiment involving four nonlinear one-dimensional functions, described in Equations 32, 33, 34, and 35. The objective of this evaluation was twofold: (i) to verify whether the GA can assemble expressive quantum circuits from a restricted set of parameterized gates, and (ii) to compare the resulting RRQNN regressors against a diverse collection of classical models under identical training and testing conditions. The results obtained for all functions are summarized in Table A1.

$$f_1^{1D}(x) = x^2, \quad (32)$$

$$f_2^{1D}(x) = x^3, \quad (33)$$

$$f_3^{1D}(x) = 2x^4 - 1, \quad (34)$$

$$f_4^{1D}(x) = \frac{0.9}{1 + e^{-10x}}. \quad (35)$$

The GA was allowed to generate RRQNN architectures with varying circuit sizes, here expressed as the total number of parameterized quantum gates (10, 15, 20, and 25). These RRQNNs were evaluated alongside standard classical baselines, including k -nearest neighbors (KNN), Support Vector Regressors (SVR), Random Forests (RF), Decision Trees (DT), and multilayer perceptrons (MLP). For each model, we report the R^2 score, the RMSE on the all dataset, providing a clear picture of the trade-off between model performance and complexity.

Discussion of Proof of Concept Results

The results in Table A1 reveal several notable patterns. First, across all four functions, RRQNNs with 20–25 gates consistently achieve the best or near-best performance among all tested models. For instance, on f_1^{1D} , the RRQNN with 25 gates attains $R^2 = 0.999$ with an RMSE of only 0.0092, outperforming all classical baselines, including Random Forests and Decision Trees. This trend persists in f_2^{1D} , f_3^{1D} , and f_4^{1D} , where RRQNN-25 again exhibits top performance, achieving optimal accuracy ($R^2 = 1.000$) on f_4^{1D} with only 25 parameters.

Second, classical models show a broader range of behaviors. While Random Forests and Decision Trees are competitive on most tasks, they do so at a much higher parameter cost; for example, RF uses more than 3600 parameters on f_1^{1D} , compared to just 25 for RRQNN-25. Simpler classical models such as KNN demonstrate reasonable predictive performance but cannot match the precision of the quantum circuits on more complex targets. Support Vector Regression shows highly heterogeneous behavior: although SVR-poly achieves moderate accuracy on f_2^{1D} , all kernel variants exhibit numerical instability or degenerate solutions for the other functions, reflected by $R^2 = -\infty$.

Third, multilayer perceptrons (MLPs) perform surprisingly poorly in this setting, often yielding extreme negative R^2 values, particularly for f_1^{1D} and f_3^{1D} . This indicates severe overfitting or optimization failure, despite their large parameter count (from 301 up to more than 10,000 trainable weights). By contrast, RRQNNs succeed with only a few dozen parameters, highlighting their favorable inductive bias for structured, low-dimensional nonlinear problems.

Overall, the proof of concept demonstrates that the Genetic Algorithm is indeed capable of discovering expressive and parameter-efficient RRQNN architectures for 1D regression. These automatically generated quantum models do not merely match classical regressors; in most cases, they surpass them—while requiring drastically fewer parameters - which was expected as demonstrated in [53]. The clear performance gap between RRQNNs and classical baselines, especially on the more intricate functions, confirms the viability of evolutionary search as a tool for quantum circuit design in regression tasks.

The best-performing RRQNN models identified in the proof-of-concept study were subsequently used to visualize the reconstructed regression functions. These visualizations, presented in Figure 9, illustrate the ability of the automatically discovered quantum circuits to closely approximate the underlying nonlinear target functions across all four one-dimensional benchmarks. The plots clearly show that the RRQNN architectures not only capture the global shape of each function but also reproduce fine-grained variations with high fidelity, corroborating the quantitative superiority reported in Table A1.

6.5 Benchmark Suite of Nonlinear Regression Functions

In order to thoroughly evaluate the performance and generalization capacity of the proposed regression framework, a benchmark suite composed of 22 nonlinear functions was employed. This suite includes the ten functions from the CEC 2020

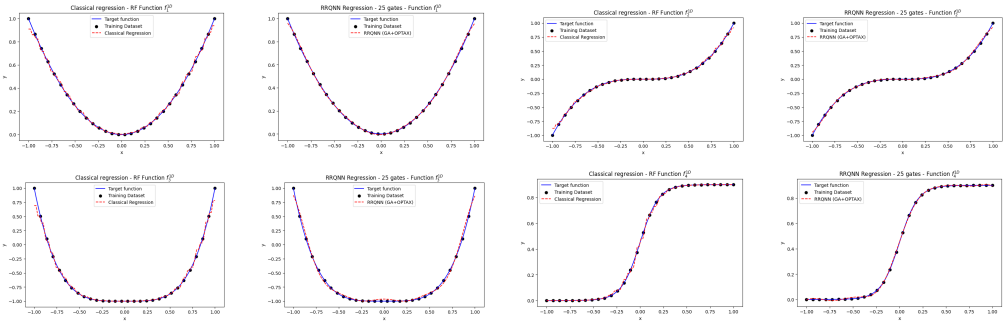


Fig. 9 Results of the best regression models for the four one-dimensional functions defined in Equations 32–35, as described in the proof-of-concept protocol (Section 6.4), comparing classical regression models with the proposed RRQNN quantum model.

benchmark and an additional set of thirteen classical nonlinear functions broadly adopted in the evolutionary computation and global optimization literature [54]. Together, these functions cover a wide range of properties—such as modality, separability, conditioning, ruggedness, and the presence of deceptive or composite landscape features—ensuring a rigorous experimental evaluation.

The IEEE Congress on Evolutionary Computation (CEC) benchmark series is one of the most influential standardized problem sets used for testing optimization and learning algorithms. Specifically, the CEC 2020 benchmark [55] contains ten functions designed to provide diverse challenges, including unimodal, multimodal, hybrid, and composite formulations. These functions incorporate transformations such as shifting, rotation, noise components, and hierarchical composition, thereby simulating realistic high-dimensional optimization scenarios.

The ten CEC 2020 functions used in the present work correspond to: Unimodal Sphere Function, High Conditioned Elliptic function, Bent Cigar Function, Discus Function, Sum of Different Powers 2 Function, Rosenbrock Function, Expanded Schaffer’s F6 Function, Ackley Function, Rastrigin Function, Weierstrass Function. These functions are widely recognized for their diversity and controlled complexity, and they have become a standard tool for benchmarking advanced optimization algorithms. Their inclusion ensures compatibility with contemporary results in the literature and allows direct comparison with state-of-the-art techniques.

As mentioned previously, to complement the CEC 2020 benchmark, thirteen additional functions were selected from the classical optimization literature. They vary significantly in terms of modality, separability, and conditioning, offering a broader spectrum of complexity beyond the CEC set. These functions constitute a comprehensive nonlinear testbed, including heavy-tailed landscapes (Schwefel), recursively fractal structures (Katsuura), hybrid formulations combining multiple landscape types (Grie–Rosen), and smooth low-curvature problems (Zakharov, Lévy). Their inclusion ensures a diversified and challenging environment for evaluating regression models, particularly those relying on evolutionary, stochastic, or variational optimization components.

In Table 2, all functions are detailed and numbered to facilitate their referencing throughout this work. This combined dataset of 22 nonlinear regression functions forms a robust and widely recognized benchmark suite. It provides an extensive and challenging environment for assessing model performance under a wide range of nonlinear behaviors and landscape difficulties.

6.6 Scalability and Experimental Scope

In this experimental study, quantum models are primarily analyzed and compared in terms of architectural complexity, quantified by the number of trainable parameters and quantum operators composing each circuit. This abstraction enables a systematic comparison across a large number of quantum and classical models while keeping the experimental protocol tractable and reproducible.

Experiments involving noisy quantum simulators or real quantum hardware were intentionally not included in the present evaluation. Given the density and breadth of the experimental campaign—which encompasses multiple circuit families, depths, benchmark functions, and repeated runs—the analysis was conducted under noiseless simulation in order to isolate architectural effects and training behavior. A more detailed investigation of noise effects, hardware constraints, and error mitigation strategies is therefore left for future work, where a reduced set of representative architectures can be examined in greater depth on actual quantum processors platforms [56].

Future studies may also extend the analysis to quantum neural networks with a larger number of qubits, explore alternative architectural paradigms beyond the ansätze considered here, and investigate different training strategies, including gradient-free optimization, adaptive learning schemes, and noise-aware training methods. Such extensions could enable a more thorough assessment of the scalability, robustness, and practical viability of automated quantum model design in real-world quantum computing settings.

7 Results and Discussions

We outline here the structure of the analyses conducted in this section. Our results begin with a comparison between quantum and classical regression models (Section 7.1). This design allows us to evaluate average performance, variability, and parameter efficiency, while also determining—via statistical significance testing—whether classical models that surpass quantum ones in mean performance are in fact *significantly* better, or whether quantum models remain statistically equivalent despite using far fewer parameters (Section 7.1.1).

We then investigate whether the genetic algorithm responsible for generating the Reduced Regressor Quantum Neural Networks (RRQNNs) exhibits systematic architectural tendencies. By applying clustering techniques to the circuits produced across all benchmarks, we explore the emergence of recurring design motifs and potential structural regularities that may reflect an implicit evolutionary preference for certain quantum topologies (Section 7.2).

Next, we analyze how the performance of the three quantum model families—*StronglyEntanglingLayers*, *SimplifiedTwoDesign*, *Basic*—varies as circuit depth increases. This examination reveals important insights into the relationship between expressivity, generalization, and the number of layers, clarifying whether deeper architectures consistently yield better regression performance (Section 7.3).

Finally, we report results from a meta-learning study that evaluates whether dataset-level complexity measures can predict the optimal quantum model class, the best RRQNN architecture, and its associated hyperparameters. As shown in this section, the meta-learning pipeline demonstrates remarkably strong predictive ability, offering a compelling path toward automated selection of quantum models for regression tasks (Section 7.4).

7.1 Analysis of R^2 score and RMSE

The average R^2 -Score and RMSE results for each model run on each of the functions can be found in Tables B2-B23. The first group of functions, from f_1 to f_6 , consists of smooth and locally regular functions. These functions generally benefit from the simpler classical models, especially tree-based methods like RF and DT, which yield high R^2 scores close to 1, demonstrating near-optimal fit with minimal error. Classical models such as k -Nearest Neighbors also perform well, achieving R^2 values exceeding 0.995, despite having no trainable parameters. However, quantum models also perform well on these functions. For example, the StronglyEntanglingLayers-20/40/60 models, with depths of 20 to 60 layers, achieve R^2 values around 0.995 to 0.997, which is very close to the performance of classical models. Similarly, the SimplifiedTwoDesign (STD) and BasicEntanglerLayers (BEL) models also deliver comparable results, albeit with slightly fewer parameters than their classical counterparts.

The RRQNN models show remarkable efficiency, especially for those with larger parameter budgets. For instance, the RRQNN-120-2q model, which uses only about 80 parameters, reaches R^2 scores around 0.996-0.997, which is impressive given its minimal expressivity. However, models with tighter parameter budgets, such as RRQNN-10-1q, exhibit a reduction in performance, but still maintain an R^2 greater than 0.90. These results demonstrate that quantum models, particularly resource-restricted networks, can match or even exceed classical performance with far fewer parameters, marking a significant advantage for quantum machine learning approaches.

Moving to Function f_7 , we observe a sharp transition in performance. This function introduces nonlinearity and structural complexity that confounds even the most robust classical models. Classical models such as RF still perform relatively well, but their R^2 values drop significantly compared to the previous functions, with RF scoring around 0.85. Quantum models face similar challenges, with SEL-40/60 and STD-40/60 yielding R^2 values around 0.65-0.71. The RRQNN models, especially those with fewer parameters, struggle to achieve higher accuracy, with performance collapsing to near-random predictions as the parameter budget is reduced further. This function serves as an example where both classical and quantum models face challenges, suggesting that higher expressivity or a different model architecture may be required to handle such complex, irregular landscapes.

For Functions f_8 to f_{13} , which feature moderate nonlinearity and some degree of multi-modality, classical models once again excel. Random Forest and other ensemble models maintain strong performance, with R^2 values consistently above 0.95. Quantum models, however, begin to close the gap, particularly with deeper SEL and STD circuits. The SEL models with 40 to 60 layers reach R^2 values between 0.90 and 0.97, which is comparable to classical models in this range. The RRQNN models, particularly those with larger budgets (e.g., RRQNN-120), also perform excellently, demonstrating their ability to capture complex patterns with fewer parameters than classical models.

In particular, Function f_{11} stands out. While classical decision tree models fail to capture the underlying complexity of the function, the SEL and STD models achieve competitive performance, outperforming their classical counterparts. This indicates that quantum models, particularly those with deep entangling layers, are better suited for capturing non-axis-aligned feature relationships that simpler classical models struggle with.

Function f_{14} marks a significant milestone in this study, as it is the first function where quantum models outperform all classical baselines. The StronglyEntanglingLayers-60 model achieves an R^2 of approximately 0.987, while the RF model lags behind at R^2 of 0.93. This result highlights a key advantage of quantum models: their ability to model complex, non-linear relationships that classical models cannot easily capture, especially when the function exhibits entangling or high-dimensional characteristics.

Functions f_{15} to f_{18} represent a transition to more challenging landscapes with higher-dimensional interactions and local irregularities. In these cases, classical models remain strong, with Random Forests and Decision Trees continuing to outperform most quantum models, achieving near-optimal R^2 scores. However, quantum models, particularly the deeper SEL and STD circuits, remain competitive, reaching R^2 values around 0.95-0.99, while still demonstrating the ability to model these complex interactions with fewer parameters. The RRQNNs, once again, show their strength in terms of parameter efficiency, achieving performance comparable to deep quantum circuits while using a fraction of the number of parameters.

In the final group of functions, from f_{19} to f_{22} , we observe the effects of highly structured regimes. These functions introduce significant complexity, making them particularly difficult for all models. Classical ensembles, including RF and MLPs, perform well, but their performance drops off at higher levels of complexity, with R^2 values ranging from 0.90 to 0.99. Quantum models, particularly SEL and STD circuits, show a similar trend, with performance ranging from 0.90 to 0.97. RRQNNs, particularly those with larger parameter budgets, maintain solid performance in this regime, although their accuracy begins to degrade as the complexity of the functions increases. The compact RRQNNs, such as RRQNN-10-1q, still achieve an R^2 of around 0.96, but they fall short on the most complex functions.

R^2 -Score values less than -100 were represented by *inf* (infinity) in the respective results tables.

Figure 11 provides a global overview of the relative performance of all quantum and classical models across the benchmark suite. The heatmap reveals a clear stratification

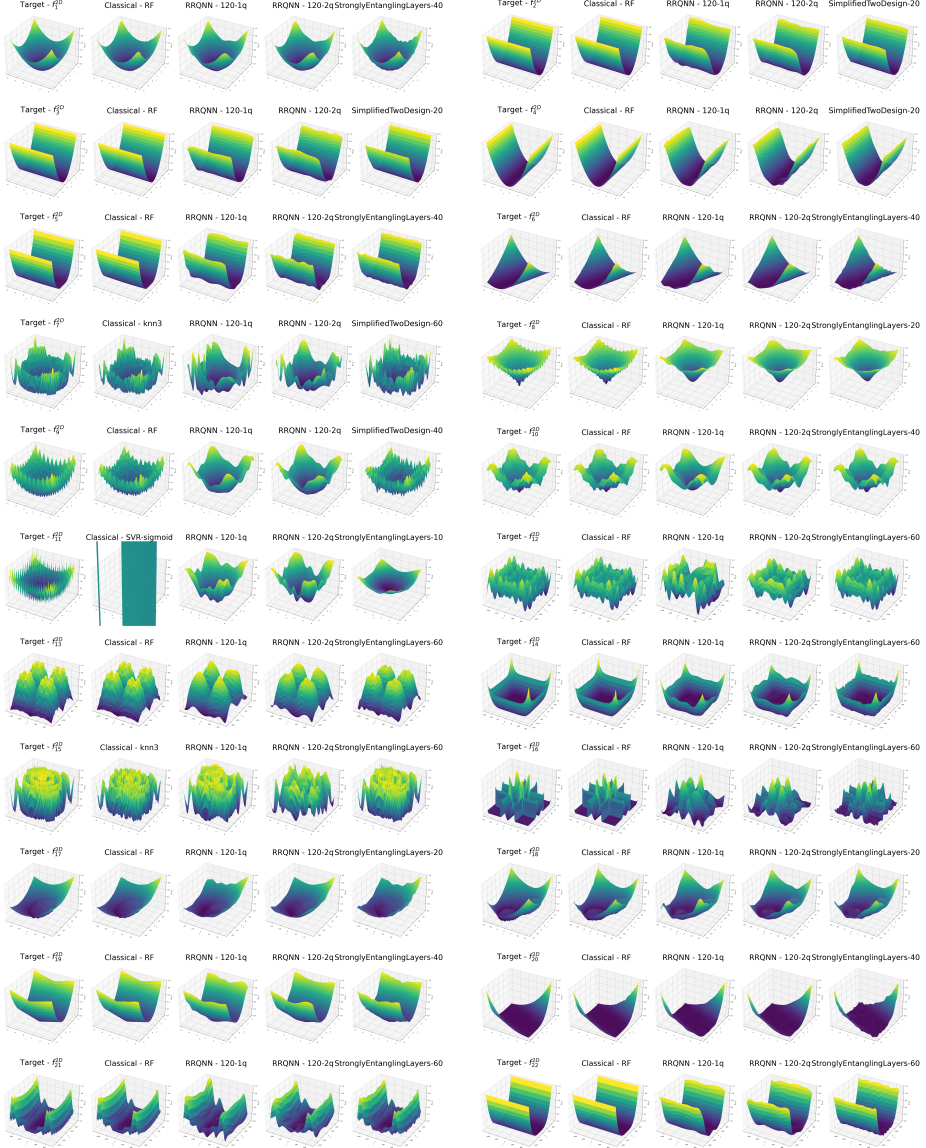


Fig. 10 Results of the best regression of 3D functions of the benchmark dataset by classical models, QNNs and the RRQNNs models.

of models when aggregated over functions, with classical tree-based and instance-based regressors consistently achieving lower ranks, while several quantum architectures occupy intermediate positions in the ranking.

Notably, deeper instances of the *StronglyEntanglingLayers* and selected *RRQNN* configurations exhibit competitive performance on a subset of functions, as reflected by localized regions of low rank values. At the same time, the variability observed across

rows highlights that no single model dominates uniformly over all regression tasks, reinforcing the importance of function-dependent and data-driven model selection strategies.

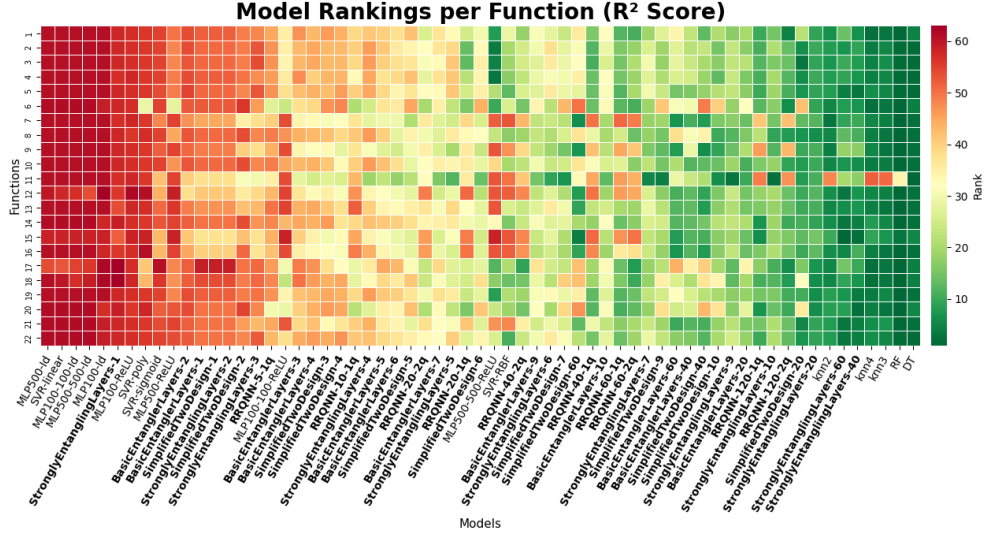


Fig. 11 Heatmap of model rankings based on the R^2 score across the 22 benchmark functions. Each cell represents the rank of a given model for a specific function, with lower ranks indicating better performance. The color scale ranges from red (higher rank, poorer performance) to green (lower rank, better performance). Models are ordered from left to right according to their average rank across all functions, and quantum models are highlighted by bold labels on the x-axis.

Table 3 presents a comprehensive ranking aggregation of all quantum and classical models across the 22 benchmark functions, computed via a rank-based methodology applied to mean R^2 scores. Within each function, models were assigned ranks based on their predictive performance, with rank 1 denoting the best-performing model. These per-function ranks were subsequently aggregated across all optimization landscapes to compute the mean rank and standard deviation of ranks for each model. The mean rank serves as a single-valued summary of overall model quality, while the standard deviation of ranks quantifies consistency of performance across heterogeneous problem domains. Models appearing in earlier positions demonstrate superior aggregate performance, whereas those with lower standard deviations exhibit more robust and generalizable behavior independent of function-specific characteristics. This rank-based aggregation is particularly valuable for comparative assessment across functions with disparate inherent difficulty, as ranking ensures equal weighting of each function regardless of problem hardness, thereby providing an unbiased evaluation of model performance across diverse regression tasks.

As expected, several classical models—notably decision trees, random forests, and nearest-neighbor regressors—occupy the top positions in the overall ranking, reflecting their strong and robust performance on a wide range of benchmark functions.

These models benefit from mature training procedures and flexible inductive biases that are well suited to the characteristics of the considered datasets. Nevertheless, it is noteworthy that a subset of quantum models, particularly instances of the *StronglyEntanglingLayers* and *SimplifiedTwoDesign* ansätze with moderate to large depths, achieve competitive average rankings, in some cases outperforming several classical baselines such as support vector regressors and multilayer perceptrons. An additional information from Table 3 is that the top ten positions in the average ranking are evenly split between classical and quantum models. Specifically, five of the ten best-ranked models correspond to classical regressors, while the remaining five are quantum neural network architectures. This balance indicates that, although classical methods remain highly competitive, appropriately designed quantum models can achieve comparable overall performance when evaluated across a diverse set of regression functions.

The ranking also reveals substantial variability among quantum architectures, emphasizing the importance of architectural choices in quantum regression. Deeper instances of the *StronglyEntanglingLayers* ansatz consistently rank higher than their shallow counterparts, suggesting that increased circuit depth plays a central role in capturing complex functional relationships. Similarly, the genetic-algorithm-generated RRQNN models are distributed across a wide range of ranks; however, the best-performing instances consistently correspond to architectures with larger parameter budgets and two-qubit configurations. This observation suggests that increased representational capacity and multi-qubit interactions play an important role in the effectiveness of evolved quantum regressors, while also reinforcing the motivation for automated architecture selection and meta-learning strategies.

From a broader perspective, these results suggest that quantum neural networks, when appropriately structured, can attain performance levels comparable to well-established classical models in regression tasks, albeit with a larger variance across architectures. While the average ranking does not imply systematic superiority of quantum models over classical ones, it supports the claim that quantum regressors constitute a viable and competitive modeling alternative within a heterogeneous model pool. This observation further motivates the use of data-driven model selection mechanisms, as discussed in subsequent sections, to identify those quantum architectures that are best suited to a given regression problem.

The results of the 22 functions provide strong evidence of the potential of quantum machine learning models, especially RRQNNs, to offer high accuracy with far fewer parameters compared to classical models. Classical models, such as Random Forests and Decision Trees, remain dominant in functions with smooth, monotonic relationships. However, quantum models, particularly deep circuits and RRQNNs, excel in more complex, non-linear tasks and can surpass classical models when the function requires intricate entangling transformations. These findings suggest that quantum machine learning has a significant role to play in tackling complex regression problems, offering a promising future for their application in real-world, resource-constrained settings. It is possible to see in Figure 10 the plotting of the 22 functions for each of the best classical, RRQNN, and RQN models found during the experiment.

7.1.1 Statistical Comparison Between Quantum and Classical Models

To deepen our understanding of the performance relationship between classical and quantum regressors, we applied the Wilcoxon signed-rank test to evaluate whether the predictive outputs of the two paradigms differ in a statistically meaningful way. The classical models included in this analysis whose average performance ranked above the quantum models in the global evaluation. This ensures that the statistical test focuses precisely on the most competitive classical baselines, i.e., those that empirically outperformed the quantum ansätze in the mean ranking. The Wilcoxon test then verifies whether such superior mean behavior is also reflected in statistically distinct predictive distributions.

Across all evaluated functions, Table D28 shows that none of the resulting p -values reach statistical significance at the $\alpha = 0.05$ threshold. This indicates that, even when the comparison is restricted to the best-performing classical models, the quantum and classical regressors exhibit statistically indistinguishable predictive distributions over repeated runs.

For Function 1, both comparisons involving `StronglyEntanglingLayers-20` against `knn4` and `knn3` resulted in p -values of 0.375 and 0.557, respectively. Even the deeper `StronglyEntanglingLayers-40` circuit produced a p -value of 0.064 when compared to `knn3`, which, although closer to the significance boundary, still fails to reject the null hypothesis. These results persist despite the fact that the selected classical models ranked above the quantum ones on average, highlighting the robustness of the statistical parity.

Function 2 includes a larger set of models, with depths up to 60 layers and multiple ansätze including `SimplifiedTwoDesign`. Yet the p -values remain comfortably above 0.05, ranging from 0.064 to 0.922. This again underscores that higher classical mean performance does not necessarily imply statistically different behavior across paired predictions. The variability across runs remains similar for both paradigms.

Functions 4 and 5 follow a comparable pattern. All comparisons between quantum circuits and the classical models that outperformed them on average yielded non-significant p -values. For example, the comparison between `SimplifiedTwoDesign-40` and `knn4` in Function 5 resulted in a p -value of 0.160, while comparisons with `knn2` yielded p -values as high as 0.625 and 0.375. These results extend to deeper circuits such as `StronglyEntanglingLayers-60`, again reinforcing the lack of evidence for any distributional shift.

Function 6 offers a particularly interesting case: in addition to variational quantum circuits, the hybrid recurrent quantum model `RRQNN-120-2q` is also included. Despite its distinct architecture, the statistical outcome aligns with the rest: p -values between 0.193 and 0.770 show no detectable difference relative to the top-performing classical baselines. This consistency suggests that, although quantum models often use drastically fewer trainable parameters, their predictive behavior remains statistically similar to that of the strongest classical competitors.

Function 11 provides one of the densest sets of comparisons, with quantum circuits of several depths evaluated against the classical decision tree, which ranked above all quantum models on average for this function. Yet even in this stringent scenario, all

p -values remain above 0.10, indicating that neither shallow nor deep quantum circuits produce distributions significantly different from the classical reference.

Finally, Function 16 continues to follow this global trend. The comparisons involving `SimplifiedTwoDesign-60` against `knn3` and `knn4` once again produce non-significant p -values (0.064 and 0.193). Although the $p = 0.064$ case is relatively close to the significance threshold, it nonetheless aligns with the unified statistical picture emerging from all functions.

Overall, these findings allow us to draw two main conclusions. First, even when the analysis is restricted to *the strongest classical models* — those that achieved higher average performance than quantum models in the global ranking — the Wilcoxon signed-rank test provides no evidence of statistically significant differences in predictive output distributions. Second, the empirical similarity across repeated runs suggests that quantum regressors, despite using considerably fewer trainable parameters and fundamentally different representational mechanisms, can match the classical models in terms of stability and distributional behavior. This reinforces the view that variational quantum models are not only expressive but also statistically reliable approximators in the regression tasks considered.

Across the 22 benchmark functions, the quantum models were competitive in 7 cases—exhibiting result distributions that were statistically indistinguishable from the best classical models—while in 1 function the quantum model outperformed all classical counterparts in terms of average performance.

7.2 Analysis of Similarity between generated RRNQQ architectures

The ten best RRQNN architectures produced by the genetic algorithm for each of the twenty-two nonlinear benchmark functions were analyzed in terms of structural similarity using unsupervised clustering methods. The underlying hypothesis was that architectures achieving high predictive accuracy—quantified by elevated R^2 scores for a given target function—would exhibit convergent structural patterns and, consequently, would be assigned to the same cluster based on similarities in their operator sequences. If the genetic algorithm consistently discovered effective architectural pattern for a specific problem, these patterns should naturally form coherent clusters independent of the clustering algorithm used.

To evaluate this hypothesis, three clustering techniques were employed: KMeans, Birch, and Agglomerative Clustering, applied to the 220 architectures distributed across the twenty-two target functions. After clustering these architectures into twenty-two groups, the results revealed low values for the Silhouette coefficient, which is internal evaluation metrics that do not depend on the expected labels. Likewise, external clustering indices such as Adjusted Rand Index (ARI), Jaccard and Fowlkes–Mallows, which quantify how closely the cluster structure aligns with the underlying function for which each architecture was optimized, also indicated that the clusters did not reflect architectural performance.

Two complementary experiments were conducted. In the first experiment, each architecture was represented using the full operator-type encoding of the quantum circuit, as explained in Section 5.2, i.e. with integers 1 – 13 denoted, respectively,

the identity operation (Id), single-qubit rotations for input encoding (R_x, R_y, R_z), single-qubit rotations for parameter encoding (R_x, R_y, R_z), and their corresponding controlled operations (CRX, CRY, CRZ, CRX, CRY, CRZ). This representation preserved the full expressiveness of the architectural search space and allowed the clustering algorithms to explore fine-grained structural similarities.

In the second experiment, each architecture was binarized: gates associated with input encoding were mapped to 0, while gates associated with parameter encoding were mapped to 1. This coarse representation was designed to test whether successful architectures share positional regularities—such as preferred locations for input loading or parameter insertion—regardless of the specific unitary type used.

Across all experiments, the conclusions were consistent: no significant similarity structure emerged among the architectures generated by the genetic algorithm. The results showed that even when the number of parameters defining each architecture was reduced (e.g., 20 or 40 operators), the clustering validity indices, although slightly higher, remained too low to support meaningful grouping. These observations suggest that effective RRQNN architectures do not converge to a stable or recurrent motif and that the architectural search landscape explored by the genetic algorithm remains highly irregular.

7.2.1 Analysis of Clustering Metrics

Tables C24, C25, C26, and C27 summarize the clustering metrics for the RRQNN architectures under four conditions: single-qubit (1q) architectures in their original operator encoding, single-qubit architectures after binarization, two-qubit (2q) architectures in their original encoding, and two-qubit architectures after binarization. These tables provide a comprehensive view of how architectural similarity behaves across different model complexities and representation schemes.

For the 1q architectures in their original encoding (Table C24), the Silhouette values are consistently low across all clustering algorithms, ranging from approximately 0.004 to 0.214. The Adjusted Rand Index (ARI), which measures alignment with the expected labels (i.e., the function each architecture was optimized for), remains extremely small, often close to zero or even negative. These results indicate that the architectural structures do not form coherent or natural clusters when the full operator information is used. Birch and AgglomerativeClustering occasionally produce slightly higher ARI values than KMeans, but the differences remain negligible in absolute terms.

When the 1q architectures are binarized (Table C25), the clustering quality remains similarly low. The Silhouette values do not improve, and the ARI remains close to zero. The binarization was expected to highlight macro-level positional similarities between input-loading and parameter-loading operations, but the results suggest that no such positional regularities exist across the datasets. In particular, even for reduced architecture sizes (5 or 10 operators), where one might expect more structural regularity, the clustering indices remain weak.

The 2q architectures in their original encoding (Table C26) also exhibit low Silhouette and ARI scores. Interestingly, for very small architectures (20 operators), the silhouette values increase slightly (around 0.051–0.054), and the ARI also increases

modestly compared to larger architectures. However, these values remain far from those typically associated with meaningful clustering. For larger architectures (40, 60, 120 operators), the Silhouette and ARI values again approach zero, suggesting that architectural diversity increases with the number of operators and that the genetic algorithm does not converge toward a consistent structural pattern.

Finally, the 2q binarized architectures (Table C27) show similar behavior: low Silhouette values, low ARI, and no evidence of meaningful structural regularity. The slight increase in Fowlkes–Mallows scores for small architectures (20 operators) again indicates that reducing architectural complexity can impose weak structural regularities, but these effects remain small and insufficient for any useful predictive interpretation.

Overall, the clustering metrics across all four tables demonstrate a consistent pattern: the RRQNN architectures exhibit high variability, and the genetic algorithm does not converge to a stable architectural template that can be detected through unsupervised clustering. Even architectures that achieve high predictive performance do not share enough structural similarity to form coherent clusters in either their full or binarized representations.

These findings underscore the inherent difficulty of designing RRQNN architectures capable of reliably solving nonlinear regression problems. The absence of consistent clustering structure suggests that high-performing architectures may be highly problem-specific and that generalized architectural motifs are unlikely to emerge from purely evolutionary search processes.

7.3 Analysis of QNN Performance by size

We checked the average behavior and its standard deviation of the 3 quantum neural network models used in Figures 12 and 13 for each of the 22 benchmark functions. It is possible to verify that there is an alternation of higher R^2 -score between the SimplifiedTwoDesign and StronglyEntanglingLayers models, but the BasicEntanglingLayers model is almost always in second place in performance. The exceptions occur in function 8, when BasicEntanglingLayers ties with SimplifiedTwoDesign for second place, and in functions 12, 13, 15 and 17 when it is in third place. Therefore, a total of 18 times BasicEntanglingLayers is in second place. It is also possible to see that sometimes increasing the number of layers does not mean increasing performance (increasing R^2 score) in the BasicEntanglingLayers and SimplifiedTwoDesign models. The StronglyEntanglingLayers model generally benefits (increases its R^2 score) as the number of layers increases. It's even possible that the performance of function 12 could be improved if the number of layers in this model were increased, since the performance curve is still showing strong growth in the 60th repetition of layers (which doesn't seem to be the same behavior in function 13, where the performance of all 3 models seems to have converged).

An important point also analyzed in these graphs is that, despite the models not finding a high average value in some functions, within the 10 executions performed, it was still possible to find the maximum R^2 -score, which suggests that the parametric

initialization and the data used to train the models may prevent the data from converging to an optimal scenario. To see this situation, look at the standard deviation bar in the curves for functions 1, 5, 10, and 14.

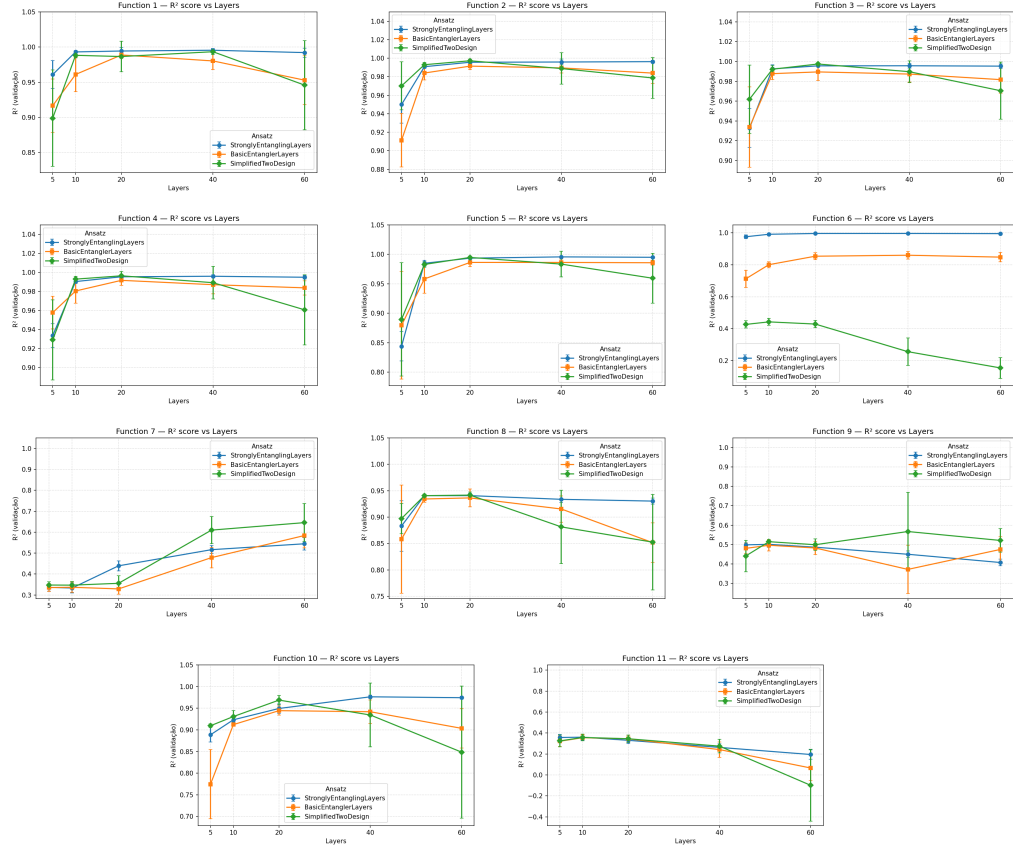


Fig. 12 Analysis of the R^2 -Score for functions 1 to 11 (Mean and standard deviation across 10 runs).

7.4 Defining best quantum architecture by dataset features

In this section, we conducted a meta-learning analysis of five predictive scenarios, each designed to evaluate the ability of regression complexity measures to guide the automatic selection of quantum regression models. Across all scenarios, a classifier receives the same set of twelve meta-features introduced in Section 4, yet its prediction targets vary according to the architectural decision being automated. The objective is to determine whether the regression complexity descriptors contain sufficient information to discriminate between different quantum architectures, depths, and resource constraints. For each scenario, a Leave-One-Out Cross-Validation (LOOCV) protocol is used, and performance is compared against the accuracy of a naive majority-class

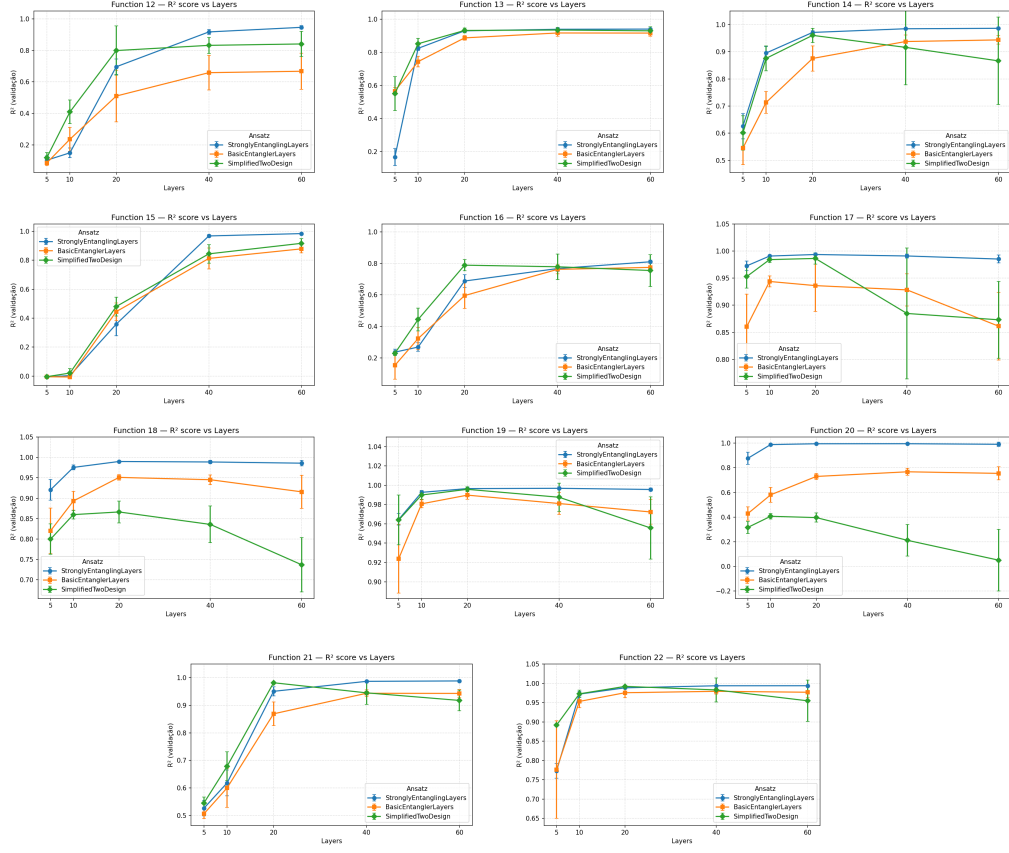


Fig. 13 Analysis of the R^2 -Score for functions 12 to 22 (Mean and standard deviation across 10 runs).

predictor. For each of the $\binom{12}{k}$ subsets of size k , a Random Forest classifier was trained on 21 instances and tested on the remaining one. The average LOOCV accuracy was computed over the 22 splits and reported.

7.4.1 Scenario 1: Selecting the Best QNN Ansatz Among Two Leading Architectures

The first scenario concerns the problem of selecting, for each dataset, the best-performing ansatz between the two highest-ranked quantum model families: the *StronglyEntanglingLayers* and the *SimplifiedTwoDesign* architectures. Across the 22 benchmark functions considered, the former achieved the best regression performance in 17 cases and the latter in 5, yielding a naive majority-class baseline of 77.27%. The meta-learning classifier, trained on the twelve complexity measures, surpasses this baseline when the appropriate subsets of features are used. Three combinations

of complexity metrics achieve optimal LOOCV accuracy (100%):

$$(i) (c1, c3, l1, s3, s4, t2), \quad (36)$$

$$(ii) (c2, c3, l1, s3, s4, t2), \quad (37)$$

$$(iii) (c1, c2, c3, s1, s3, l3, s4). \quad (38)$$

The first two solutions share six metrics and differ only by substituting $c1$ with $c2$, whereas the third subset contains seven metrics but preserves the same structural components: global complexity indicators ($c1, c2, c3$), smoothness and local complexity descriptors ($s1, s3, s4$), and at least one landmarking-based nonlinearity measure ($l1$ or $l3$). These results indicate that optimal predictive accuracy arises from a stable configuration of complementary meta-features, rather than from arbitrary or isolated combinations.

The distribution of accuracies as a function of subset size is summarized in the violin plot shown in Figure 14, which reveals substantial variability across subset sizes but also isolated regions of optimal predictive performance.

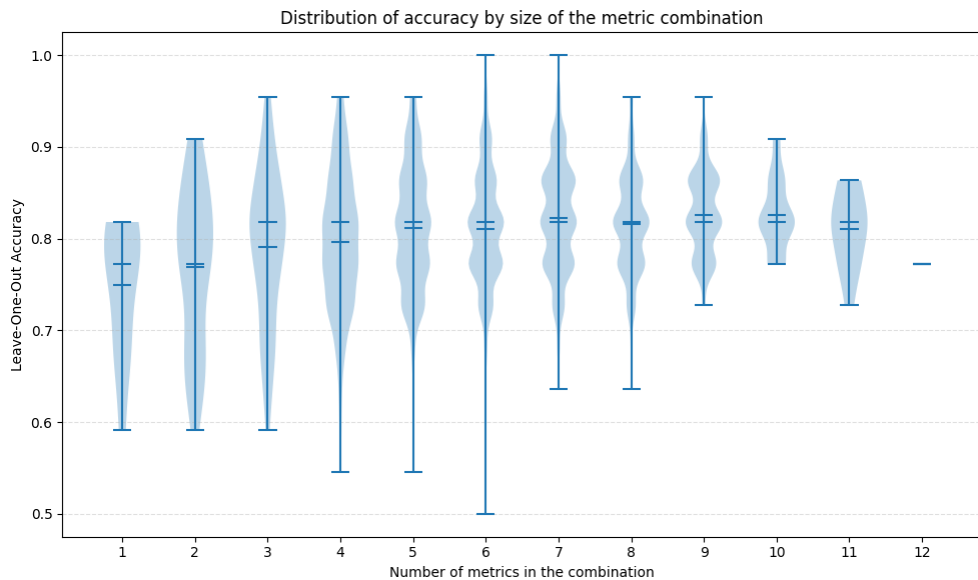


Fig. 14 Violin plot of the number of metric combinations and their respective accuracy results when evaluated to determine which quantum circuit to use to solve the 22 nonlinear functions.

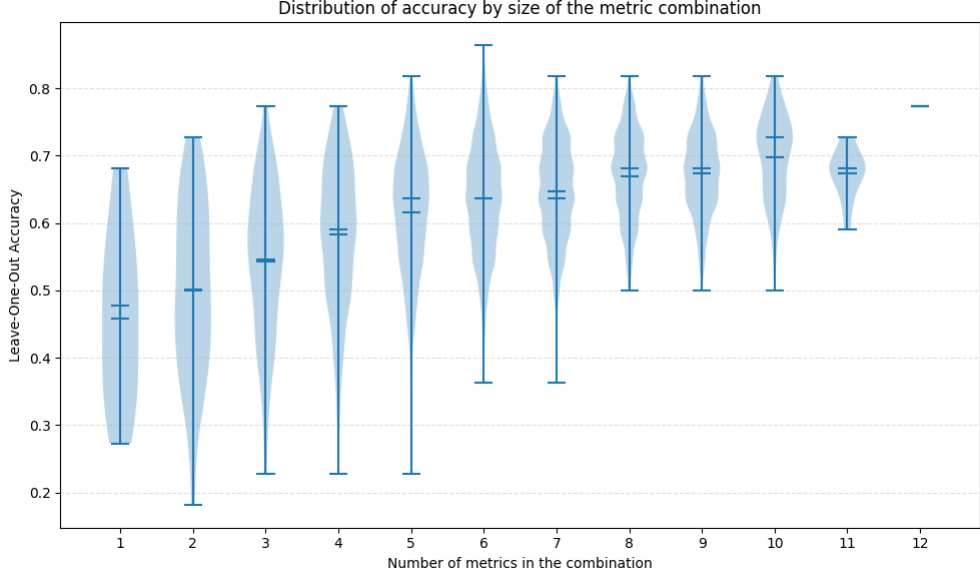


Fig. 15 Violin plot of the number of metric combinations and their respective accuracy results when evaluated to determine which RRQNN architecture (considering maximum operators and qubit count) should be selected to solve the 22 nonlinear benchmark functions.

7.4.2 Scenario 2: Selecting the Best RRQNN Model Under Operator and Qubit Constraints

The second scenario evaluates the ability of the meta-learner to determine the best RRQNN variant among four competing configurations, each defined by its maximum number of quantum operators and number of qubits. Here is the frequency of each class: RRQNN-120-2q: 11, RRQNN-120-1q: 7, RRQNN-20-2q: 3, RRQNN-40-1q: 1. The majority-class baseline is 0.50. Two feature subsets yield the best LOOCV accuracy (0.8636), far surpassing the baseline:

$$(c1, c3, l2, s1, l3, s4), \quad (c2, c3, l2, s1, l3, s4). \quad (39)$$

Both optimal subsets share six complexity measures, differing only in the substitution of $c1$ and $c2$, mirroring the pattern observed in Scenario 1. Once again, the decisive role of $c3$, $s1$, $s4$, and higher-order linearity descriptors ($l2$, $l3$) suggests that the RRQNN architectural landscape is strongly governed by a mixture of global structure, local smoothness, and landmarking behavior.

The distribution of accuracies as a function of subset size is summarized in the violin plot shown in Figure 15, which reveals substantial variability across subset sizes but also clear clusters of high-performing combinations capable of surpassing the majority-class baseline, thereby demonstrating that the complexity measures encode discriminative information regarding operator budget and qubit allocation in RRQNN models.

7.4.3 Scenario 3: Determining the Optimal Number of Qubits in RRQNN Models

In this scenario, the classifier must choose between one- and two-qubit RRQNN architectures. The empirical distribution of best models is '2q': 14, and '1q': 8, yielding a majority baseline of 0.6364. Remarkably, three metric subsets achieve optimal LOOCV accuracy (1.0):

$$(c1, c2, c3, l2, l3, s4), \quad (40)$$

$$(c1, c3, l2, l3, s4, t2), \quad (41)$$

$$(c2, c3, l2, l3, s4, t2). \quad (42)$$

These combinations reflect the same structural template observed in Scenarios 1 and 2: a core of global complexity indicators ($c1, c2, c3$), smoothness/nonlinearity descriptors ($s4$), and landmark metrics ($l2, l3$), with $t2$ acting as a stabilizing topological descriptor in two of the three optimal subsets. The consistent emergence of this motif across scenarios suggests that the number of qubits required for optimal regression behavior is highly dependent on the global complexity profile of the dataset.

Figure 16 shows that only subsets containing six meta-features were able to achieve 100% accuracy, whereas all smaller subsets yielded lower performance. The figure further shows that as more meta-features are incorporated, the variability in accuracy decreases, reinforcing the role of richer complexity information in enabling reliable qubit-selection decisions.

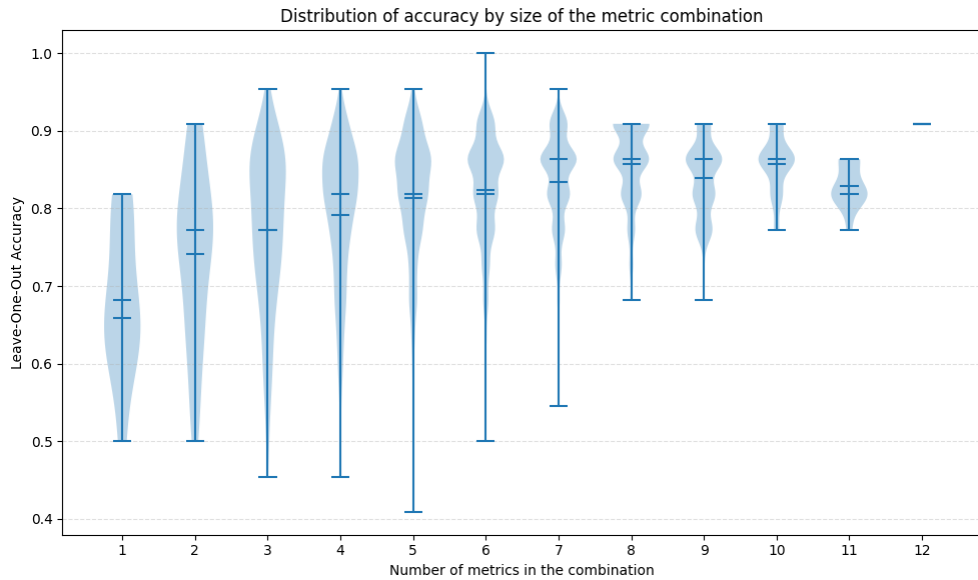


Fig. 16 Violin plot of the number of metric combinations and their respective accuracy results when evaluated to determine whether a one-qubit or two-qubit RRQNN architecture should be used to solve the 22 nonlinear benchmark functions.

7.4.4 Scenario 4: Selecting the Best Overall Quantum Model Considering Architecture and Depth

A more challenging classification task arises when the meta-learner must select, among all quantum models and depths tested, the best-performing configuration for each dataset. The empirical distribution of winners is: StronglyEntanglingLayers-40: 5, StronglyEntanglingLayers-60: 5, SimplifiedTwoDesign-20: 4, StronglyEntanglingLayers-20: 4, SimplifiedTwoDesign-40: 3, RRQNN-120-2q: 1, yielding a naive baseline of 0.17 (or 0.20 if we ignore the lone RRQNN winner). The best LOOCV accuracy achieved by any subset of meta-features is 0.5455, obtained by the following combinations:

$$(c1, c2, c3, s1), \quad (c1, c3, s1, t2), \quad (c2, c3, s1, t2), \quad (43)$$

$$(c1, c2, c3, s1, s3), \quad (c1, c2, c3, s1, t2), \quad (c1, c2, c3, s1, s3, s4). \quad (44)$$

Although lower than in the first three scenarios, the predictive accuracy remains significantly above the majority baseline and demonstrates that complexity measures can meaningfully guide model-depth selection, even when the decision space is substantially larger.

Figure 17, which reveals substantial variability across subset sizes but also nontrivial pockets of above-baseline predictive accuracy. In particular, the highest accuracy levels are concentrated around combinations of 4, 5, and 6 meta-features, whereas nearly all subset sizes exhibit considerable dispersion in performance. This high degree of variability reflects the difficulty of this predictive scenario, where the classifier must discriminate among a broad and heterogeneous set of quantum architectures and depth configurations. Even under these challenging conditions, the meta-features still retain some discriminative power for identifying the architecture-depth pair.

7.4.5 Scenario 5: Selecting the Best Quantum Model Without Considering Depth

Finally, we collapse all layer-dependent variants into their respective architectural families, yielding the class distribution: StronglyEntanglingLayers: 14, SimplifiedTwoDesign: 6, RRQNN-120-2q: 2, with a majority baseline of 0.6364. The best LOOCV performance achieved by the meta-learner is 0.8182, associated with two feature subsets:

$$(c3, s3), \quad (c1, c2, c3, s1, s3). \quad (45)$$

In contrast to previous scenarios, here a two-feature subset is already sufficient to surpass the naive baseline by a large margin, indicating that key distinctions across architectural families may be captured by a small set of highly informative regression complexity measures.

Figure 18, which reveals substantial variability across subset sizes but also regions of markedly enhanced predictive accuracy, thus demonstrating that the complexity metrics remain informative even when the task is reduced to distinguishing among architectural families independent of their layer configurations.

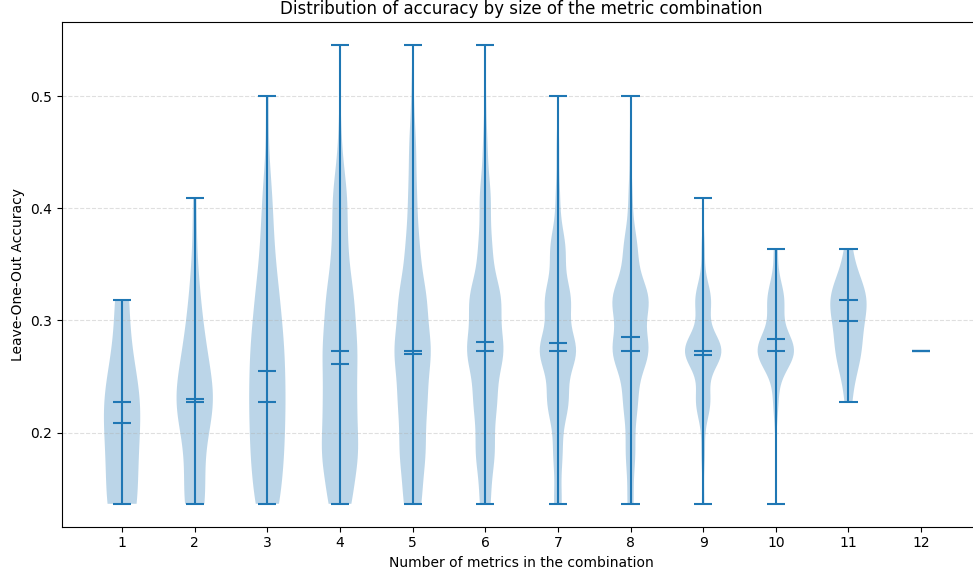


Fig. 17 Violin plot of the number of metric combinations and their respective accuracy results when evaluated to determine which quantum model and layer configuration achieves the best performance across the 22 nonlinear benchmark functions.

7.4.6 Discussion

Across all five scenarios, several consistent patterns emerge. First, the C -family metrics—particularly $C3$ —appear essential for predicting which quantum architecture will succeed on a given dataset. Second, smoothness and nearest-neighbor-based descriptors from the S family ($S1$, $S3$, $S4$) occur in nearly all high-performing subsets, highlighting the role of local geometric structure in governing quantum expressivity. Third, landmarking-based linearity indicators ($L1$, $L2$, $L3$) regularly appear in the optimal combinations, suggesting that the behavior of simple learners on the dataset provides powerful discriminative information. Finally, the ability of the meta-learner to exceed all majority-class baselines—often by a substantial margin—demonstrates that regression complexity measures contain highly actionable information for guiding quantum model selection, even in the presence of significant architectural variability and limited training examples.

The results reported in this section are obtained from a specific set of benchmark regression functions and therefore motivate further analysis on more diverse and generic datasets. Extending the evaluation to problems with different statistical properties, dimensionalities, and data-generation mechanisms will be important to better characterize the scope and generality of the proposed meta-learning approach.

At the same time, the observed performance trends indicate that structural descriptors of regression datasets capture information that is relevant for quantum architecture selection, suggesting that dataset-level characteristics can be exploited to inform the choice of suitable quantum ansätze in regression tasks.

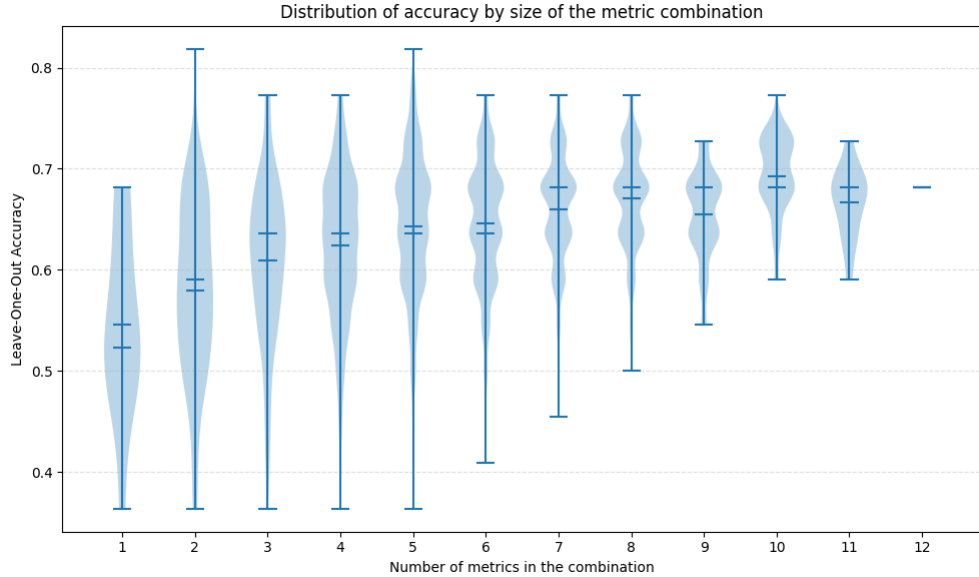


Fig. 18 Violin plot of the number of metric combinations and their respective accuracy results when evaluated to determine which quantum model architecture—regardless of its number of layers—should be selected to solve the 22 nonlinear benchmark functions.

8 Conclusion

In this work, it was possible to analyze the behavior of variational quantum neural networks applied to a benchmark of 22 non-linear function regression problems, with a variety of behaviors, including non-continuous, non-separable, and multimodal. An approach for defining reduced regression quantum neural networks (RRQNN) was proposed based on a search performed by Genetic Algorithms. The quantum models were compared with 17 classical baseline models. The results were extensively evaluated and compared, verifying the high impact of the number of parameters required for a classical model to perform the regression compared to the quantum model. Through statistical testing, it was possible to verify that although the average of the quantum models was not always greater than that of the classical models, there is statistical equivalence in 7 of the 22 functions.

It was verified that the RRQNN networks found by the Genetic Algorithm had good comparative results (resulting in the best quantum model in one of the scenarios). However, it was possible to assess that the circuits found did not have a significant pattern, based on the execution of 3 unsupervised clustering algorithms, and analyzing 4 metrics that evaluate the quality of the generated clusters.

It was also possible to verify that there is information (meta-features) in the databases that suggests identifying which quantum neural network layer can be used to maximize performance. We performed an exhaustive test combinatorially varying

12 metrics established in the literature, and verified that there are 3 combinations that achieve an optimal choice between the two best quantum models evaluated.

Based on all the analysis conducted, it is possible to conclude that quantum models are very promising in modeling nonlinear problems, being equivalent to or better than almost all classical models evaluated, performing the task, after training, with much smaller parameters. There are challenging factors in this area, among which we can point out as main ones the definition of layers (repetitions of their layers), premature convergence at barren plateaus due to sensitivity to training conditions, the lack of standardization of architectures that best solve the problems, and the training time due to the need to simulate the models in classical environments. This work paves the way for future work connected to the computability of variational quantum models and improved training.

As future work, several extensions of the present study are envisioned. First, the analysis can be expanded to regression problems with higher-dimensional input spaces and more complex functional structures, allowing a deeper assessment of the scalability of automatically synthesized quantum neural networks. In this context, an important research direction is the automation of meta-feature selection itself. The exhaustive searches conducted in this work indicate that specific subsets of regression complexity measures can optimally discriminate between competing quantum architectures. Future studies may therefore investigate principled mechanisms for automatically selecting or learning these meta-features, further strengthening the meta-learning framework for quantum model selection.

Moreover, the present study focuses on a restricted search space in terms of qubit count and circuit depth, and all experiments are performed under noiseless simulation. Extending the analysis to larger circuit architectures, higher-dimensional input spaces, and noisy quantum hardware constitutes a critical next step toward evaluating the practical viability of the proposed approach. In this direction, combining error-prediction strategies for noisy quantum processors [57] with data-driven circuit-construction methodologies based on meta-features represents a promising avenue. Incorporating hardware-aware constraints, realistic noise models, and error-mitigation techniques directly into the metalearning loop may substantially improve the robustness and reliability of automatically synthesized quantum models.

Finally, although the comparison with classical regressors highlights the parameter efficiency of quantum neural networks, a tighter integration with classical metalearning pipelines remains an open challenge. Exploring connections with established techniques such as neural architecture search, ensemble-based model selection, and Bayesian optimization could provide deeper insights into when and why quantum models offer advantages over classical alternatives. Collectively, these directions point toward the development of principled, scalable, and hardware-adaptive metalearning frameworks for quantum regression, helping to bridge the gap between quantum machine learning and mature automated learning methodologies in the classical domain.

Acknowledgements. Fernando M. de Paula Neto acknowledges financial support from the Brazilian National Council for Scientific and Technological Development (CNPq) under Grant No. 408499/2025-7. Fernando M. de Paula Neto is also a

researcher affiliated with the National Institute of Science and Technology for Applied Quantum Computing, supported by CNPq under Grant No. 408884/2024-0. Fernando M. de Paula Neto and Paulo Mattos are part of the Brazilian National Institute for Artificial Intelligence, supported by CNPq under Grant No. 406417/2022-9. Paulo Mattos also acknowledges financial support from CNPq for an academic project under Grant No. 306934/2025-6. Felipe Fanchini acknowledges financial support from the National Institute of Science and Technology for Applied Quantum Computing through CNPq process No. 408884/2024-0, and from the São Paulo Research Foundation (FAPESP), under grant numbers 2023/04987-6 and 2024/00998-6. Felipe Fanchini also acknowledges support from the Office of Naval Research Global (ONR Global) and the Air Force Office of Scientific Research (AFOSR), grant No. N62909-24-1-2012.

Declarations

The authors declare no conflict of interest.

The data generated are detailed in the article.

FMPN conceived the idea, conducted the experiments, and wrote the article. LRS, PSGMN, and FFF contributed to the writing and revision of the manuscript, with LRS also participating in the experimental execution.

Appendix A Results for 1D functions

The detailed numerical results of the proof-of-concept experiments discussed in Section 6.4 are in Table A1.

Appendix B Results for 3D functions

The detailed numerical results for each of the 22 benchmark regression datasets are reported in Tables B2–B23. Each table corresponds to one benchmark function and summarizes the performance of all evaluated models under the experimental protocol described in this work.

Appendix C Similarity between architectures generated by genetic algorithms - Clustering Checking

Tables C27 and C26 report the clustering metrics obtained for RRQNN architectures with two qubits, considering both binarized and non-binarized architectural representations across different operator counts and clustering algorithms. Analogously, Tables C25 and C24 summarize the corresponding results for single-qubit RRQNNs, enabling a comparative analysis of how architectural representation, parameter count, and qubit configuration influence the clustering behavior of evolved quantum models. A detailed discussion of these clustering results is provided in Section 7.2.

Appendix D Statistical comparing tests

Table D28 reports the results of the Wilcoxon statistical tests comparing quantum and classical regression models, which are discussed in detail in Section 7.1.1.

References

- [1] Shor, P.W.: Polynomial-time algorithms for prime factorization and discrete logarithms on a quantum computer. *SIAM Journal on Computing* **26**(5), 1484–1509 (1997) <https://doi.org/10.1137/S0097539795293172>
- [2] Du, Y., Hsieh, M., Liu, T., Tao, D.: Expressive power of parametrized quantum circuits. *Physical Review Research* **2**(3), 033125 (2020) <https://doi.org/10.1103/PhysRevResearch.2.033125>
- [3] Biamonte, J., Wittek, P., Pancotti, N., Rebentrost, P., Wiebe, N., Lloyd, S.: Quantum machine learning. *Nature* **549**(7671), 195–202 (2017)
- [4] Barreto, A.G., Fanchini, F.F., Papa, J.P., Albuquerque, V.H.C.: Why consider quantum instead classical pattern recognition techniques? *Applied Soft Computing* **165**, 112096 (2024)
- [5] Havlíček, V., Córcoles, A.D., al., K.T.: Supervised learning with quantum-enhanced feature spaces. *Nature* **567**, 209–212 (2019) <https://doi.org/10.1038/s41586-019-0980-2>
- [6] Liu, Y., Arunachalam, S., Temme, K.: A rigorous and robust quantum speed-up in supervised machine learning. *Nature Physics* **17**(9), 1013–1017 (2021)
- [7] Abbas, A., Sutter, D., Zoufal, C., Lucchi, A., Figalli, A., Woerner, S.: The power of quantum neural networks. *Nature Machine Intelligence* **3**, 1–9 (2021) <https://doi.org/10.1038/s42256-021-00302-1>
- [8] Ding, C., Wang, S., Wang, Y., Gao, W.: Quantum machine learning for multiclass classification beyond kernel methods. *Physical Review A* **111**(6), 062410 (2025)
- [9] Lin, C.-H., Tang, P.-W., Huete, A.R.: Quantum feature-empowered deep classification for fast mangrove mapping. *IEEE Transactions on Geoscience and Remote Sensing* (2024)
- [10] Onim, M.S.H., Humble, T.S., Thapliyal, H.: Quantum hybrid support vector machines for stress detection in older adults. In: 2025 IEEE International Conference on Consumer Electronics (ICCE), pp. 1–4 (2025). IEEE
- [11] Röseler, P., Schaudt, O., Berg, H., Bauckhage, C., Koch, M.: Efficient quantum convolutional neural networks for image classification: Overcoming hardware constraints. *arXiv preprint arXiv:2505.05957* (2025)

- [12] Chittoor, H.H.S., Griffin, P.R., Neufeld, A., Thompson, J., Gu, M.: Qultsf: Long-term time series forecasting with quantum machine learning. arXiv preprint arXiv:2412.13769 (2024)
- [13] Ciceri, A., Cottrell, A., Freeland, J., Fry, D., Hirai, H., Intallura, P., Kang, H., Lee, C.-K., Mitra, A., Ohno, K., et al.: Enhanced fill probability estimates in institutional algorithmic bond trading using statistical learning algorithms with quantum computers. arXiv preprint arXiv:2509.17715 (2025)
- [14] Hegade, N.N., Chen, X., Solano, E.: Digitized counterdiabatic quantum optimization. *Physical Review Research* **4**(4), 042030 (2022)
- [15] Simen, A., Flores-Garrigos, C., De Oliveira, M.H., Barrios, G.D.A., Hernández, J.F., Zhang, Q., Cadavid, A.G., Vives-Gilabert, Y., Martín-Guerrero, J.D., Solano, E., et al.: Quenched quantum feature maps. arXiv preprint arXiv:2508.20975 (2025)
- [16] Peruzzo, A., McClean, J., Shadbolt, P., Yung, M.-H., Zhou, X.-Q., Love, P.J., Aspuru-Guzik, A., O'Brien, J.L.: A variational eigenvalue solver on a photonic quantum processor. *Nature communications* **5**(1), 4213 (2014)
- [17] Tacchino, F., Macchiavello, C., Gerace, D., Bajoni, D.: An artificial neuron implemented on an actual quantum processor. *npj Quantum Information* **5**(1), 1–8 (2019)
- [18] Paula Neto, F.M., Ludermir, T.B., Oliveira, W.R., Silva, A.J.: Implementing any nonlinear quantum neuron. *IEEE transactions on neural networks and learning systems* **31**(9), 3741–3746 (2019)
- [19] Huggins, W., Patil, P., Mitchell, B., Whaley, K.B., Stoudenmire, M.: Towards quantum machine learning with tensor networks. *Quantum Science and Technology* **4**(2), 024001 (2019)
- [20] Cong, L., Choi, S., Lukin, M.D.: Quantum convolutional neural networks. *Nature Physics* **15**(12), 1273–1278 (2019)
- [21] Pérez-Salinas, A., Cervera-Lierta, A., Gil-Fuster, E., Latorre, J.I.: Data re-uploading for a universal quantum classifier. *Quantum* **4**, 226 (2020)
- [22] Gonon, L., Jacquier, A.: Universal approximation theorem and error bounds for quantum neural networks and quantum reservoirs. *IEEE Transactions on Neural Networks and Learning Systems* (2025)
- [23] Schuld, M., Swei, R., Meyer, J.: The effect of data encoding on the expressive power of variational quantum machine learning models (2020). arXiv preprint arXiv:2008.08605

- [24] Wang, J., Kim, M., Kais, S.: Information bottleneck of quantum neural networks. In: NeurIPS 2024 Workshop Machine Learning with New Compute Paradigms
- [25] Coyle, B., Mills, D., Danos, V., Kashefi, E.: The born supremacy: quantum advantage and training of an ising born machine. *npj Quantum Information* **6**(1), 60 (2020)
- [26] Ristè, D., Da Silva, M.P., Ryan, C.A., Cross, A.W., Córcoles, A.D., Smolin, J.A., Gambetta, J.M., Chow, J.M., Johnson, B.R.: Demonstration of quantum advantage in machine learning. *npj Quantum Information* **3**(1), 16 (2017)
- [27] Carvalho, J.H., Paula Neto, F.M.: Parametrized constant-depth quantum neuron. *IEEE Transactions on Neural Networks and Learning Systems* (2023)
- [28] Basilewitsch, D., Bravo, J.F., Tutschku, C., Struckmeier, F.: Quantum neural networks in practice: a comparative study with classical models from standard data sets to industrial images. *Quantum Machine Intelligence* **7**(2), 110 (2025)
- [29] Monteiro, C.A., Gustavo Filho, I., Costa, M.H.J., Paula Neto, F.M., Oliveira, W.R.: Quantum neuron with real weights. *Neural Networks* **143**, 698–708 (2021)
- [30] Sim, S., Johnson, P.D., Aspuru-Guzik, A.: Expressibility and entangling capability of parameterized quantum circuits for hybrid quantum-classical algorithms. *Advanced Quantum Technologies* **2**(12), 1900070 (2019)
- [31] McClean, J.R., Boixo, S., Smelyanskiy, V.N., Babbush, R., Neven, H.: Barren plateaus in quantum neural network training landscapes. *Nature communications* **9**(1), 4812 (2018)
- [32] Zhang, S., Hsieh, C., Zhang, S., Yao, H.: Neural predictor based quantum architecture search. *Machine Learning: Science and Technology* **2**(4), 045027 (2021) <https://doi.org/10.1088/2632-2153/ac28dd>
- [33] He, Z., Chen, C., Li, Z., Situ, H., Zhang, F., Zheng, S., Li, L.: A meta-trained generator for quantum architecture search. *EPJ Quantum Technology* **11**(44) (2024) <https://doi.org/10.1140/epjqt/s40507-024-00255-9>
- [34] Martyniuk, D., Jung, J., Paschke, A.: Quantum architecture search: A survey. In: *IEEE International Conference on Quantum Computing and Engineering (QCE)* (2024). <https://doi.org/10.1109/QCE60285.2024.00198>
- [35] Sun, X., Tian, G., Yang, S., Yuan, P., Zhang, S.: Asymptotically optimal circuit depth for quantum state preparation and general unitary synthesis. *IEEE Transactions on Computer-Aided Design of Integrated Circuits and Systems* **42**(10), 3301–3314 (2023)

- [36] Zhang, S.-X., Hsieh, C.-Y., Zhang, S., Yao, H.: Differentiable quantum architecture search. *Quantum Science and Technology* **7**(4), 045023 (2022)
- [37] Ostaszewski, M., Trenkwalder, L.M., Masarczyk, W., Scerri, E., Dunjko, V.: Reinforcement learning for optimization of variational quantum circuit architectures. *Advances in neural information processing systems* **34**, 18182–18194 (2021)
- [38] Sotoca, J.M., Mollineda, R.A., Sánchez, J.S.: A meta-learning framework for pattern classification by means of data complexity measures. *Inteligencia Artificial. Revista Iberoamericana de Inteligencia Artificial* **10**(29), 31–38 (2006)
- [39] Nielsen, M.A., Chuang, I.L.: *Quantum Computation and Quantum Information*. Cambridge university press, ??? (2010)
- [40] Schuld, M., Petruccione, F.: *Machine Learning with Quantum Computers* vol. 676. Springer, ??? (2021)
- [41] Grant, E., Benedetti, M., Cao, S., Hallam, A., Lockhart, J., Stojovic, V., Green, A.G., Severini, S.: Hierarchical quantum classifiers. *npj Quantum Information* **4**(1), 65 (2018)
- [42] Schuld, M., Sweke, R., Meyer, J.J.: Effect of data encoding on the expressive power of variational quantum-machine-learning models. *Physical Review A* **103**(3), 032430 (2021)
- [43] Ballarin, M., Mangini, S., Montangero, S., Macchiavello, C., Mengoni, R.: Entanglement entropy production in quantum neural networks. *Quantum* **7**, 1023 (2023)
- [44] Lloyd, S., Schuld, M., Ijaz, A., Izaac, J., Killoran, N.: Quantum embeddings for machine learning. *arXiv preprint arXiv:2001.03622* (2020)
- [45] Panadero, I., Ban, Y., Espinós, H., Puebla, R., Casanova, J., Torrontegui, E.: Regressions on quantum neural networks at maximal expressivity. *Scientific Reports* **14**(1), 31669 (2024) <https://doi.org/10.1038/s41598-024-81436-5>
- [46] Schuld, M., Bocharov, A., Svore, K.M., Wiebe, N.: Circuit-centric quantum classifiers. *Physical Review A* **101**(3), 032308 (2020)
- [47] Bergholm, V., Izaac, J., Schuld, M., Gogolin, C., Ahmed, S., Ajith, V., Alam, M.S., Alonso-Linaje, G., AkashNarayanan, B., Asadi, A., Arrazola, J.M., Azad, U., Banning, S., Blank, C., Bromley, T.R., Cordier, B.A., Ceroni, J., Delgado, A., Di Matteo, O., Dusko, A., Garg, T., Guala, D., Hayes, A., Hill, R., Ijaz, A., Isacsson, T., Ittah, D., Jahangiri, S., Jain, P., Jiang, E., Khandelwal, A., Kottmann, K., Lang, R.A., Lee, C., Loke, T., Lowe, A., McKiernan, K., Meyer, J.J., Montañez-Barrera, J.A., Moyard, R., Niu, Z., O’Riordan, L.J., Oud, S., Panigrahi, A., Park, C.-Y., Polatajko, D., Quesada, N., Roberts, C., Sá, N.,

Schoch, I., Shi, B., Shu, S., Sim, S., Singh, A., Strandberg, I., Soni, J., Száva, A., Thabet, S., Vargas-Hernández, R.A., Vincent, T., Vitucci, N., Weber, M., Wierichs, D., Wiersema, R., Willmann, M., Wong, V., Zhang, S., Killoran, N.: PennyLane: Automatic differentiation of hybrid quantum-classical computations (2022). <https://arxiv.org/abs/1811.04968>

[48] Cerezo, M., Sone, A., Volkoff, T., Cincio, L., Coles, P.J.: Cost function dependent barren plateaus in shallow parametrized quantum circuits. *Nature communications* **12**(1), 1791 (2021)

[49] Brazdil, P., Van Rijn, J.N., Soares, C., Vanschoren, J.: Metalearning: Applications to Automated Machine Learning and Data Mining. Springer, ??? (2022)

[50] Lorena, A.C., Maciel, A.I., Miranda, P.B., Costa, I.G., Prudêncio, R.B.: Data complexity meta-features for regression problems. *Machine Learning* **107**(1), 209–246 (2018)

[51] Komorniczak, J., Ksieniewicz, P.: proplexity—an open-source python library for supervised learning problem complexity assessment. *Neurocomputing* **521**, 126–136 (2023)

[52] Hastie, T., Tibshirani, R., Friedman, J.: *The Elements of Statistical Learning: Data Mining, Inference, and Prediction*, 2nd edn. Springer, ??? (2009). <https://doi.org/10.1007/978-0-387-84858-7>

[53] Huang, H.-Y., Broughton, M., Cotler, J., Chen, S., Li, J., Mohseni, M., Neven, H., Babbush, R., Kueng, R., Preskill, J., *et al.*: Quantum advantage in learning from experiments. *Science* **376**(6598), 1182–1186 (2022)

[54] Plevris, V., Solorzano, G.: A collection of 30 multidimensional functions for global optimization benchmarking. *Data* **7**(4), 46 (2022)

[55] Liang, J., Suganthan, P., Qu, B., Gong, D., Yue, C.: Problem definitions and evaluation criteria for the cec 2020 special session on multimodal multiobjective optimization (2019) <https://doi.org/10.13140/RG.2.2.31746.02247>

[56] Preskill, J.: Quantum computing in the nisq era and beyond. *Quantum* **2**, 79 (2018)

[57] Saravanan, V., Saeed, S.M.: Data-driven reliability models of quantum circuit: From traditional ml to graph neural network. *IEEE Transactions on Computer-Aided Design of Integrated Circuits and Systems* **42**(5), 1477–1489 (2022)

Table 2 Details of benchmark functions. The function types are categorized as follows: U = unimodal; M = multimodal; EM = extreme multimodal; D = differentiable; ND = non-differentiable; NS = nonseparable; NC = non-convex; NCt = non-continuous.

Function name	No.	Equation	Domain Interval	Type
Sphere function	1	$f(\mathbf{x}) = \sum_{i=1}^d x_i^2$	[-5, 5] ²	U, D
Ellipsoid	2	$f(\mathbf{x}) = \sum_{i=1}^d i \cdot x_i^2$	[-5, 5] ²	U, D
Bent Cigar	3	$f(\mathbf{x}) = x_1^2 + 10^6 \sum_{i=2}^d x_i^2$	[-5, 5] ²	U, NS
Discus	4	$f(\mathbf{x}) = 10^6 \cdot x_1^2 + \sum_{i=2}^d x_i^2$	[-5, 5] ²	U
Different Powers	5	$f(\mathbf{x}) = \sum_{i=1}^d x_i ^{i+1}$	[-5, 5] ²	U
Rosenbrock	6	$f(\mathbf{x}) = \sum_{i=1}^{d-1} \left(100 (x_{i+1} - x_i^2)^2 + (x_i + 1)^2 \right)$	[-5, 5] ²	M
Schaffer F7	7	$f(\mathbf{x}) = \left(\frac{1}{d-1} \sum_{i=1}^{d-1} \left(\sqrt{s_i} + \sqrt{s_i} \cdot \sin^2 \left(50 \cdot s_i^1/5 \right) \right) \right)^2$ where $s_i = \sqrt{x_i^2 + x_{i+1}^2}$	[-5, 5] ²	M, NS
Ackley	8	$f(\mathbf{x}) = -20 \cdot \exp \left(-0.2 \cdot \sqrt{\frac{1}{d} \cdot \sum_{i=1}^d x_i^2} \right) - \sqrt{\frac{1}{d} \sum_{i=1}^d \cos \left(2 \cdot \pi \cdot x_i \right)} + e + 20$	[-5, 5] ²	M, NC
Rastrigin	9	$f(\mathbf{x}) = \sum_{i=1}^d \left(x_i^2 - 10 \cdot \cos \left(2 \cdot \pi \cdot x_i \right) \right) + 10 \cdot d$	[-5, 5] ²	M
Weierstrass	10	$f(\mathbf{x}) = \sum_{i=1}^d \left(\sum_{k=0}^{k_{\max}} \left(a^k \cdot \cos \left(2 \cdot \pi \cdot b^k \cdot (x_i + 0.5) \right) \right) - d \cdot \sum_{k=0}^{k_{\max}} \left(a^k \cdot \cos \left(\pi \cdot b^k \right) \right) \right)$ where $a = 0.5, b = 3, k_{\max} = 20$	[-5, 5] ²	M, ND
Griewank	11	$f(\mathbf{x}) = \frac{1}{4000} \cdot \sum_{i=1}^d x_i^2 - \prod_{i=1}^d \cos \left(\frac{x_i}{\sqrt{i}} \right) + 1$	[-10, 10] ²	M
Schwefel	12	$f(\mathbf{x}) = - \sum_{i=1}^d x_i \cdot \sin \left(\sqrt{ x_i } \right) + 41.8 \cdot 9828872724337 \cdot d$	[-500, 500] ²	M
Katsuura	13	$f(\mathbf{x}) = \frac{10}{d^2} \cdot \prod_{i=1}^d \left(1 + i \cdot \sum_{j=1}^{32} \left 2^{j \cdot x_i - \frac{\lfloor 2^j \cdot x_i + \frac{1}{2} \rfloor}{2^j}} \right \right)^{\frac{10}{d^2}}$	[-500, 500] ²	EM
Griewank-Rosenbrock	14	$f(\mathbf{x}) = \sum_{i=1}^d \left[\frac{\left(100 (x_i^2 - x_{i+1})^2 + (x_i - 1)^2 \right)^2}{4000} - \cos \left(100 (x_i^2 - x_{i+1})^2 + (x_i - 1)^2 \right) + 1 \right]$	[-300, 300] ²	M
Expanded Schaffer 6	15	$f(\mathbf{x}) = \sum_{i=1}^{D-1} \left(g(x_i, x_{i+1}) \right) + g(x_D, x_1)$ where $g(x, y) = 0.5 + \frac{\sin^2 \left(\sqrt{x^2 + y^2} \right) - 0.5}{\left(1 + 0.001 \cdot (x^2 + y^2) \right)^2}$	[-10, 10] ²	M, NS
Step-Rastrigin	16	$f(\mathbf{x}) = \sum_{i=1}^D \left(z_i^2 - 10 \cos(2\pi z_i) + 10 \right)$ where $z_i \sim \tilde{z}_i = \begin{cases} \frac{512}{100} \cdot z_i + 0.5, & z_i > 0.5, \\ \frac{512}{100} \cdot z_i, & \text{otherwise} \end{cases}$	[-30, 30] ²	M, NCt, non-D
HappyCat	17	$f(\mathbf{x}) = \sum_{i=1}^d x_i^2 - d^{\lfloor 1/4 + \frac{0.5 \cdot \sum_{i=1}^d x_i^2 + \sum_{i=1}^d x_i}{d} + 0.5 \rfloor}$	[-50, 50] ²	M
HGBat	18	$f(\mathbf{x}) = \left(\sum_{i=1}^d x_i^2 \right)^2 - \left(\sum_{i=1}^d x_i \right)^2$ $1/2 + \frac{0.5 \cdot \sum_{i=1}^d x_i^2 + \sum_{i=1}^d x_i}{d} + 0.5$	[-30, 30] ²	M
Different Powers Modified	19	$f(\mathbf{x}) = \left(\sum_{i=1}^d z_i ^{2 + \frac{4(i-1)}{d-1}} \right)^{1/2}$	[-5, 5] ²	U, NS
Zakharov	20	$f(\mathbf{x}) = \sum_{i=1}^d x_i^2 + \left(\sum_{i=1}^d 0.5 \cdot i \cdot x_i \right)^2 + \left(\sum_{i=1}^d 0.5 \cdot i \cdot x_i \right)^4$	[-5, 5] ²	U
Lévy	21	$f(\mathbf{x}) = \sin^2(\pi w_1) + \sum_{i=1}^{d-1} (w_i - 1)^2 \left[\frac{1}{1 + 10 \sin^2(\pi w_i + 1)} \right] + (w_d - 1)^2 \left[1 + \sin^2(2\pi w_d) \right]$ where $w_i = 1 + \frac{x_i}{d}$, for $i = 1, \dots, d$	[-500, 500] ²	M
Dixon-Price	22	$f(\mathbf{x}) = (x_1 - 1)^2 + \sum_{i=2}^d i \cdot (2x_i)^2 - x_i - 1$	[-10 ³ , 10 ³] ²	U, NS

Table 3 Average model rankings (mean \pm standard deviation) computed from R^2 scores across the 22 benchmark regression functions. Lower ranks indicate better overall performance.

Rank	Model	Mean \pm Std	Rank	Model	Mean \pm Std	Rank	Model	Mean \pm Std
1	DT	2.50 \pm 1.25	22	RRQNN-60-1q	23.80 \pm 14.16	43	SimplifiedTwoDesign-3	39.70 \pm 6.17
2	RF	2.70 \pm 7.00	23	BasicEntanglerLayers-10	26.05 \pm 5.64	44	BasicEntanglerLayers-4	40.48 \pm 5.99
3	knn3	6.34 \pm 10.06	24	RRQNN-40-1q	26.18 \pm 14.68	45	BasicEntanglerLayers-3	41.34 \pm 5.42
4	knn4	6.59 \pm 10.30	25	SimplifiedTwoDesign-60	26.50 \pm 14.65	46	MLP100-100-ReLU	42.20 \pm 11.20
5	StronglyEntanglingLayers-40	7.41 \pm 4.13	26	SimplifiedTwoDesign-7	26.66 \pm 7.96	47	RRQNN-5-1q	43.73 \pm 5.98
6	StronglyEntanglingLayers-60	8.30 \pm 5.07	27	StronglyEntanglingLayers-6	27.11 \pm 7.08	48	StronglyEntanglingLayers-3	45.57 \pm 6.51
7	knn2	8.34 \pm 9.03	28	BasicEntanglerLayers-9	27.43 \pm 4.86	49	SimplifiedTwoDesign-2	47.14 \pm 6.79
8	StronglyEntanglingLayers-20	9.50 \pm 2.39	29	RRQNN-40-2q	27.48 \pm 11.90	50	SimplifiedTwoDesign-1	48.82 \pm 5.37
9	SimplifiedTwoDesign-20	13.30 \pm 10.43	30	SVR-RBF	29.27 \pm 15.59	51	BasicEntanglerLayers-1	48.82 \pm 5.37
10	RRQNN-120-2q	15.48 \pm 12.04	31	MLP500-500-ReLU	29.82 \pm 20.01	52	StronglyEntanglingLayers-2	48.82 \pm 5.37
11	StronglyEntanglingLayers-10	16.14 \pm 4.73	32	SimplifiedTwoDesign-6	30.11 \pm 6.57	53	BasicEntanglerLayers-2	50.36 \pm 4.97
12	RRQNN-120-1q	17.20 \pm 12.15	33	RRQNN-20-1q	30.25 \pm 11.29	54	MLP500-ReLU	50.80 \pm 6.53
13	BasicEntanglerLayers-20	18.59 \pm 6.09	34	StronglyEntanglingLayers-5	31.39 \pm 7.87	55	SVR-sigmoid	52.18 \pm 5.02
14	StronglyEntanglingLayers-9	18.66 \pm 5.34	35	BasicEntanglerLayers-7	31.57 \pm 5.47	56	SVR-poly	54.25 \pm 7.30
15	SimplifiedTwoDesign-10	19.09 \pm 8.38	36	RRQNN-20-2q	32.52 \pm 7.65	57	MLP100-ReLU	57.43 \pm 1.20
16	SimplifiedTwoDesign-40	20.02 \pm 12.71	37	SimplifiedTwoDesign-5	33.77 \pm 6.66	58	StronglyEntanglingLayers-1	57.77 \pm 2.33
17	BasicEntanglerLayers-40	20.27 \pm 7.51	38	BasicEntanglerLayers-6	33.89 \pm 5.77	59	MLP100-1d	60.34 \pm 1.52
18	BasicEntanglerLayers-60	21.27 \pm 11.10	39	BasicEntanglerLayers-5	36.52 \pm 5.35	60	MLP500-500-1d	60.36 \pm 1.91
19	SimplifiedTwoDesign-9	21.82 \pm 8.24	40	StronglyEntanglingLayers-4	38.20 \pm 8.14	61	MLP100-100-1d	60.36 \pm 1.78
20	StronglyEntanglingLayers-7	22.20 \pm 5.90	41	RRQNN-10-1q	38.23 \pm 7.75	62	SVR-linear	60.45 \pm 1.89
21	RRQNN-60-2q	23.52 \pm 13.78	42	SimplifiedTwoDesign-4	38.43 \pm 6.75	63	MLP500-1d	60.64 \pm 1.61

Dataset	Model	R^2 -score	RMSE
$f_1^1 D$	RRQNN-25 gates	0.999000	0.009191
$f_1^1 D$	RRQNN-20 gates	0.998200	0.012837
$f_1^1 D$	RRQNN-15 gates	0.997100	0.016551
$f_1^1 D$	RF	0.995987	0.018765
$f_1^1 D$	DT	0.994382	0.022859
$f_1^1 D$	RRQNN-10 gates	0.994000	0.022989
$f_1^1 D$	KNN2	0.993750	0.023861
$f_1^1 D$	KNN3	0.988465	0.031618
$f_1^1 D$	KNN4	0.975460	0.044343
$f_1^1 D$	SVR-RBF	0.891315	0.088069
$f_1^1 D$	MLP-100	-17.439350	0.247251
$f_1^1 D$	MLP-100-100	-29.740651	0.303552
$f_1^1 D$	SVR-poly	- inf	0.311554
$f_1^1 D$	SVR-linear	- inf	0.311554
$f_1^1 D$	SVR-sigmoid	- inf	0.311554
$f_2^1 D$	RRQNN-25 gates	0.999000	0.014948
$f_2^1 D$	RRQNN-20 gates	0.997600	0.018709
$f_2^1 D$	RF	0.996228	0.023329
$f_2^1 D$	RRQNN-15 gates	0.995900	0.024688
$f_2^1 D$	DT	0.995419	0.026495
$f_2^1 D$	KNN2	0.994620	0.028388
$f_2^1 D$	SVR-poly	0.987654	0.038940
$f_2^1 D$	KNN3	0.988519	0.040535
$f_2^1 D$	RRQNN-10 gates	0.988300	0.041865
$f_2^1 D$	KNN4	0.974486	0.058006
$f_2^1 D$	SVR-RBF	0.963202	0.073446
$f_2^1 D$	SVR-linear	0.786758	0.156695
$f_2^1 D$	MLP-100-100	0.362336	0.197533
$f_2^1 D$	MLP-100	-68.571361	0.415031
$f_2^1 D$	SVR-sigmoid	-0.363334	1.243425
$f_3^1 D$	RRQNN-25 gates	0.994500	0.040548
$f_3^1 D$	RRQNN-20 gates	0.991200	0.051167
$f_3^1 D$	RF	0.989437	0.054274
$f_3^1 D$	DT	0.988732	0.059593
$f_3^1 D$	KNN2	0.985748	0.065208
$f_3^1 D$	RRQNN-15 gates	0.985900	0.065547
$f_3^1 D$	KNN3	0.965270	0.097353
$f_3^1 D$	RRQNN-10 gates	0.963500	0.105216
$f_3^1 D$	KNN4	0.917439	0.138495
$f_3^1 D$	SVR-RBF	0.887239	0.146927
$f_3^1 D$	MLP-100-100	-1002.978816	0.547193
$f_3^1 D$	SVR-linear	- inf	0.610670
$f_3^1 D$	SVR-sigmoid	- inf	0.610670
$f_3^1 D$	SVR-poly	- inf	0.619152
$f_3^1 D$	MLP-100	-1053.885342	0.921896
$f_4^1 D$	RRQNN-25 gates	1.000000	0.006314
$f_4^1 D$	RF	0.999335	0.010354
$f_4^1 D$	RRQNN-20 gates	0.999500	0.011206
$f_4^1 D$	RRQNN-15 gates	0.998700	0.015041
$f_4^1 D$	DT	0.998413	0.016068
$f_4^1 D$	KNN3	0.998333	0.016362
$f_4^1 D$	KNN2	0.998263	0.016733
$f_4^1 D$	KNN4	0.997494	0.019913
$f_4^1 D$	RRQNN-10 gates	0.993100	0.033522
$f_4^1 D$	SVR-RBF	0.971586	0.059961
$f_4^1 D$	SVR-linear	0.822931	0.145442
$f_4^1 D$	SVR-poly	-0.072663	0.274805
$f_4^1 D$	MLP-100-100	-9.431680	0.313086
$f_4^1 D$	MLP-100	-29.102670	0.355271
$f_4^1 D$	SVR-sigmoid	-0.021996	1.114870

Table A1 Results of the Proof of Concept detailed in Section 6.4

Model	R^2 -score \pm std	RMSE \pm std	#Params \pm std
RF	0.9989 \pm 0.0001	0.0145 \pm 0.0145	205285.8 \pm 347.31
knn4	0.9974 \pm 0.0002	0.0221 \pm 0.0221	0.0 \pm 0.0
knn3	0.9973 \pm 0.0001	0.0227 \pm 0.0227	0.0 \pm 0.0
RRQNN-120-2q	0.9969 \pm 0.0006	0.0249 \pm 0.0249	84.4 \pm 3.34
DT	0.9969 \pm 0.0001	0.0245 \pm 0.0245	3245.0 \pm 9.29
StronglyEntanglingLayers-40	0.9963 \pm 0.0016	0.0262 \pm 0.0262	240.0 \pm 0.0
knn2	0.9963 \pm 0.0001	0.0266 \pm 0.0266	0.0 \pm 0.0
MLP500-500-ReLU	0.9955 \pm 0.0015	0.0288 \pm 0.0288	252501.0 \pm 0.0
StronglyEntanglingLayers-20	0.9951 \pm 0.0047	0.0287 \pm 0.0287	120.0 \pm 0.0
RRQNN-120-1q	0.9947 \pm 0.0019	0.032 \pm 0.032	81.3 \pm 3.33
RRQNN-60-2q	0.9946 \pm 0.0011	0.0322 \pm 0.0322	43.1 \pm 2.08
RRQNN-60-1q	0.9942 \pm 0.0017	0.0328 \pm 0.0328	40.5 \pm 2.59
SimplifiedTwoDesign-40	0.994 \pm 0.0034	0.0326 \pm 0.0326	82.0 \pm 0.0
StronglyEntanglingLayers-60	0.9939 \pm 0.0047	0.0324 \pm 0.0324	360.0 \pm 0.0
StronglyEntanglingLayers-10	0.9935 \pm 0.0016	0.0351 \pm 0.0351	60.0 \pm 0.0
RRQNN-40-1q	0.9927 \pm 0.0032	0.0365 \pm 0.0365	27.3 \pm 1.64
StronglyEntanglingLayers-9	0.9922 \pm 0.0022	0.0385 \pm 0.0385	54.0 \pm 0.0
RRQNN-40-2q	0.9921 \pm 0.0024	0.0384 \pm 0.0384	28.3 \pm 2.11
StronglyEntanglingLayers-7	0.9901 \pm 0.0027	0.0433 \pm 0.0433	42.0 \pm 0.0
BasicEntanglerLayers-20	0.9892 \pm 0.0046	0.0445 \pm 0.0445	40.0 \pm 0.0
SimplifiedTwoDesign-10	0.9885 \pm 0.0033	0.0465 \pm 0.0465	22.0 \pm 0.0
SimplifiedTwoDesign-20	0.9871 \pm 0.021	0.042 \pm 0.042	42.0 \pm 0.0
BasicEntanglerLayers-40	0.9822 \pm 0.0107	0.0562 \pm 0.0562	80.0 \pm 0.0
SimplifiedTwoDesign-7	0.9821 \pm 0.0068	0.0578 \pm 0.0578	16.0 \pm 0.0
RRQNN-20-1q	0.982 \pm 0.0072	0.058 \pm 0.058	13.6 \pm 0.52
RRQNN-20-2q	0.9807 \pm 0.0077	0.0601 \pm 0.0601	14.5 \pm 1.27
SimplifiedTwoDesign-9	0.9798 \pm 0.0153	0.0592 \pm 0.0592	20.0 \pm 0.0
StronglyEntanglingLayers-6	0.9759 \pm 0.0171	0.0646 \pm 0.0646	36.0 \pm 0.0
SVR-RBF	0.9754 \pm 0.0004	0.0652 \pm 0.0652	44.6 \pm 4.33
SimplifiedTwoDesign-6	0.9752 \pm 0.0157	0.067 \pm 0.067	14.0 \pm 0.0
BasicEntanglerLayers-9	0.9678 \pm 0.0277	0.0745 \pm 0.0745	18.0 \pm 0.0
BasicEntanglerLayers-10	0.9622 \pm 0.0239	0.082 \pm 0.082	20.0 \pm 0.0
StronglyEntanglingLayers-5	0.9616 \pm 0.0189	0.0832 \pm 0.0832	30.0 \pm 0.0
BasicEntanglerLayers-60	0.9607 \pm 0.0272	0.0833 \pm 0.0833	120.0 \pm 0.0
MLP100-100-ReLU	0.9578 \pm 0.0038	0.0829 \pm 0.0829	10501.0 \pm 0.0
SimplifiedTwoDesign-60	0.9573 \pm 0.0474	0.0791 \pm 0.0791	122.0 \pm 0.0
BasicEntanglerLayers-7	0.9542 \pm 0.0213	0.0918 \pm 0.0918	14.0 \pm 0.0
BasicEntanglerLayers-6	0.9452 \pm 0.0262	0.1004 \pm 0.1004	12.0 \pm 0.0
RRQNN-10-1q	0.9438 \pm 0.024	0.1011 \pm 0.1011	5.2 \pm 0.79
BasicEntanglerLayers-5	0.9176 \pm 0.0396	0.1228 \pm 0.1228	10.0 \pm 0.0
StronglyEntanglingLayers-4	0.9074 \pm 0.0011	0.1334 \pm 0.1334	24.0 \pm 0.0
SimplifiedTwoDesign-5	0.9012 \pm 0.0654	0.1312 \pm 0.1312	12.0 \pm 0.0
BasicEntanglerLayers-4	0.8919 \pm 0.0348	0.1429 \pm 0.1429	8.0 \pm 0.0
SimplifiedTwoDesign-4	0.8738 \pm 0.0395	0.1544 \pm 0.1544	10.0 \pm 0.0
RRQNN-5-1q	0.8432 \pm 0.0135	0.1736 \pm 0.1736	2.0 \pm 0.0
SimplifiedTwoDesign-3	0.82 \pm 0.1399	0.1774 \pm 0.1774	8.0 \pm 0.0
BasicEntanglerLayers-3	0.7953 \pm 0.0	0.1984 \pm 0.1984	6.0 \pm 0.0
StronglyEntanglingLayers-3	0.4835 \pm 0.0002	0.3152 \pm 0.3152	18.0 \pm 0.0
SimplifiedTwoDesign-2	0.3892 \pm 0.4106	0.3225 \pm 0.3225	6.0 \pm 0.0
MLP500-ReLU	0.3032 \pm 0.039	0.2242 \pm 0.2242	2001.0 \pm 0.0
MLP500-500-Id	-inf \pm inf	0.4411 \pm 0.4411	252501.0 \pm 0.0
MLP100-100-Id	-inf \pm inf	0.445 \pm 0.445	10501.0 \pm 0.0
MLP100-1d	-inf \pm inf	0.4395 \pm 0.4395	401.0 \pm 0.0
SVR-linear	-inf \pm inf	0.44 \pm 0.44	2.0 \pm 0.0
MLP500-1d	-inf \pm inf	0.441 \pm 0.441	2001.0 \pm 0.0
StronglyEntanglingLayers-1	-8.8688 \pm 0.0	1.3778 \pm 1.3778	6.0 \pm 0.0
MLP100-ReLU	-3.1089 \pm 0.1714	0.3538 \pm 0.3538	401.0 \pm 0.0
SVR-poly	-0.5553 \pm 0.0266	0.3768 \pm 0.3768	2599.2 \pm 23.71
SVR-sigmoid	-0.0589 \pm 0.0141	75.7616 \pm 75.7616	3344.8 \pm 2.7
BasicEntanglerLayers-2	-0.0002 \pm 0.0002	0.4386 \pm 0.4386	4.0 \pm 0.0
BasicEntanglerLayers-1	-0.0 \pm 0.0001	0.4386 \pm 0.4386	2.0 \pm 0.0
SimplifiedTwoDesign-1	-0.0 \pm 0.0001	0.4386 \pm 0.4386	4.0 \pm 0.0
StronglyEntanglingLayers-2	-0.0 \pm 0.0001	0.4386 \pm 0.4386	12.0 \pm 0.0

Table B2 Results of the benchmark Function 1

Model	R^2 -score \pm std	RMSE \pm std	#Params \pm std
RF	1.0 \pm 0.0	0.0 \pm 0.0	173309.0 \pm 1572.14
DT	1.0 \pm 0.0	0.0 \pm 0.0	2557.2 \pm 30.63
MLP500-500-ReLU	0.9974 \pm 0.0014	0.0306 \pm 0.0306	252501.0 \pm 0.0
knn4	0.9974 \pm 0.0002	0.031 \pm 0.031	0.0 \pm 0.0
knn3	0.9973 \pm 0.0002	0.0319 \pm 0.0319	0.0 \pm 0.0
SimplifiedTwoDesign-20	0.9972 \pm 0.0021	0.031 \pm 0.031	42.0 \pm 0.0
StronglyEntanglingLayers-60	0.9968 \pm 0.0014	0.0343 \pm 0.0343	360.0 \pm 0.0
knn2	0.9964 \pm 0.0002	0.0372 \pm 0.0372	0.0 \pm 0.0
StronglyEntanglingLayers-40	0.9962 \pm 0.0031	0.0363 \pm 0.0363	240.0 \pm 0.0
StronglyEntanglingLayers-20	0.996 \pm 0.0016	0.039 \pm 0.039	120.0 \pm 0.0
RRQNN-120-1q	0.9951 \pm 0.0009	0.0441 \pm 0.0441	79.2 \pm 4.24
RRQNN-40-1q	0.9938 \pm 0.0033	0.0474 \pm 0.0474	28.3 \pm 1.95
RRQNN-20-1q	0.9933 \pm 0.0033	0.0503 \pm 0.0503	13.4 \pm 0.7
RRQNN-120-2q	0.9933 \pm 0.0018	0.0503 \pm 0.0503	85.3 \pm 4.35
SimplifiedTwoDesign-10	0.9931 \pm 0.0025	0.0508 \pm 0.0508	22.0 \pm 0.0
RRQNN-60-1q	0.9923 \pm 0.0015	0.0539 \pm 0.0539	41.6 \pm 2.95
BasicEntanglerLayers-20	0.9916 \pm 0.004	0.0552 \pm 0.0552	40.0 \pm 0.0
RRQNN-60-2q	0.9913 \pm 0.002	0.058 \pm 0.058	42.8 \pm 2.49
SimplifiedTwoDesign-9	0.9912 \pm 0.0042	0.0568 \pm 0.0568	20.0 \pm 0.0
SVR-RBF	0.991 \pm 0.0001	0.06 \pm 0.06	97.4 \pm 5.97
StronglyEntanglingLayers-10	0.9909 \pm 0.0024	0.0588 \pm 0.0588	60.0 \pm 0.0
BasicEntanglerLayers-40	0.99 \pm 0.0054	0.0601 \pm 0.0601	80.0 \pm 0.0
SimplifiedTwoDesign-40	0.9895 \pm 0.016	0.0529 \pm 0.0529	82.0 \pm 0.0
StronglyEntanglingLayers-9	0.9895 \pm 0.0026	0.0632 \pm 0.0632	54.0 \pm 0.0
RRQNN-40-2q	0.9892 \pm 0.0027	0.0637 \pm 0.0637	27.5 \pm 2.51
StronglyEntanglingLayers-7	0.987 \pm 0.0101	0.0668 \pm 0.0668	42.0 \pm 0.0
BasicEntanglerLayers-60	0.9857 \pm 0.0099	0.0715 \pm 0.0715	120.0 \pm 0.0
SimplifiedTwoDesign-7	0.985 \pm 0.0061	0.0747 \pm 0.0747	16.0 \pm 0.0
BasicEntanglerLayers-10	0.984 \pm 0.0072	0.0766 \pm 0.0766	20.0 \pm 0.0
BasicEntanglerLayers-9	0.983 \pm 0.0049	0.0799 \pm 0.0799	18.0 \pm 0.0
SimplifiedTwoDesign-60	0.9821 \pm 0.0189	0.0764 \pm 0.0764	122.0 \pm 0.0
RRQNN-20-2q	0.9714 \pm 0.0179	0.101 \pm 0.101	12.9 \pm 1.45
SimplifiedTwoDesign-6	0.9706 \pm 0.0263	0.1012 \pm 0.1012	14.0 \pm 0.0
SimplifiedTwoDesign-5	0.9699 \pm 0.026	0.1026 \pm 0.1026	12.0 \pm 0.0
MLP100-100-ReLU	0.9697 \pm 0.0046	0.1015 \pm 0.1015	10501.0 \pm 0.0
BasicEntanglerLayers-6	0.9681 \pm 0.0158	0.1083 \pm 0.1083	12.0 \pm 0.0
BasicEntanglerLayers-7	0.9623 \pm 0.0298	0.1139 \pm 0.1139	14.0 \pm 0.0
StronglyEntanglingLayers-6	0.9604 \pm 0.0177	0.1211 \pm 0.1211	36.0 \pm 0.0
StronglyEntanglingLayers-5	0.9497 \pm 0.0208	0.1367 \pm 0.1367	30.0 \pm 0.0
RRQNN-10-1q	0.9482 \pm 0.0236	0.138 \pm 0.138	5.6 \pm 0.84
BasicEntanglerLayers-5	0.911 \pm 0.0292	0.1816 \pm 0.1816	10.0 \pm 0.0
BasicEntanglerLayers-3	0.8959 \pm 0.0	0.2001 \pm 0.2001	6.0 \pm 0.0
SimplifiedTwoDesign-4	0.8959 \pm 0.0	0.2001 \pm 0.2001	10.0 \pm 0.0
SimplifiedTwoDesign-3	0.8959 \pm 0.0	0.2001 \pm 0.2001	8.0 \pm 0.0
BasicEntanglerLayers-4	0.8916 \pm 0.0096	0.2041 \pm 0.2041	8.0 \pm 0.0
StronglyEntanglingLayers-4	0.6656 \pm 0.0002	0.3587 \pm 0.3587	24.0 \pm 0.0
RRQNN-5-1q	0.576 \pm 0.2376	0.392 \pm 0.392	1.4 \pm 0.84
MLP500-ReLU	0.4996 \pm 0.0259	0.2951 \pm 0.2951	2001.0 \pm 0.0
SimplifiedTwoDesign-2	0.2723 \pm 0.1882	0.5254 \pm 0.5254	6.0 \pm 0.0
SVR-linear	-inf \pm inf	0.6438 \pm 0.6438	2.0 \pm 0.0
MLP100-Id	-inf \pm inf	0.621 \pm 0.621	401.0 \pm 0.0
MLP100-100-Id	-inf \pm inf	0.625 \pm 0.625	10501.0 \pm 0.0
MLP500-500-1d	-inf \pm inf	0.6245 \pm 0.6245	252501.0 \pm 0.0
MLP500-Id	-inf \pm inf	0.6221 \pm 0.6221	2001.0 \pm 0.0
StronglyEntanglingLayers-1	-4.4344 \pm 0.0	1.4459 \pm 1.4459	6.0 \pm 0.0
MLP100-ReLU	-2.8617 \pm 0.0834	0.4685 \pm 0.4685	401.0 \pm 0.0
SVR-poly	-0.3101 \pm 0.0168	0.5238 \pm 0.5238	2677.6 \pm 24.11
SVR-sigmoid	-0.0633 \pm 0.0152	75.9174 \pm 75.9174	3347.0 \pm 1.7
BasicEntanglerLayers-2	-0.0246 \pm 0.0769	0.6275 \pm 0.6275	4.0 \pm 0.0
StronglyEntanglingLayers-3	-0.0004 \pm 0.0004	0.6204 \pm 0.6204	18.0 \pm 0.0
StronglyEntanglingLayers-2	-0.0002 \pm 0.0002	0.6203 \pm 0.6203	12.0 \pm 0.0
SimplifiedTwoDesign-1	-0.0002 \pm 0.0002	0.6203 \pm 0.6203	4.0 \pm 0.0
BasicEntanglerLayers-1	-0.0002 \pm 0.0002	0.6203 \pm 0.6203	2.0 \pm 0.0

Table B3 Results of the benchmark Function 2

Model	R^2 -score \pm std	RMSE \pm std	#Params \pm std
RF	1.0 \pm 0.0	0.0 \pm 0.0	173309.0 \pm 1572.14
DT	1.0 \pm 0.0	0.0 \pm 0.0	2557.2 \pm 30.63
SimplifiedTwoDesign-20	0.9977 \pm 0.001	0.0296 \pm 0.0296	42.0 \pm 0.0
MLP500-500-ReLU	0.9974 \pm 0.0014	0.0306 \pm 0.0306	252501.0 \pm 0.0
knn4	0.9974 \pm 0.0002	0.031 \pm 0.031	0.0 \pm 0.0
knn3	0.9973 \pm 0.0002	0.0319 \pm 0.0319	0.0 \pm 0.0
knn2	0.9964 \pm 0.0002	0.0372 \pm 0.0372	0.0 \pm 0.0
StronglyEntanglingLayers-40	0.9961 \pm 0.0024	0.0374 \pm 0.0374	240.0 \pm 0.0
StronglyEntanglingLayers-20	0.996 \pm 0.0004	0.0392 \pm 0.0392	120.0 \pm 0.0
StronglyEntanglingLayers-60	0.9958 \pm 0.0021	0.039 \pm 0.039	360.0 \pm 0.0
RRQNN-40-1q	0.9945 \pm 0.0013	0.0453 \pm 0.0453	28.4 \pm 2.22
RRQNN-120-1q	0.9942 \pm 0.0013	0.0467 \pm 0.0467	79.7 \pm 4.3
RRQNN-20-1q	0.9941 \pm 0.0007	0.0478 \pm 0.0478	13.1 \pm 1.1
RRQNN-120-2q	0.994 \pm 0.0011	0.0478 \pm 0.0478	84.8 \pm 3.29
RRQNN-60-1q	0.9935 \pm 0.0014	0.0499 \pm 0.0499	44.6 \pm 2.32
StronglyEntanglingLayers-10	0.9927 \pm 0.0036	0.0512 \pm 0.0512	60.0 \pm 0.0
SimplifiedTwoDesign-10	0.9922 \pm 0.0037	0.0533 \pm 0.0533	22.0 \pm 0.0
SimplifiedTwoDesign-9	0.9912 \pm 0.0034	0.0572 \pm 0.0572	20.0 \pm 0.0
SVR-RBF	0.991 \pm 0.0001	0.06 \pm 0.06	97.4 \pm 5.97
SimplifiedTwoDesign-40	0.9908 \pm 0.0096	0.0532 \pm 0.0532	82.0 \pm 0.0
RRQNN-60-2q	0.9903 \pm 0.0023	0.0605 \pm 0.0605	43.2 \pm 1.69
BasicEntanglerLayers-20	0.99 \pm 0.0076	0.0584 \pm 0.0584	40.0 \pm 0.0
StronglyEntanglingLayers-9	0.9889 \pm 0.0042	0.0642 \pm 0.0642	54.0 \pm 0.0
BasicEntanglerLayers-40	0.9883 \pm 0.0072	0.0647 \pm 0.0647	80.0 \pm 0.0
RRQNN-40-2q	0.9878 \pm 0.0066	0.067 \pm 0.067	29.1 \pm 1.97
BasicEntanglerLayers-10	0.9877 \pm 0.0059	0.067 \pm 0.067	20.0 \pm 0.0
BasicEntanglerLayers-9	0.9869 \pm 0.0056	0.0698 \pm 0.0698	18.0 \pm 0.0
BasicEntanglerLayers-60	0.9843 \pm 0.011	0.0747 \pm 0.0747	120.0 \pm 0.0
SimplifiedTwoDesign-7	0.9837 \pm 0.0058	0.078 \pm 0.078	16.0 \pm 0.0
StronglyEntanglingLayers-7	0.9819 \pm 0.0097	0.0808 \pm 0.0808	42.0 \pm 0.0
RRQNN-20-2q	0.9784 \pm 0.0103	0.0884 \pm 0.0884	13.3 \pm 1.06
SimplifiedTwoDesign-60	0.9764 \pm 0.0223	0.0868 \pm 0.0868	122.0 \pm 0.0
BasicEntanglerLayers-7	0.9718 \pm 0.0242	0.0989 \pm 0.0989	14.0 \pm 0.0
MLP100-100-ReLU	0.9697 \pm 0.0046	0.1015 \pm 0.1015	10501.0 \pm 0.0
SimplifiedTwoDesign-6	0.9634 \pm 0.0355	0.1098 \pm 0.1098	14.0 \pm 0.0
StronglyEntanglingLayers-6	0.9621 \pm 0.0144	0.1189 \pm 0.1189	36.0 \pm 0.0
SimplifiedTwoDesign-5	0.9617 \pm 0.0347	0.1134 \pm 0.1134	12.0 \pm 0.0
BasicEntanglerLayers-6	0.9609 \pm 0.0337	0.1152 \pm 0.1152	12.0 \pm 0.0
RRQNN-10-1q	0.9468 \pm 0.0224	0.1398 \pm 0.1398	5.6 \pm 0.7
BasicEntanglerLayers-5	0.9338 \pm 0.0403	0.1515 \pm 0.1515	10.0 \pm 0.0
StronglyEntanglingLayers-5	0.9331 \pm 0.0203	0.1584 \pm 0.1584	30.0 \pm 0.0
SimplifiedTwoDesign-4	0.8959 \pm 0.0001	0.2002 \pm 0.2002	10.0 \pm 0.0
SimplifiedTwoDesign-3	0.8959 \pm 0.0	0.2001 \pm 0.2001	8.0 \pm 0.0
BasicEntanglerLayers-3	0.8959 \pm 0.0	0.2001 \pm 0.2001	6.0 \pm 0.0
BasicEntanglerLayers-4	0.8954 \pm 0.0014	0.2006 \pm 0.2006	8.0 \pm 0.0
StronglyEntanglingLayers-4	0.6656 \pm 0.0001	0.3587 \pm 0.3587	24.0 \pm 0.0
RRQNN-5-1q	0.6514 \pm 0.1236	0.361 \pm 0.361	1.2 \pm 0.63
MLP500-ReLU	0.4996 \pm 0.0259	0.2951 \pm 0.2951	2001.0 \pm 0.0
SimplifiedTwoDesign-2	0.2722 \pm 0.1884	0.5254 \pm 0.5254	6.0 \pm 0.0
MLP500-500-Id	-inf \pm inf	0.6245 \pm 0.6245	252501.0 \pm 0.0
MLP100-100-Id	-inf \pm inf	0.625 \pm 0.625	10501.0 \pm 0.0
MLP100-Id	-inf \pm inf	0.621 \pm 0.621	401.0 \pm 0.0
SVR-linear	-inf \pm inf	0.6438 \pm 0.6438	2.0 \pm 0.0
MLP500-Id	-inf \pm inf	0.6221 \pm 0.6221	2001.0 \pm 0.0
StronglyEntanglingLayers-1	-4.4344 \pm 0.0	1.4459 \pm 1.4459	6.0 \pm 0.0
MLP100-ReLU	-2.8617 \pm 0.0834	0.4685 \pm 0.4685	401.0 \pm 0.0
SVR-poly	-0.3101 \pm 0.0168	0.5238 \pm 0.5238	2677.6 \pm 24.11
SVR-sigmoid	-0.0633 \pm 0.0152	75.9174 \pm 75.9174	3347.0 \pm 1.7
StronglyEntanglingLayers-3	-0.0005 \pm 0.0004	0.6204 \pm 0.6204	18.0 \pm 0.0
BasicEntanglerLayers-2	-0.0003 \pm 0.0003	0.6204 \pm 0.6204	4.0 \pm 0.0
BasicEntanglerLayers-1	-0.0002 \pm 0.0002	0.6203 \pm 0.6203	2.0 \pm 0.0
SimplifiedTwoDesign-1	-0.0002 \pm 0.0002	0.6203 \pm 0.6203	4.0 \pm 0.0
StronglyEntanglingLayers-2	-0.0002 \pm 0.0002	0.6203 \pm 0.6203	12.0 \pm 0.0

Table B4 Results of the benchmark Function 3

Model	R^2 -score \pm std	RMSE \pm std	#Params \pm std
RF	1.0 \pm 0.0	0.0 \pm 0.0	173545.8 \pm 1210.53
DT	1.0 \pm 0.0	0.0 \pm 0.0	2562.4 \pm 22.84
MLP500-500-ReLU	0.9976 \pm 0.0012	0.0297 \pm 0.0297	252501.0 \pm 0.0
knn4	0.9975 \pm 0.0001	0.0307 \pm 0.0307	0.0 \pm 0.0
knn3	0.9973 \pm 0.0001	0.0318 \pm 0.0318	0.0 \pm 0.0
SimplifiedTwoDesign-20	0.9967 \pm 0.0043	0.0319 \pm 0.0319	42.0 \pm 0.0
StronglyEntanglingLayers-40	0.9966 \pm 0.0015	0.0354 \pm 0.0354	240.0 \pm 0.0
knn2	0.9963 \pm 0.0001	0.0378 \pm 0.0378	0.0 \pm 0.0
StronglyEntanglingLayers-60	0.9959 \pm 0.0015	0.0391 \pm 0.0391	360.0 \pm 0.0
StronglyEntanglingLayers-20	0.9958 \pm 0.001	0.04 \pm 0.04	120.0 \pm 0.0
RRQNN-120-1q	0.9955 \pm 0.0007	0.0416 \pm 0.0416	80.1 \pm 4.93
RRQNN-120-2q	0.994 \pm 0.0012	0.0476 \pm 0.0476	83.1 \pm 4.33
SimplifiedTwoDesign-10	0.993 \pm 0.0031	0.0506 \pm 0.0506	22.0 \pm 0.0
RRQNN-40-1q	0.9929 \pm 0.004	0.0509 \pm 0.0509	29.0 \pm 2.0
RRQNN-60-1q	0.9925 \pm 0.0016	0.0528 \pm 0.0528	41.4 \pm 2.32
BasicEntanglerLayers-20	0.9918 \pm 0.0053	0.0543 \pm 0.0543	40.0 \pm 0.0
SVR-RBF	0.991 \pm 0.0001	0.0598 \pm 0.0598	96.8 \pm 6.48
SimplifiedTwoDesign-40	0.9909 \pm 0.0139	0.0499 \pm 0.0499	82.0 \pm 0.0
RRQNN-60-2q	0.9909 \pm 0.0017	0.059 \pm 0.059	43.4 \pm 2.55
StronglyEntanglingLayers-10	0.9908 \pm 0.002	0.0593 \pm 0.0593	60.0 \pm 0.0
SimplifiedTwoDesign-9	0.9906 \pm 0.0027	0.0597 \pm 0.0597	20.0 \pm 0.0
RRQNN-20-1q	0.9902 \pm 0.0145	0.0549 \pm 0.0549	14.6 \pm 0.7
RRQNN-40-2q	0.989 \pm 0.0063	0.0631 \pm 0.0631	28.5 \pm 1.58
StronglyEntanglingLayers-9	0.9888 \pm 0.0039	0.0649 \pm 0.0649	54.0 \pm 0.0
BasicEntanglerLayers-40	0.9886 \pm 0.0083	0.063 \pm 0.063	80.0 \pm 0.0
BasicEntanglerLayers-60	0.9862 \pm 0.006	0.0712 \pm 0.0712	120.0 \pm 0.0
StronglyEntanglingLayers-7	0.9827 \pm 0.0054	0.0807 \pm 0.0807	42.0 \pm 0.0
RRQNN-20-2q	0.9823 \pm 0.0134	0.0776 \pm 0.0776	13.5 \pm 0.85
BasicEntanglerLayers-9	0.982 \pm 0.0112	0.08 \pm 0.08	18.0 \pm 0.0
SimplifiedTwoDesign-7	0.9818 \pm 0.0045	0.0831 \pm 0.0831	16.0 \pm 0.0
StronglyEntanglingLayers-6	0.9813 \pm 0.018	0.0785 \pm 0.0785	36.0 \pm 0.0
BasicEntanglerLayers-10	0.9802 \pm 0.0133	0.0829 \pm 0.0829	20.0 \pm 0.0
RRQNN-10-1q	0.9747 \pm 0.0206	0.0908 \pm 0.0908	5.1 \pm 0.57
SimplifiedTwoDesign-6	0.9731 \pm 0.0219	0.0974 \pm 0.0974	14.0 \pm 0.0
SimplifiedTwoDesign-60	0.9694 \pm 0.0274	0.097 \pm 0.097	122.0 \pm 0.0
MLP100-100-ReLU	0.9653 \pm 0.0055	0.1072 \pm 0.1072	10501.0 \pm 0.0
BasicEntanglerLayers-7	0.9582 \pm 0.0226	0.1224 \pm 0.1224	14.0 \pm 0.0
BasicEntanglerLayers-5	0.9582 \pm 0.0166	0.1239 \pm 0.1239	10.0 \pm 0.0
BasicEntanglerLayers-6	0.9578 \pm 0.0245	0.1219 \pm 0.1219	12.0 \pm 0.0
BasicEntanglerLayers-4	0.9473 \pm 0.0	0.1424 \pm 0.1424	8.0 \pm 0.0
StronglyEntanglingLayers-5	0.9343 \pm 0.0121	0.1584 \pm 0.1584	30.0 \pm 0.0
SimplifiedTwoDesign-5	0.9288 \pm 0.0426	0.1566 \pm 0.1566	12.0 \pm 0.0
SimplifiedTwoDesign-4	0.8959 \pm 0.0	0.2001 \pm 0.2001	10.0 \pm 0.0
SimplifiedTwoDesign-3	0.8959 \pm 0.0	0.2001 \pm 0.2001	8.0 \pm 0.0
StronglyEntanglingLayers-4	0.8464 \pm 0.0061	0.2431 \pm 0.2431	24.0 \pm 0.0
RRQNN-5-1q	0.767 \pm 0.0	0.2993 \pm 0.2993	2.0 \pm 0.0
BasicEntanglerLayers-3	0.6657 \pm 0.0001	0.3586 \pm 0.3586	6.0 \pm 0.0
StronglyEntanglingLayers-3	0.6657 \pm 0.0001	0.3586 \pm 0.3586	18.0 \pm 0.0
MLP500-ReLU	0.5213 \pm 0.0281	0.2917 \pm 0.2917	2001.0 \pm 0.0
SimplifiedTwoDesign-2	0.2723 \pm 0.1884	0.5254 \pm 0.5254	6.0 \pm 0.0
MLP500-500-1d	-inf \pm inf	0.6253 \pm 0.6253	252501.0 \pm 0.0
SVR-linear	-inf \pm inf	0.6433 \pm 0.6433	2.0 \pm 0.0
MLP100-1d	-inf \pm inf	0.6211 \pm 0.6211	401.0 \pm 0.0
MLP100-100-1d	-inf \pm inf	0.6242 \pm 0.6242	10501.0 \pm 0.0
MLP500-1d	-inf \pm inf	0.6248 \pm 0.6248	2001.0 \pm 0.0
MLP100-ReLU	-5.2158 \pm 0.282	0.5134 \pm 0.5134	401.0 \pm 0.0
StronglyEntanglingLayers-1	-4.4344 \pm 0.0	1.4459 \pm 1.4459	6.0 \pm 0.0
SVR-poly	-0.3031 \pm 0.0265	0.5231 \pm 0.5231	2685.0 \pm 27.23
SVR-sigmoid	-0.0646 \pm 0.014	75.9479 \pm 75.9479	3346.6 \pm 3.13
BasicEntanglerLayers-2	-0.0004 \pm 0.0005	0.6204 \pm 0.6204	4.0 \pm 0.0
StronglyEntanglingLayers-2	-0.0002 \pm 0.0003	0.6203 \pm 0.6203	12.0 \pm 0.0
SimplifiedTwoDesign-1	-0.0002 \pm 0.0003	0.6203 \pm 0.6203	4.0 \pm 0.0
BasicEntanglerLayers-1	-0.0002 \pm 0.0003	0.6203 \pm 0.6203	2.0 \pm 0.0

Table B5 Results of the benchmark Function 4

Model	R^2 -score \pm std	RMSE \pm std	#Params \pm std
RF	1.0 \pm 0.0	0.0007 \pm 0.0007	206018.8 \pm 296.56
DT	1.0 \pm 0.0	0.0008 \pm 0.0008	3249.6 \pm 7.89
StronglyEntanglingLayers-40	0.9962 \pm 0.0007	0.0361 \pm 0.0361	240.0 \pm 0.0
StronglyEntanglingLayers-60	0.996 \pm 0.0015	0.0369 \pm 0.0369	360.0 \pm 0.0
knn3	0.9956 \pm 0.0003	0.0387 \pm 0.0387	0.0 \pm 0.0
knn4	0.9955 \pm 0.0004	0.039 \pm 0.039	0.0 \pm 0.0
SimplifiedTwoDesign-20	0.9951 \pm 0.0021	0.0406 \pm 0.0406	42.0 \pm 0.0
knn2	0.9944 \pm 0.0003	0.0439 \pm 0.0439	0.0 \pm 0.0
StronglyEntanglingLayers-20	0.994 \pm 0.0008	0.0456 \pm 0.0456	120.0 \pm 0.0
RRQNN-120-1q	0.9921 \pm 0.0018	0.0526 \pm 0.0526	77.9 \pm 6.28
RRQNN-120-2q	0.9898 \pm 0.0012	0.0596 \pm 0.0596	82.1 \pm 5.32
RRQNN-60-1q	0.9892 \pm 0.0028	0.0609 \pm 0.0609	40.6 \pm 2.63
SVR-RBF	0.989 \pm 0.0002	0.0644 \pm 0.0644	162.0 \pm 5.73
RRQNN-40-1q	0.9887 \pm 0.0025	0.063 \pm 0.063	26.7 \pm 1.83
BasicEntanglerLayers-60	0.987 \pm 0.0034	0.0668 \pm 0.0668	120.0 \pm 0.0
BasicEntanglerLayers-40	0.9869 \pm 0.0055	0.0664 \pm 0.0664	80.0 \pm 0.0
BasicEntanglerLayers-20	0.9868 \pm 0.0068	0.066 \pm 0.066	40.0 \pm 0.0
SimplifiedTwoDesign-40	0.9853 \pm 0.0187	0.0614 \pm 0.0614	82.0 \pm 0.0
StronglyEntanglingLayers-10	0.9851 \pm 0.0049	0.0714 \pm 0.0714	60.0 \pm 0.0
RRQNN-60-2q	0.985 \pm 0.0028	0.0723 \pm 0.0723	41.4 \pm 3.03
SimplifiedTwoDesign-10	0.9831 \pm 0.0047	0.0762 \pm 0.0762	22.0 \pm 0.0
MLP500-500-ReLU	0.9831 \pm 0.0039	0.0743 \pm 0.0743	252501.0 \pm 0.0
StronglyEntanglingLayers-9	0.9814 \pm 0.005	0.0801 \pm 0.0801	54.0 \pm 0.0
SimplifiedTwoDesign-9	0.98 \pm 0.0053	0.0831 \pm 0.0831	20.0 \pm 0.0
RRQNN-20-1q	0.9781 \pm 0.006	0.0869 \pm 0.0869	12.5 \pm 1.35
RRQNN-40-2q	0.9771 \pm 0.0064	0.089 \pm 0.089	27.2 \pm 1.03
BasicEntanglerLayers-9	0.9702 \pm 0.0097	0.1011 \pm 0.1011	18.0 \pm 0.0
SimplifiedTwoDesign-60	0.97 \pm 0.0289	0.0894 \pm 0.0894	122.0 \pm 0.0
SimplifiedTwoDesign-7	0.967 \pm 0.0138	0.1054 \pm 0.1054	16.0 \pm 0.0
StronglyEntanglingLayers-7	0.9659 \pm 0.0143	0.1071 \pm 0.1071	42.0 \pm 0.0
BasicEntanglerLayers-10	0.9582 \pm 0.025	0.1168 \pm 0.1168	20.0 \pm 0.0
RRQNN-20-2q	0.9433 \pm 0.0281	0.1373 \pm 0.1373	13.4 \pm 1.35
BasicEntanglerLayers-7	0.9329 \pm 0.0485	0.1455 \pm 0.1455	14.0 \pm 0.0
BasicEntanglerLayers-6	0.931 \pm 0.0342	0.1521 \pm 0.1521	12.0 \pm 0.0
SimplifiedTwoDesign-6	0.9308 \pm 0.0617	0.1478 \pm 0.1478	14.0 \pm 0.0
StronglyEntanglingLayers-6	0.9141 \pm 0.0198	0.1723 \pm 0.1723	36.0 \pm 0.0
SimplifiedTwoDesign-5	0.889 \pm 0.0974	0.1822 \pm 0.1822	12.0 \pm 0.0
MLP100-100-ReLU	0.8879 \pm 0.0068	0.1761 \pm 0.1761	10501.0 \pm 0.0
BasicEntanglerLayers-5	0.8784 \pm 0.0918	0.1931 \pm 0.1931	10.0 \pm 0.0
RRQNN-10-1q	0.8511 \pm 0.0221	0.2277 \pm 0.2277	5.6 \pm 0.7
StronglyEntanglingLayers-5	0.8435 \pm 0.0258	0.2334 \pm 0.2334	30.0 \pm 0.0
SimplifiedTwoDesign-3	0.7481 \pm 0.0001	0.297 \pm 0.297	8.0 \pm 0.0
BasicEntanglerLayers-3	0.7481 \pm 0.0001	0.297 \pm 0.297	6.0 \pm 0.0
BasicEntanglerLayers-4	0.7475 \pm 0.0016	0.2973 \pm 0.2973	8.0 \pm 0.0
StronglyEntanglingLayers-4	0.7121 \pm 0.0005	0.3175 \pm 0.3175	24.0 \pm 0.0
SimplifiedTwoDesign-4	0.6902 \pm 0.1251	0.3245 \pm 0.3245	10.0 \pm 0.0
RRQNN-5-1q	0.6826 \pm 0.0234	0.3331 \pm 0.3331	2.8 \pm 0.42
SimplifiedTwoDesign-2	0.3571 \pm 0.1257	0.4728 \pm 0.4728	6.0 \pm 0.0
MLP500-ReLU	0.2274 \pm 0.0285	0.3261 \pm 0.3261	2001.0 \pm 0.0
MLP500-500-Id	-inf \pm inf	0.596 \pm 0.596	252501.0 \pm 0.0
SVR-linear	-inf \pm inf	0.6449 \pm 0.6449	2.0 \pm 0.0
MLP100-100-Id	-inf \pm inf	0.5974 \pm 0.5974	10501.0 \pm 0.0
MLP500-1d	-inf \pm inf	0.5935 \pm 0.5935	2001.0 \pm 0.0
MLP100-1d	-inf \pm inf	0.5942 \pm 0.5942	401.0 \pm 0.0
StronglyEntanglingLayers-1	-6.0673 \pm 0.0	1.573 \pm 1.573	6.0 \pm 0.0
MLP100-ReLU	-3.6082 \pm 0.1288	0.4719 \pm 0.4719	401.0 \pm 0.0
SVR-poly	-0.6353 \pm 0.0465	0.4942 \pm 0.4942	2353.4 \pm 22.17
BasicEntanglerLayers-2	-0.0601 \pm 0.1889	0.6074 \pm 0.6074	4.0 \pm 0.0
SVR-sigmoid	-0.0593 \pm 0.0139	75.7782 \pm 75.7782	3347.0 \pm 1.7
StronglyEntanglingLayers-3	-0.0003 \pm 0.0004	0.5918 \pm 0.5918	18.0 \pm 0.0
StronglyEntanglingLayers-2	-0.0002 \pm 0.0002	0.5917 \pm 0.5917	12.0 \pm 0.0
BasicEntanglerLayers-1	-0.0002 \pm 0.0002	0.5917 \pm 0.5917	2.0 \pm 0.0
SimplifiedTwoDesign-1	-0.0002 \pm 0.0002	0.5917 \pm 0.5917	4.0 \pm 0.0

Table B6 Results of the benchmark Function 5

Model	R^2 -score \pm std	RMSE \pm std	#Params \pm std
RF	0.9992 \pm 0.0001	0.0108 \pm 0.0108	211158.0 \pm 6.53
knn4	0.9983 \pm 0.0001	0.016 \pm 0.016	0.0 \pm 0.0
knn3	0.9982 \pm 0.0001	0.0166 \pm 0.0166	0.0 \pm 0.0
DT	0.9977 \pm 0.0001	0.0188 \pm 0.0188	3349.0 \pm 0.0
knn2	0.9975 \pm 0.0001	0.0197 \pm 0.0197	0.0 \pm 0.0
RRQNN-120-2q	0.9971 \pm 0.0007	0.0211 \pm 0.0211	86.9 \pm 4.28
StronglyEntanglingLayers-40	0.9968 \pm 0.0021	0.0214 \pm 0.0214	240.0 \pm 0.0
StronglyEntanglingLayers-60	0.9967 \pm 0.0017	0.0221 \pm 0.0221	360.0 \pm 0.0
StronglyEntanglingLayers-20	0.9966 \pm 0.001	0.0228 \pm 0.0228	120.0 \pm 0.0
MLP500-500-ReLU	0.9962 \pm 0.0007	0.0233 \pm 0.0239	252501.0 \pm 0.0
RRQNN-60-2q	0.9958 \pm 0.0015	0.0257 \pm 0.0257	43.9 \pm 2.42
RRQNN-60-1q	0.9953 \pm 0.0019	0.0266 \pm 0.0266	41.7 \pm 3.59
RRQNN-120-1q	0.9953 \pm 0.0018	0.0271 \pm 0.0271	80.5 \pm 4.45
RRQNN-40-1q	0.9951 \pm 0.0032	0.0263 \pm 0.0263	30.0 \pm 2.4
RRQNN-40-2q	0.9943 \pm 0.0048	0.0288 \pm 0.0288	30.0 \pm 2.11
RRQNN-20-1q	0.994 \pm 0.0027	0.0302 \pm 0.0302	13.4 \pm 1.17
StronglyEntanglingLayers-10	0.9919 \pm 0.0041	0.0345 \pm 0.0345	60.0 \pm 0.0
StronglyEntanglingLayers-9	0.9914 \pm 0.0034	0.0357 \pm 0.0357	54.0 \pm 0.0
StronglyEntanglingLayers-7	0.9856 \pm 0.0055	0.0465 \pm 0.0465	42.0 \pm 0.0
RRQNN-20-2q	0.9855 \pm 0.0096	0.0461 \pm 0.0461	13.9 \pm 1.2
RRQNN-10-1q	0.9843 \pm 0.0045	0.049 \pm 0.049	6.4 \pm 0.84
StronglyEntanglingLayers-6	0.9816 \pm 0.008	0.0523 \pm 0.0523	36.0 \pm 0.0
StronglyEntanglingLayers-5	0.9758 \pm 0.0125	0.0596 \pm 0.0596	30.0 \pm 0.0
MLP100-100-ReLU	0.9739 \pm 0.0015	0.0615 \pm 0.0615	10501.0 \pm 0.0
StronglyEntanglingLayers-4	0.9734 \pm 0.0136	0.0623 \pm 0.0623	24.0 \pm 0.0
SVR-RBF	0.9699 \pm 0.0008	0.0653 \pm 0.0653	39.4 \pm 2.5
RRQNN-5-1q	0.9438 \pm 0.035	0.0898 \pm 0.0898	2.9 \pm 0.32
MLP500-ReLU	0.8892 \pm 0.0036	0.117 \pm 0.117	2001.0 \pm 0.0
SVR-poly	0.8841 \pm 0.0009	0.1277 \pm 0.1277	1287.4 \pm 30.86
BasicEntanglerLayers-40	0.869 \pm 0.0164	0.1424 \pm 0.1424	80.0 \pm 0.0
BasicEntanglerLayers-60	0.8645 \pm 0.0198	0.1448 \pm 0.1448	120.0 \pm 0.0
BasicEntanglerLayers-20	0.857 \pm 0.024	0.1488 \pm 0.1486	40.0 \pm 0.0
BasicEntanglerLayers-10	0.8051 \pm 0.0207	0.1738 \pm 0.1738	20.0 \pm 0.0
BasicEntanglerLayers-9	0.7894 \pm 0.0269	0.1806 \pm 0.1806	18.0 \pm 0.0
BasicEntanglerLayers-7	0.7794 \pm 0.0252	0.1848 \pm 0.1848	14.0 \pm 0.0
BasicEntanglerLayers-6	0.7402 \pm 0.0285	0.2007 \pm 0.2007	12.0 \pm 0.0
BasicEntanglerLayers-5	0.7146 \pm 0.0563	0.2098 \pm 0.2098	10.0 \pm 0.0
BasicEntanglerLayers-3	0.7139 \pm 0.0003	0.2109 \pm 0.2109	6.0 \pm 0.0
BasicEntanglerLayers-4	0.6536 \pm 0.1558	0.2282 \pm 0.2282	8.0 \pm 0.0
SimplifiedTwoDesign-10	0.4573 \pm 0.003	0.2904 \pm 0.2904	22.0 \pm 0.0
SimplifiedTwoDesign-9	0.4555 \pm 0.0037	0.2909 \pm 0.2909	20.0 \pm 0.0
SimplifiedTwoDesign-20	0.4554 \pm 0.0043	0.2909 \pm 0.2909	42.0 \pm 0.0
SimplifiedTwoDesign-7	0.4541 \pm 0.0051	0.2913 \pm 0.2913	16.0 \pm 0.0
SimplifiedTwoDesign-6	0.447 \pm 0.014	0.2931 \pm 0.2931	14.0 \pm 0.0
SimplifiedTwoDesign-5	0.4384 \pm 0.0162	0.2954 \pm 0.2954	12.0 \pm 0.0
StronglyEntanglingLayers-3	0.4346 \pm 0.0002	0.2964 \pm 0.2964	18.0 \pm 0.0
SimplifiedTwoDesign-3	0.4164 \pm 0.0035	0.3011 \pm 0.3011	8.0 \pm 0.0
SimplifiedTwoDesign-4	0.4069 \pm 0.0356	0.3035 \pm 0.3035	10.0 \pm 0.0
SimplifiedTwoDesign-40	0.3519 \pm 0.0945	0.3163 \pm 0.3166	82.0 \pm 0.0
SimplifiedTwoDesign-60	0.326 \pm 0.0487	0.3234 \pm 0.3234	122.0 \pm 0.0
SVR-linear	-inf \pm inf	0.4143 \pm 0.4143	2.0 \pm 0.0
MLP100-100-1d	-inf \pm inf	0.3988 \pm 0.3988	10501.0 \pm 0.0
MLP500-500-1d	-inf \pm inf	0.3973 \pm 0.3973	252501.0 \pm 0.0
MLP500-1d	-inf \pm 61.9169	0.395 \pm 0.395	2001.0 \pm 0.0
MLP100-1d	-24.1022 \pm 3.4995	0.4042 \pm 0.4042	401.0 \pm 0.0
StronglyEntanglingLayers-1	-17.2832 \pm 0.0	1.6855 \pm 1.6855	6.0 \pm 0.0
MLP100-ReLU	-1.354 \pm 0.0999	0.2598 \pm 0.2598	401.0 \pm 0.0
SimplifiedTwoDesign-2	-0.1148 \pm 0.0638	0.416 \pm 0.416	6.0 \pm 0.0
SVR-sigmoid	-0.0617 \pm 0.0142	75.8526 \pm 75.8526	3344.6 \pm 2.99
BasicEntanglerLayers-2	-0.0001 \pm 0.0007	0.3942 \pm 0.3942	4.0 \pm 0.0
StronglyEntanglingLayers-2	-0.0001 \pm 0.0001	0.3942 \pm 0.3942	12.0 \pm 0.0
SimplifiedTwoDesign-1	-0.0001 \pm 0.0001	0.3942 \pm 0.3942	4.0 \pm 0.0
BasicEntanglerLayers-1	-0.0001 \pm 0.0001	0.3942 \pm 0.3942	2.0 \pm 0.0

Table B7 Results of the benchmark Function 6

Model	R^2 -score \pm std	RMSE \pm std	#Params \pm std
RF	0.8592 \pm 0.0042	0.1275 \pm 0.1275	206265.8 \pm 319.62
DT	0.8532 \pm 0.0103	0.1507 \pm 0.1507	3250.6 \pm 9.08
knn2	0.8086 \pm 0.0067	0.1583 \pm 0.1583	0.0 \pm 0.0
knn3	0.8042 \pm 0.0084	0.1508 \pm 0.1508	0.0 \pm 0.0
knn4	0.771 \pm 0.0112	0.1563 \pm 0.1563	0.0 \pm 0.0
SimplifiedTwoDesign-60	0.7133 \pm 0.0647	0.2106 \pm 0.2106	122.0 \pm 0.0
BasicEntanglerLayers-60	0.656 \pm 0.0312	0.2319 \pm 0.2319	120.0 \pm 0.0
SimplifiedTwoDesign-40	0.6518 \pm 0.0584	0.2328 \pm 0.2328	82.0 \pm 0.0
StronglyEntanglingLayers-60	0.6304 \pm 0.0182	0.2405 \pm 0.2405	360.0 \pm 0.0
StronglyEntanglingLayers-40	0.583 \pm 0.01	0.2555 \pm 0.2555	240.0 \pm 0.0
BasicEntanglerLayers-40	0.5333 \pm 0.0281	0.2702 \pm 0.2702	80.0 \pm 0.0
StronglyEntanglingLayers-20	0.4761 \pm 0.0147	0.2864 \pm 0.2864	120.0 \pm 0.0
SimplifiedTwoDesign-20	0.3866 \pm 0.0299	0.3098 \pm 0.3098	42.0 \pm 0.0
BasicEntanglerLayers-20	0.3626 \pm 0.0087	0.3159 \pm 0.3159	40.0 \pm 0.0
StronglyEntanglingLayers-10	0.3599 \pm 0.0051	0.3166 \pm 0.3166	60.0 \pm 0.0
SimplifiedTwoDesign-10	0.3561 \pm 0.0032	0.3175 \pm 0.3175	22.0 \pm 0.0
StronglyEntanglingLayers-9	0.356 \pm 0.004	0.3175 \pm 0.3175	54.0 \pm 0.0
StronglyEntanglingLayers-7	0.3517 \pm 0.0035	0.3186 \pm 0.3186	42.0 \pm 0.0
SimplifiedTwoDesign-9	0.3511 \pm 0.007	0.3187 \pm 0.3187	20.0 \pm 0.0
BasicEntanglerLayers-10	0.3501 \pm 0.0064	0.319 \pm 0.319	20.0 \pm 0.0
SimplifiedTwoDesign-5	0.35 \pm 0.0076	0.319 \pm 0.319	12.0 \pm 0.0
SimplifiedTwoDesign-7	0.3495 \pm 0.0065	0.3191 \pm 0.3191	16.0 \pm 0.0
BasicEntanglerLayers-9	0.3492 \pm 0.0076	0.3192 \pm 0.3192	18.0 \pm 0.0
StronglyEntanglingLayers-6	0.3483 \pm 0.0028	0.3194 \pm 0.3194	36.0 \pm 0.0
StronglyEntanglingLayers-5	0.345 \pm 0.0027	0.3203 \pm 0.3203	30.0 \pm 0.0
SimplifiedTwoDesign-6	0.3439 \pm 0.0103	0.3205 \pm 0.3205	14.0 \pm 0.0
BasicEntanglerLayers-7	0.3421 \pm 0.0164	0.3209 \pm 0.3209	14.0 \pm 0.0
StronglyEntanglingLayers-4	0.3415 \pm 0.0144	0.3211 \pm 0.3211	24.0 \pm 0.0
BasicEntanglerLayers-6	0.3383 \pm 0.0172	0.3219 \pm 0.3219	12.0 \pm 0.0
BasicEntanglerLayers-5	0.3383 \pm 0.0075	0.3219 \pm 0.3219	10.0 \pm 0.0
SimplifiedTwoDesign-3	0.3364 \pm 0.0103	0.3223 \pm 0.3223	8.0 \pm 0.0
SimplifiedTwoDesign-4	0.3236 \pm 0.0255	0.3254 \pm 0.3254	10.0 \pm 0.0
BasicEntanglerLayers-4	0.3074 \pm 0.0248	0.3293 \pm 0.3293	8.0 \pm 0.0
BasicEntanglerLayers-3	0.3052 \pm 0.0562	0.3296 \pm 0.3296	6.0 \pm 0.0
SimplifiedTwoDesign-2	0.2546 \pm 0.1346	0.3405 \pm 0.3405	6.0 \pm 0.0
RRQNN-20-2q	0.207 \pm 0.0362	0.3523 \pm 0.3523	13.6 \pm 1.78
RRQNN-10-1q	0.2029 \pm 0.0219	0.3533 \pm 0.3533	6.2 \pm 0.92
StronglyEntanglingLayers-3	0.1708 \pm 0.0004	0.3603 \pm 0.3603	18.0 \pm 0.0
RRQNN-20-1q	0.1283 \pm 0.0701	0.3692 \pm 0.3692	16.3 \pm 0.82
RRQNN-5-1q	0.0887 \pm 0.0809	0.3774 \pm 0.3774	3.3 \pm 0.67
RRQNN-120-1q	0.0864 \pm 0.0505	0.3781 \pm 0.3781	70.3 \pm 4.72
RRQNN-120-2q	0.0418 \pm 0.066	0.3871 \pm 0.3871	66.5 \pm 4.84
RRQNN-40-2q	0.0236 \pm 0.0953	0.3905 \pm 0.3905	26.5 \pm 3.27
MLP500-500-Id	-inf \pm inf	0.4015 \pm 0.4015	252501.0 \pm 0.0
SVR-linear	-inf \pm inf	0.4063 \pm 0.4063	2.0 \pm 0.0
MLP500-Id	-inf \pm inf	0.3981 \pm 0.3981	2001.0 \pm 0.0
MLP100-100-Id	-inf \pm 76.9552	0.4016 \pm 0.4016	10501.0 \pm 0.0
MLP100-1d	-inf \pm 44.3239	0.397 \pm 0.397	401.0 \pm 0.0
SVR-poly	-7.1165 \pm 0.9332	0.3834 \pm 0.3834	2711.0 \pm 17.34
MLP500-ReLU	-5.4497 \pm 0.4199	0.3426 \pm 0.3426	2001.0 \pm 0.0
MLP100-ReLU	-17.4302 \pm 1.3218	0.3784 \pm 0.3784	401.0 \pm 0.0
StronglyEntanglingLayers-1	-11.6 \pm 0.0	1.4046 \pm 1.4046	6.0 \pm 0.0
MLP100-100-ReLU	-1.4455 \pm 0.1776	0.3242 \pm 0.3242	10501.0 \pm 0.0
SVR-RBF	-1.2615 \pm 0.1422	0.3226 \pm 0.3226	2603.2 \pm 21.57
MLP500-500-ReLU	-1.0509 \pm 0.115	0.328 \pm 0.328	252501.0 \pm 0.0
RRQNN-60-1q	-0.2506 \pm 0.04	0.4425 \pm 0.4425	34.1 \pm 2.23
RRQNN-40-1q	-0.1447 \pm 0.1135	0.4228 \pm 0.4228	28.1 \pm 4.98
RRQNN-60-2q	-0.1318 \pm 0.0323	0.4209 \pm 0.4209	34.2 \pm 3.74
SVR-sigmoid	0.0609 \pm 0.0138	75.8276 \pm 75.8276	3347.6 \pm 2.07
BasicEntanglerLayers-2	-0.0007 \pm 0.0008	0.3958 \pm 0.3958	4.0 \pm 0.0
StronglyEntanglingLayers-2	-0.0002 \pm 0.0003	0.3957 \pm 0.3957	12.0 \pm 0.0
SimplifiedTwoDesign-1	-0.0002 \pm 0.0003	0.3957 \pm 0.3957	4.0 \pm 0.0
BasicEntanglerLayers-1	-0.0002 \pm 0.0003	0.3957 \pm 0.3957	2.0 \pm 0.0

Table B8 Results of the benchmark Function 7

Model	R^2 -score \pm std	RMSE \pm std	#Params \pm std
RF	0.9927 \pm 0.0005	0.03 \pm 0.03	206403.6 \pm 346.53
DT	0.9906 \pm 0.0006	0.0343 \pm 0.0343	3254.4 \pm 8.11
knn3	0.9854 \pm 0.0007	0.0424 \pm 0.0424	0.0 \pm 0.0
knn4	0.9845 \pm 0.0009	0.0436 \pm 0.0436	0.0 \pm 0.0
knn2	0.983 \pm 0.0008	0.046 \pm 0.046	0.0 \pm 0.0
StronglyEntanglingLayers-20	0.9431 \pm 0.0044	0.0846 \pm 0.0846	120.0 \pm 0.0
SimplifiedTwoDesign-20	0.943 \pm 0.0039	0.0847 \pm 0.0847	42.0 \pm 0.0
RRQNN-120-2q	0.9425 \pm 0.0014	0.0851 \pm 0.0851	83.0 \pm 4.45
StronglyEntanglingLayers-10	0.9416 \pm 0.0012	0.0857 \pm 0.0857	60.0 \pm 0.0
SimplifiedTwoDesign-10	0.9414 \pm 0.0024	0.0859 \pm 0.0859	22.0 \pm 0.0
StronglyEntanglingLayers-40	0.9411 \pm 0.0064	0.086 \pm 0.086	240.0 \pm 0.0
StronglyEntanglingLayers-9	0.9406 \pm 0.0017	0.0865 \pm 0.0865	54.0 \pm 0.0
StronglyEntanglingLayers-60	0.9404 \pm 0.0057	0.0865 \pm 0.0865	360.0 \pm 0.0
RRQNN-60-2q	0.9392 \pm 0.0019	0.0874 \pm 0.0874	42.8 \pm 2.53
SimplifiedTwoDesign-9	0.938 \pm 0.0029	0.0883 \pm 0.0883	20.0 \pm 0.0
BasicEntanglerLayers-20	0.9378 \pm 0.0154	0.088 \pm 0.088	40.0 \pm 0.0
SVR-RBF	0.9377 \pm 0.0004	0.0851 \pm 0.0851	873.0 \pm 25.82
StronglyEntanglingLayers-7	0.9376 \pm 0.0014	0.088 \pm 0.0886	42.0 \pm 0.0
RRQNN-40-2q	0.9365 \pm 0.0011	0.0893 \pm 0.0893	28.7 \pm 2.21
BasicEntanglerLayers-10	0.9353 \pm 0.0051	0.0902 \pm 0.0902	20.0 \pm 0.0
StronglyEntanglingLayers-6	0.935 \pm 0.0038	0.0904 \pm 0.0904	36.0 \pm 0.0
RRQNN-120-1q	0.9343 \pm 0.0042	0.0909 \pm 0.0909	78.4 \pm 4.6
BasicEntanglerLayers-9	0.933 \pm 0.0069	0.0917 \pm 0.0917	18.0 \pm 0.0
MLP500-500-ReLU	0.933 \pm 0.002	0.0884 \pm 0.0884	252501.0 \pm 0.0
RRQNN-60-1q	0.9306 \pm 0.0065	0.0934 \pm 0.0934	40.0 \pm 3.06
SimplifiedTwoDesign-7	0.9304 \pm 0.0138	0.0933 \pm 0.0933	16.0 \pm 0.0
BasicEntanglerLayers-7	0.9285 \pm 0.0099	0.094 \pm 0.0946	14.0 \pm 0.0
BasicEntanglerLayers-6	0.9284 \pm 0.0053	0.0949 \pm 0.0949	12.0 \pm 0.0
RRQNN-40-1q	0.9282 \pm 0.0028	0.095 \pm 0.095	27.1 \pm 1.97
RRQNN-20-2q	0.9244 \pm 0.0135	0.0972 \pm 0.0972	13.9 \pm 1.45
BasicEntanglerLayers-40	0.9217 \pm 0.0233	0.0984 \pm 0.0984	80.0 \pm 0.0
SimplifiedTwoDesign-6	0.9178 \pm 0.0239	0.1009 \pm 0.1009	14.0 \pm 0.0
RRQNN-20-1q	0.9156 \pm 0.0059	0.1031 \pm 0.1031	13.1 \pm 1.91
SimplifiedTwoDesign-40	0.8974 \pm 0.0563	0.11 \pm 0.11	82.0 \pm 0.0
SimplifiedTwoDesign-5	0.8974 \pm 0.0287	0.1126 \pm 0.1126	12.0 \pm 0.0
StronglyEntanglingLayers-5	0.885 \pm 0.047	0.1182 \pm 0.1182	30.0 \pm 0.0
SimplifiedTwoDesign-60	0.879 \pm 0.063	0.12 \pm 0.12	122.0 \pm 0.0
BasicEntanglerLayers-60	0.8719 \pm 0.0306	0.1262 \pm 0.1262	120.0 \pm 0.0
SimplifiedTwoDesign-4	0.8636 \pm 0.0271	0.1301 \pm 0.1306	10.0 \pm 0.0
BasicEntanglerLayers-5	0.8612 \pm 0.0991	0.1257 \pm 0.1257	10.0 \pm 0.0
RRQNN-10-1q	0.8586 \pm 0.0961	0.1284 \pm 0.1284	5.6 \pm 0.52
SimplifiedTwoDesign-3	0.7208 \pm 0.0002	0.1875 \pm 0.1875	8.0 \pm 0.0
BasicEntanglerLayers-4	0.6885 \pm 0.1659	0.1897 \pm 0.1897	8.0 \pm 0.0
BasicEntanglerLayers-3	0.6841 \pm 0.0002	0.1994 \pm 0.1994	6.0 \pm 0.0
MLP500-ReLU	0.6189 \pm 0.0417	0.1544 \pm 0.1544	2001.0 \pm 0.0
StronglyEntanglingLayers-4	0.5236 \pm 0.0026	0.2449 \pm 0.2449	24.0 \pm 0.0
MLP100-100-ReLU	0.4819 \pm 0.0248	0.174 \pm 0.174	10501.0 \pm 0.0
StronglyEntanglingLayers-3	0.3353 \pm 0.0001	0.2893 \pm 0.2893	18.0 \pm 0.0
RRQNN-5-1q	0.027 \pm 0.1223	0.3494 \pm 0.3494	3.1 \pm 0.88
MLP500-500-1d	-inf \pm inf	0.3568 \pm 0.3568	252501.0 \pm 0.0
SVR-linear	-inf \pm inf	0.3597 \pm 0.3597	2.0 \pm 0.0
MLP100-1d	-inf \pm inf	0.3555 \pm 0.3555	401.0 \pm 0.0
MLP100-100-1d	-inf \pm inf	0.356 \pm 0.356	10501.0 \pm 0.0
MLP500-1d	-inf \pm inf	0.356 \pm 0.356	2001.0 \pm 0.0
StronglyEntanglingLayers-1	-3.1534 \pm 0.0	0.7231 \pm 0.7231	6.0 \pm 0.0
SVR-poly	-1.7151 \pm 0.1058	0.3039 \pm 0.3039	2294.4 \pm 20.67
MLP100-ReLU	-0.664 \pm 0.0562	0.2331 \pm 0.2331	401.0 \pm 0.0
SVR-sigmoid	-0.0592 \pm 0.0142	75.7682 \pm 75.7682	3347.4 \pm 1.9
SimplifiedTwoDesign-2	-0.0005 \pm 0.0006	0.3549 \pm 0.3549	6.0 \pm 0.0
BasicEntanglerLayers-2	-0.0002 \pm 0.0002	0.3549 \pm 0.3549	4.0 \pm 0.0
StronglyEntanglingLayers-2	-0.0001 \pm 0.0001	0.3548 \pm 0.3548	12.0 \pm 0.0
SimplifiedTwoDesign-1	-0.0001 \pm 0.0001	0.3548 \pm 0.3548	4.0 \pm 0.0
BasicEntanglerLayers-1	-0.0001 \pm 0.0001	0.3548 \pm 0.3548	2.0 \pm 0.0

Table B9 Results of the benchmark Function 8

Model	R^2 -score \pm std	RMSE \pm std	#Params \pm std
RF	0.924 \pm 0.0042	0.0922 \pm 0.0922	206517.4 \pm 283.51
DT	0.903 \pm 0.0058	0.113 \pm 0.113	3252.4 \pm 6.8
knn3	0.869 \pm 0.006	0.1191 \pm 0.1191	0.0 \pm 0.0
knn2	0.858 \pm 0.0064	0.1292 \pm 0.1292	0.0 \pm 0.0
knn4	0.8503 \pm 0.0082	0.1237 \pm 0.1237	0.0 \pm 0.0
SimplifiedTwoDesign-40	0.6354 \pm 0.1613	0.2128 \pm 0.2128	82.0 \pm 0.0
SimplifiedTwoDesign-60	0.6213 \pm 0.0332	0.224 \pm 0.224	122.0 \pm 0.0
BasicEntanglerLayers-60	0.574 \pm 0.0308	0.2377 \pm 0.2377	120.0 \pm 0.0
SimplifiedTwoDesign-10	0.5178 \pm 0.0031	0.253 \pm 0.253	22.0 \pm 0.0
SimplifiedTwoDesign-20	0.5161 \pm 0.0296	0.2534 \pm 0.2534	42.0 \pm 0.0
StronglyEntanglingLayers-20	0.5132 \pm 0.0043	0.2542 \pm 0.2542	120.0 \pm 0.0
StronglyEntanglingLayers-10	0.5124 \pm 0.0023	0.2544 \pm 0.2544	60.0 \pm 0.0
SimplifiedTwoDesign-9	0.5116 \pm 0.0166	0.2546 \pm 0.2546	20.0 \pm 0.0
StronglyEntanglingLayers-9	0.5114 \pm 0.0026	0.2547 \pm 0.2547	54.0 \pm 0.0
SimplifiedTwoDesign-7	0.5107 \pm 0.0058	0.2549 \pm 0.2549	16.0 \pm 0.0
StronglyEntanglingLayers-7	0.5102 \pm 0.0025	0.255 \pm 0.255	42.0 \pm 0.0
StronglyEntanglingLayers-40	0.5097 \pm 0.0056	0.2551 \pm 0.2551	240.0 \pm 0.0
StronglyEntanglingLayers-60	0.5085 \pm 0.0073	0.2555 \pm 0.2555	360.0 \pm 0.0
StronglyEntanglingLayers-6	0.5068 \pm 0.0032	0.2559 \pm 0.2559	36.0 \pm 0.0
StronglyEntanglingLayers-5	0.5009 \pm 0.0037	0.2574 \pm 0.2574	30.0 \pm 0.0
BasicEntanglerLayers-20	0.5006 \pm 0.0298	0.2574 \pm 0.2574	40.0 \pm 0.0
BasicEntanglerLayers-10	0.5004 \pm 0.0352	0.2574 \pm 0.2574	20.0 \pm 0.0
BasicEntanglerLayers-9	0.4912 \pm 0.0243	0.2598 \pm 0.2598	18.0 \pm 0.0
SimplifiedTwoDesign-6	0.4895 \pm 0.0569	0.26 \pm 0.26	14.0 \pm 0.0
BasicEntanglerLayers-6	0.4869 \pm 0.0241	0.2609 \pm 0.2609	12.0 \pm 0.0
BasicEntanglerLayers-7	0.4856 \pm 0.0365	0.2612 \pm 0.2612	14.0 \pm 0.0
BasicEntanglerLayers-5	0.4823 \pm 0.0257	0.2621 \pm 0.2621	10.0 \pm 0.0
SimplifiedTwoDesign-4	0.4802 \pm 0.0141	0.2627 \pm 0.2627	10.0 \pm 0.0
BasicEntanglerLayers-40	0.4657 \pm 0.0822	0.2657 \pm 0.2657	80.0 \pm 0.0
SimplifiedTwoDesign-5	0.4447 \pm 0.0771	0.271 \pm 0.271	12.0 \pm 0.0
StronglyEntanglingLayers-4	0.4409 \pm 0.0524	0.2722 \pm 0.2722	24.0 \pm 0.0
BasicEntanglerLayers-4	0.4347 \pm 0.0525	0.2737 \pm 0.2737	8.0 \pm 0.0
SimplifiedTwoDesign-3	0.4221 \pm 0.0887	0.2763 \pm 0.2763	8.0 \pm 0.0
BasicEntanglerLayers-3	0.3919 \pm 0.11	0.2831 \pm 0.2831	6.0 \pm 0.0
RRQNN-20-2q	0.3882 \pm 0.038	0.2849 \pm 0.2849	15.5 \pm 0.97
RRQNN-20-1q	0.2855 \pm 0.0933	0.3074 \pm 0.3074	13.8 \pm 1.99
RRQNN-10-1q	0.2737 \pm 0.1162	0.3096 \pm 0.3096	5.9 \pm 0.88
StronglyEntanglingLayers-3	0.2567 \pm 0.0003	0.3141 \pm 0.3141	18.0 \pm 0.0
RRQNN-40-2q	0.2513 \pm 0.0227	0.3153 \pm 0.3153	26.8 \pm 3.39
SimplifiedTwoDesign-2	0.1893 \pm 0.1308	0.3272 \pm 0.3272	6.0 \pm 0.0
RRQNN-60-2q	0.1779 \pm 0.0323	0.3303 \pm 0.3303	36.8 \pm 4.24
RRQNN-40-1q	0.1612 \pm 0.0233	0.3337 \pm 0.3337	27.8 \pm 3.26
RRQNN-120-2q	0.1406 \pm 0.0146	0.3378 \pm 0.3378	74.2 \pm 3.43
RRQNN-5-1q	0.1205 \pm 0.1263	0.341 \pm 0.341	3.0 \pm 1.15
RRQNN-60-1q	0.1132 \pm 0.0097	0.3431 \pm 0.3431	39.1 \pm 3.96
RRQNN-120-1q	0.104 \pm 0.0166	0.3449 \pm 0.3449	78.0 \pm 4.32
SVR-RBF	0.0797 \pm 0.0244	0.2543 \pm 0.2543	2300.4 \pm 13.02
SVR-linear	-inf \pm inf	0.3646 \pm 0.3646	2.0 \pm 0.0
MLP500-500-Id	-inf \pm inf	0.366 \pm 0.366	252501.0 \pm 0.0
MLP100-1Id	-inf \pm inf	0.3646 \pm 0.3646	401.0 \pm 0.0
MLP100-100-Id	-inf \pm inf	0.3699 \pm 0.3699	10501.0 \pm 0.0
MLP500-Id	-inf \pm inf	0.3665 \pm 0.3665	2001.0 \pm 0.0
StronglyEntanglingLayers-1	-8.5238 \pm 0.0	1.1245 \pm 1.1245	6.0 \pm 0.0
MLP100-ReLU	-6.4564 \pm 0.4773	0.3161 \pm 0.3161	401.0 \pm 0.0
SVR-poly	-3.2694 \pm 0.2641	0.3335 \pm 0.3335	2615.8 \pm 25.98
MLP500-ReLU	-1.1733 \pm 0.1268	0.2762 \pm 0.2762	2001.0 \pm 0.0
MLP100-100-ReLU	-0.2609 \pm 0.0358	0.262 \pm 0.262	10501.0 \pm 0.0
MLP500-500-ReLU	-0.0642 \pm 0.0916	0.261 \pm 0.261	252501.0 \pm 0.0
SVR-sigmoid	-0.0606 \pm 0.014	75.8191 \pm 75.8191	3347.6 \pm 2.07
BasicEntanglerLayers-2	-0.0006 \pm 0.0005	0.3645 \pm 0.3645	4.0 \pm 0.0
StronglyEntanglingLayers-2	-0.0001 \pm 0.0001	0.3644 \pm 0.3644	12.0 \pm 0.0
SimplifiedTwoDesign-1	-0.0001 \pm 0.0001	0.3644 \pm 0.3644	4.0 \pm 0.0
BasicEntanglerLayers-1	-0.0001 \pm 0.0001	0.3644 \pm 0.3644	2.0 \pm 0.0

Table B10 Results of the benchmark Function 9

Model	R^2 -score \pm std	RMSE \pm std	#Params \pm std
RF	0.9969 \pm 0.0003	0.0212 \pm 0.0212	210831.4 \pm 41.85
DT	0.9949 \pm 0.0004	0.0272 \pm 0.0272	3346.6 \pm 1.84
knn3	0.9921 \pm 0.0004	0.0337 \pm 0.0337	0.0 \pm 0.0
knn4	0.9921 \pm 0.0003	0.0336 \pm 0.0336	0.0 \pm 0.0
knn2	0.9901 \pm 0.0002	0.0378 \pm 0.0378	0.0 \pm 0.0
StronglyEntanglingLayers-40	0.9789 \pm 0.004	0.0552 \pm 0.0552	240.0 \pm 0.0
StronglyEntanglingLayers-60	0.978 \pm 0.0038	0.0565 \pm 0.0565	360.0 \pm 0.0
SimplifiedTwoDesign-20	0.9694 \pm 0.0104	0.066 \pm 0.066	42.0 \pm 0.0
RRQNN-120-2q	0.9624 \pm 0.0025	0.074 \pm 0.074	78.6 \pm 3.44
StronglyEntanglingLayers-20	0.9519 \pm 0.0106	0.0834 \pm 0.0834	120.0 \pm 0.0
BasicEntanglerLayers-20	0.9468 \pm 0.0093	0.0878 \pm 0.0878	40.0 \pm 0.0
BasicEntanglerLayers-40	0.9458 \pm 0.0249	0.0867 \pm 0.0867	80.0 \pm 0.0
SimplifiedTwoDesign-40	0.9416 \pm 0.0629	0.0836 \pm 0.0836	82.0 \pm 0.0
SimplifiedTwoDesign-10	0.9314 \pm 0.0144	0.0996 \pm 0.0996	22.0 \pm 0.0
SimplifiedTwoDesign-9	0.9267 \pm 0.013	0.103 \pm 0.103	20.0 \pm 0.0
RRQNN-120-1q	0.9266 \pm 0.0106	0.1033 \pm 0.1033	75.3 \pm 5.1
RRQNN-60-2q	0.9265 \pm 0.0037	0.1034 \pm 0.1034	38.8 \pm 2.25
StronglyEntanglingLayers-10	0.9244 \pm 0.0035	0.105 \pm 0.105	60.0 \pm 0.0
StronglyEntanglingLayers-9	0.9199 \pm 0.0028	0.1081 \pm 0.1081	54.0 \pm 0.0
SVR-RBF	0.9192 \pm 0.0008	0.104 \pm 0.104	1232.6 \pm 17.15
BasicEntanglerLayers-60	0.9189 \pm 0.0342	0.1064 \pm 0.1064	120.0 \pm 0.0
StronglyEntanglingLayers-7	0.9145 \pm 0.0037	0.1116 \pm 0.1116	42.0 \pm 0.0
RRQNN-40-2q	0.9145 \pm 0.002	0.1117 \pm 0.1117	29.4 \pm 1.65
StronglyEntanglingLayers-6	0.9128 \pm 0.0031	0.1128 \pm 0.1128	36.0 \pm 0.0
SimplifiedTwoDesign-7	0.9124 \pm 0.0031	0.1131 \pm 0.1131	16.0 \pm 0.0
BasicEntanglerLayers-10	0.9122 \pm 0.0033	0.1132 \pm 0.1132	20.0 \pm 0.0
RRQNN-60-1q	0.9101 \pm 0.0056	0.1145 \pm 0.1145	38.4 \pm 2.88
SimplifiedTwoDesign-6	0.9088 \pm 0.0049	0.1154 \pm 0.1154	14.0 \pm 0.0
SimplifiedTwoDesign-5	0.9088 \pm 0.002	0.1154 \pm 0.1154	12.0 \pm 0.0
BasicEntanglerLayers-9	0.907 \pm 0.0125	0.1163 \pm 0.1163	18.0 \pm 0.0
RRQNN-40-1q	0.904 \pm 0.0106	0.1181 \pm 0.1181	27.5 \pm 2.37
RRQNN-20-2q	0.8975 \pm 0.0065	0.1223 \pm 0.1223	13.2 \pm 1.14
SimplifiedTwoDesign-4	0.8932 \pm 0.0163	0.1245 \pm 0.1245	10.0 \pm 0.0
StronglyEntanglingLayers-5	0.8887 \pm 0.0167	0.1271 \pm 0.1271	30.0 \pm 0.0
BasicEntanglerLayers-7	0.8853 \pm 0.0413	0.1278 \pm 0.1278	14.0 \pm 0.0
RRQNN-20-1q	0.8842 \pm 0.0167	0.1297 \pm 0.1297	13.2 \pm 1.32
SimplifiedTwoDesign-60	0.8734 \pm 0.1246	0.1221 \pm 0.1221	122.0 \pm 0.0
BasicEntanglerLayers-6	0.8717 \pm 0.0474	0.1349 \pm 0.1349	12.0 \pm 0.0
MLP500-500-ReLU	0.8532 \pm 0.0157	0.1334 \pm 0.1334	252501.0 \pm 0.0
RRQNN-10-1q	0.8342 \pm 0.0267	0.1552 \pm 0.1552	5.5 \pm 0.53
SimplifiedTwoDesign-3	0.7958 \pm 0.0001	0.1726 \pm 0.1726	8.0 \pm 0.0
BasicEntanglerLayers-5	0.7709 \pm 0.077	0.1804 \pm 0.1804	10.0 \pm 0.0
BasicEntanglerLayers-3	0.694 \pm 0.0002	0.2113 \pm 0.2113	6.0 \pm 0.0
BasicEntanglerLayers-4	0.6682 \pm 0.1528	0.2136 \pm 0.2136	8.0 \pm 0.0
MLP100-100-ReLU	0.5649 \pm 0.0125	0.1842 \pm 0.1842	10501.0 \pm 0.0
StronglyEntanglingLayers-4	0.5198 \pm 0.0339	0.2645 \pm 0.2645	24.0 \pm 0.0
MLP500-ReLU	0.3877 \pm 0.0726	0.1984 \pm 0.1984	2001.0 \pm 0.0
StronglyEntanglingLayers-3	0.3482 \pm 0.0002	0.3084 \pm 0.3084	18.0 \pm 0.0
RRQNN-5-1q	0.1605 \pm 0.1988	0.3475 \pm 0.3475	3.1 \pm 0.99
MLP500-500-Id	-inf \pm inf	0.3842 \pm 0.3842	252501.0 \pm 0.0
SVR-linear	-inf \pm inf	0.3823 \pm 0.3823	2.0 \pm 0.0
MLP100-Id	-inf \pm inf	0.3822 \pm 0.3822	401.0 \pm 0.0
MLP100-100-Id	-inf \pm inf	0.3846 \pm 0.3846	10501.0 \pm 0.0
MLP500-Id	-inf \pm inf	0.3846 \pm 0.3846	2001.0 \pm 0.0
StronglyEntanglingLayers-1	-4.479 \pm 0.0	0.8942 \pm 0.8942	6.0 \pm 0.0
MLP100-ReLU	-2.1764 \pm 0.1594	0.2839 \pm 0.2839	401.0 \pm 0.0
SVR-poly	-1.5051 \pm 0.1071	0.3349 \pm 0.3349	2541.4 \pm 19.82
SVR-sigmoid	-0.0641 \pm 0.014	75.9396 \pm 75.9396	3347.0 \pm 1.94
SimplifiedTwoDesign-2	-0.0007 \pm 0.0009	0.3821 \pm 0.3821	6.0 \pm 0.0
BasicEntanglerLayers-2	-0.0002 \pm 0.0002	0.382 \pm 0.382	4.0 \pm 0.0
StronglyEntanglingLayers-2	-0.0001 \pm 0.0001	0.382 \pm 0.382	12.0 \pm 0.0
BasicEntanglerLayers-1	-0.0001 \pm 0.0001	0.382 \pm 0.382	2.0 \pm 0.0
SimplifiedTwoDesign-1	-0.0001 \pm 0.0001	0.382 \pm 0.382	4.0 \pm 0.0

Table B11 Results of the benchmark Function 10

Model	R^2 -score \pm std	RMSE \pm std	#Params \pm std
DT	0.3967 \pm 0.044	0.2923 \pm 0.2923	3264.4 \pm 8.0
StronglyEntanglingLayers-10	0.3796 \pm 0.0019	0.2893 \pm 0.2893	60.0 \pm 0.0
StronglyEntanglingLayers-9	0.3792 \pm 0.0016	0.2894 \pm 0.2894	54.0 \pm 0.0
SimplifiedTwoDesign-9	0.379 \pm 0.0031	0.2895 \pm 0.2895	20.0 \pm 0.0
StronglyEntanglingLayers-7	0.3775 \pm 0.003	0.2898 \pm 0.2898	42.0 \pm 0.0
SimplifiedTwoDesign-10	0.3745 \pm 0.0117	0.2905 \pm 0.2905	22.0 \pm 0.0
SimplifiedTwoDesign-7	0.3743 \pm 0.0037	0.2906 \pm 0.2906	16.0 \pm 0.0
SimplifiedTwoDesign-20	0.373 \pm 0.0127	0.2909 \pm 0.2909	42.0 \pm 0.0
StronglyEntanglingLayers-6	0.3728 \pm 0.0082	0.2909 \pm 0.2909	36.0 \pm 0.0
BasicEntanglerLayers-20	0.3724 \pm 0.0085	0.291 \pm 0.291	40.0 \pm 0.0
StronglyEntanglingLayers-20	0.3715 \pm 0.0112	0.2912 \pm 0.2912	120.0 \pm 0.0
StronglyEntanglingLayers-5	0.3705 \pm 0.0063	0.2915 \pm 0.2915	30.0 \pm 0.0
BasicEntanglerLayers-10	0.3684 \pm 0.0132	0.2919 \pm 0.2919	20.0 \pm 0.0
SimplifiedTwoDesign-6	0.3677 \pm 0.0143	0.2921 \pm 0.2921	14.0 \pm 0.0
BasicEntanglerLayers-9	0.3639 \pm 0.0196	0.293 \pm 0.293	18.0 \pm 0.0
BasicEntanglerLayers-7	0.3629 \pm 0.0144	0.2932 \pm 0.2932	14.0 \pm 0.0
StronglyEntanglingLayers-40	0.3581 \pm 0.0073	0.2943 \pm 0.2943	240.0 \pm 0.0
BasicEntanglerLayers-6	0.3468 \pm 0.0221	0.2969 \pm 0.2969	12.0 \pm 0.0
StronglyEntanglingLayers-4	0.3419 \pm 0.0199	0.298 \pm 0.298	24.0 \pm 0.0
StronglyEntanglingLayers-60	0.3415 \pm 0.0284	0.298 \pm 0.298	360.0 \pm 0.0
SimplifiedTwoDesign-40	0.3399 \pm 0.0348	0.2984 \pm 0.2984	82.0 \pm 0.0
SimplifiedTwoDesign-5	0.3381 \pm 0.0497	0.2987 \pm 0.2987	12.0 \pm 0.0
BasicEntanglerLayers-5	0.3327 \pm 0.0433	0.3 \pm 0.3	10.0 \pm 0.0
BasicEntanglerLayers-40	0.3183 \pm 0.0368	0.3032 \pm 0.3032	80.0 \pm 0.0
BasicEntanglerLayers-4	0.3147 \pm 0.0544	0.3039 \pm 0.3039	8.0 \pm 0.0
SimplifiedTwoDesign-4	0.3049 \pm 0.0636	0.306 \pm 0.306	10.0 \pm 0.0
SimplifiedTwoDesign-3	0.2949 \pm 0.0671	0.3082 \pm 0.3082	8.0 \pm 0.0
BasicEntanglerLayers-3	0.2835 \pm 0.0976	0.3103 \pm 0.3103	6.0 \pm 0.0
BasicEntanglerLayers-60	0.2394 \pm 0.0499	0.3202 \pm 0.3202	120.0 \pm 0.0
StronglyEntanglingLayers-3	0.1923 \pm 0.0004	0.3302 \pm 0.3302	18.0 \pm 0.0
SimplifiedTwoDesign-2	0.164 \pm 0.0868	0.3355 \pm 0.3355	6.0 \pm 0.0
RRQNN-20-2q	0.1386 \pm 0.0599	0.3407 \pm 0.3407	13.6 \pm 1.84
SimplifiedTwoDesign-60	0.1384 \pm 0.1945	0.3391 \pm 0.3391	122.0 \pm 0.0
RF	0.0597 \pm 0.0441	0.2655 \pm 0.2655	207688.2 \pm 233.71
RRQNN-5-1q	0.0139 \pm 0.1631	0.3638 \pm 0.3638	3.3 \pm 1.06
RRQNN-20-1q	0.0021 \pm 0.0825	0.3667 \pm 0.3667	14.1 \pm 1.2
MLP500-Id	-inf \pm inf	0.3696 \pm 0.3696	2001.0 \pm 0.0
SVR-linear	-inf \pm inf	0.3675 \pm 0.3675	2.0 \pm 0.0
MLP100-Id	-inf \pm inf	0.3675 \pm 0.3675	401.0 \pm 0.0
MLP100-100-Id	-inf \pm inf	0.3722 \pm 0.3722	10501.0 \pm 0.0
MLP500-500-Id	-inf \pm inf	0.3711 \pm 0.3711	252501.0 \pm 0.0
MLP100-ReLU	-9.296 \pm 0.6593	0.3303 \pm 0.3303	401.0 \pm 0.0
StronglyEntanglingLayers-1	-8.2836 \pm 0.0	1.1193 \pm 1.1193	6.0 \pm 0.0
SVR-poly	-4.9261 \pm 0.6418	0.344 \pm 0.344	2630.6 \pm 30.71
MLP500-ReLU	-2.2673 \pm 0.194	0.3023 \pm 0.3023	2001.0 \pm 0.0
MLP100-100-ReLU	-1.0948 \pm 0.105	0.2954 \pm 0.2954	10501.0 \pm 0.0
MLP500-500-ReLU	-0.8082 \pm 0.2049	0.2958 \pm 0.2958	252501.0 \pm 0.0
knn4	-0.7504 \pm 0.0806	0.3295 \pm 0.3295	0.0 \pm 0.0
knn3	-0.6791 \pm 0.0708	0.3355 \pm 0.3355	0.0 \pm 0.0
SVR-RBF	-0.5821 \pm 0.1237	0.289 \pm 0.289	2355.2 \pm 29.44
RRQNN-120-1q	-0.4426 \pm 0.0241	0.4412 \pm 0.4412	73.7 \pm 3.02
knn2	-0.3693 \pm 0.0544	0.3275 \pm 0.3275	0.0 \pm 0.0
RRQNN-120-2q	-0.3452 \pm 0.0251	0.426 \pm 0.426	66.1 \pm 5.0
RRQNN-60-1q	-0.3438 \pm 0.0262	0.4258 \pm 0.4258	38.0 \pm 3.16
RRQNN-40-1q	-0.229 \pm 0.0428	0.4072 \pm 0.4072	29.0 \pm 2.11
RRQNN-60-2q	-0.2128 \pm 0.0209	0.4045 \pm 0.4045	32.7 \pm 4.62
RRQNN-10-1q	-0.0736 \pm 0.0519	0.3805 \pm 0.3805	6.6 \pm 1.35
SVR-sigmoid	-0.0611 \pm 0.0136	75.8341 \pm 75.8341	3345.8 \pm 1.99
RRQNN-40-2q	-0.0582 \pm 0.0417	0.3778 \pm 0.3778	25.6 \pm 2.63
BasicEntanglerLayers-2	-0.0027 \pm 0.0078	0.3679 \pm 0.3679	4.0 \pm 0.0
SimplifiedTwoDesign-1	-0.0001 \pm 0.0001	0.3674 \pm 0.3674	4.0 \pm 0.0
StronglyEntanglingLayers-2	-0.0001 \pm 0.0001	0.3674 \pm 0.3674	12.0 \pm 0.0
BasicEntanglerLayers-1	-0.0001 \pm 0.0001	0.3674 \pm 0.3674	2.0 \pm 0.0

Table B12 Results of the benchmark Function 11

Model	R^2 -score \pm std	RMSE \pm std	#Params \pm std
RF	0.9771 \pm 0.0018	0.048 \pm 0.048	210632.4 \pm 91.3
DT	0.9694 \pm 0.0021	0.0576 \pm 0.0576	3345.8 \pm 1.69
StronglyEntanglingLayers-60	0.9564 \pm 0.0087	0.0681 \pm 0.0681	360.0 \pm 0.0
knn3	0.9479 \pm 0.0031	0.0704 \pm 0.0704	0.0 \pm 0.0
knn4	0.9448 \pm 0.0041	0.0709 \pm 0.0709	0.0 \pm 0.0
knn2	0.9387 \pm 0.0027	0.0784 \pm 0.0784	0.0 \pm 0.0
StronglyEntanglingLayers-40	0.9306 \pm 0.0119	0.0861 \pm 0.0861	240.0 \pm 0.0
SimplifiedTwoDesign-60	0.8681 \pm 0.0664	0.1164 \pm 0.1164	122.0 \pm 0.0
SimplifiedTwoDesign-40	0.851 \pm 0.0458	0.125 \pm 0.125	82.0 \pm 0.0
SimplifiedTwoDesign-20	0.8151 \pm 0.1427	0.1301 \pm 0.1301	42.0 \pm 0.0
BasicEntanglerLayers-60	0.7299 \pm 0.077	0.1689 \pm 0.1689	120.0 \pm 0.0
StronglyEntanglingLayers-20	0.7189 \pm 0.0449	0.1733 \pm 0.1733	120.0 \pm 0.0
BasicEntanglerLayers-40	0.7002 \pm 0.0902	0.1778 \pm 0.1778	80.0 \pm 0.0
RRQNN-120-2q	0.6646 \pm 0.0239	0.1897 \pm 0.1897	75.9 \pm 4.61
BasicEntanglerLayers-20	0.5352 \pm 0.149	0.2205 \pm 0.2205	40.0 \pm 0.0
SimplifiedTwoDesign-10	0.4259 \pm 0.0675	0.248 \pm 0.248	22.0 \pm 0.0
SimplifiedTwoDesign-9	0.395 \pm 0.1403	0.2534 \pm 0.2534	20.0 \pm 0.0
RRQNN-120-1q	0.2487 \pm 0.047	0.284 \pm 0.284	69.0 \pm 2.91
BasicEntanglerLayers-10	0.2412 \pm 0.0733	0.2853 \pm 0.2853	20.0 \pm 0.0
StronglyEntanglingLayers-10	0.1804 \pm 0.0353	0.2967 \pm 0.2967	60.0 \pm 0.0
SimplifiedTwoDesign-7	0.1741 \pm 0.0301	0.2979 \pm 0.2979	16.0 \pm 0.0
SimplifiedTwoDesign-6	0.1722 \pm 0.026	0.2982 \pm 0.2982	14.0 \pm 0.0
BasicEntanglerLayers-9	0.1483 \pm 0.0146	0.3025 \pm 0.3025	18.0 \pm 0.0
StronglyEntanglingLayers-9	0.1448 \pm 0.0219	0.3031 \pm 0.3031	54.0 \pm 0.0
BasicEntanglerLayers-7	0.1309 \pm 0.0254	0.3055 \pm 0.3056	14.0 \pm 0.0
StronglyEntanglingLayers-7	0.1224 \pm 0.0066	0.3071 \pm 0.3071	42.0 \pm 0.0
StronglyEntanglingLayers-6	0.12 \pm 0.0038	0.3075 \pm 0.3075	36.0 \pm 0.0
SimplifiedTwoDesign-5	0.1179 \pm 0.0201	0.3079 \pm 0.3079	12.0 \pm 0.0
StronglyEntanglingLayers-5	0.11 \pm 0.009	0.3092 \pm 0.3092	30.0 \pm 0.0
BasicEntanglerLayers-6	0.1023 \pm 0.0149	0.3106 \pm 0.3106	12.0 \pm 0.0
SimplifiedTwoDesign-4	0.096 \pm 0.0195	0.3117 \pm 0.3117	10.0 \pm 0.0
BasicEntanglerLayers-5	0.0886 \pm 0.0085	0.313 \pm 0.313	10.0 \pm 0.0
BasicEntanglerLayers-4	0.0788 \pm 0.0103	0.3146 \pm 0.3146	8.0 \pm 0.0
StronglyEntanglingLayers-4	0.0712 \pm 0.0029	0.3159 \pm 0.3159	24.0 \pm 0.0
SimplifiedTwoDesign-3	0.0652 \pm 0.0067	0.3169 \pm 0.3169	8.0 \pm 0.0
SimplifiedTwoDesign-2	0.0488 \pm 0.0157	0.3197 \pm 0.3197	6.0 \pm 0.0
BasicEntanglerLayers-3	0.0458 \pm 0.0084	0.3202 \pm 0.3202	6.0 \pm 0.0
BasicEntanglerLayers-2	0.0306 \pm 0.0003	0.3228 \pm 0.3228	4.0 \pm 0.0
StronglyEntanglingLayers-3	0.0304 \pm 0.0005	0.3228 \pm 0.3228	18.0 \pm 0.0
MLP100-100-1d	-9.9794 \pm 2.7521	0.318 \pm 0.318	10501.0 \pm 0.0
StronglyEntanglingLayers-1	-9.287 \pm 0.0	0.10514 \pm 0.10514	6.0 \pm 0.0
MLP100-100-ReLU	-9.1813 \pm 1.728	0.3057 \pm 0.3057	10501.0 \pm 0.0
MLP500-500-1d	-9.1535 \pm 2.5952	0.3184 \pm 0.3184	252501.0 \pm 0.0
MLP500-500-ReLU	-6.7192 \pm 1.6363	0.298 \pm 0.298	252501.0 \pm 0.0
SVR-RBF	-5.1778 \pm 0.7247	0.3048 \pm 0.3048	2526.4 \pm 18.4
MLP100-1d	-16.9103 \pm 2.1508	0.3157 \pm 0.3157	401.0 \pm 0.0
MLP100-ReLU	-12.8779 \pm 1.7839	0.3143 \pm 0.3143	401.0 \pm 0.0
SVR-poly	-12.7505 \pm 2.1713	0.3163 \pm 0.3166	2547.4 \pm 22.53
MLP500-1d	-11.4659 \pm 3.2741	0.3179 \pm 0.3179	2001.0 \pm 0.0
MLP500-ReLU	-10.8688 \pm 2.9211	0.3116 \pm 0.3116	2001.0 \pm 0.0
SVR-linear	-10.7998 \pm 1.3996	0.3153 \pm 0.3153	2.0 \pm 0.0
RRQNN-20-1q	-1.6935 \pm 0.1179	0.5379 \pm 0.5379	9.9 \pm 2.38
RRQNN-40-1q	-1.0322 \pm 0.149	0.467 \pm 0.467	21.4 \pm 2.22
RRQNN-20-2q	-0.9853 \pm 0.3271	0.4605 \pm 0.4605	8.7 \pm 1.49
RRQNN-40-2q	-0.7392 \pm 0.168	0.4318 \pm 0.4318	20.1 \pm 1.52
RRQNN-10-1q	-0.5205 \pm 0.5593	0.3981 \pm 0.3981	5.9 \pm 1.66
RRQNN-60-1q	-0.4019 \pm 0.1041	0.3879 \pm 0.3879	33.6 \pm 2.88
RRQNN-60-2q	-0.1298 \pm 0.1024	0.3481 \pm 0.3481	33.4 \pm 2.91
SVR-sigmoid	-0.066 \pm 0.0139	76.0071 \pm 76.0071	3346.4 \pm 2.07
RRQNN-5-1q	-0.0316 \pm 0.0989	0.3327 \pm 0.3327	3.3 \pm 0.82
BasicEntanglerLayers-1	-0.0001 \pm 0.0002	0.3278 \pm 0.3278	2.0 \pm 0.0
SimplifiedTwoDesign-1	-0.0001 \pm 0.0002	0.3278 \pm 0.3278	4.0 \pm 0.0
StronglyEntanglingLayers-2	-0.0001 \pm 0.0002	0.3278 \pm 0.3278	12.0 \pm 0.0

Table B13 Results of the benchmark Function 12

Model	R^2 -score \pm std	RMSE \pm std	#Params \pm std
RF	0.9927 \pm 0.0005	0.0457 \pm 0.0457	207511.4 \pm 171.93
DT	0.9905 \pm 0.0009	0.0525 \pm 0.0525	3260.8 \pm 4.05
knn3	0.974 \pm 0.0013	0.084 \pm 0.084	0.0 \pm 0.0
knn4	0.9725 \pm 0.0014	0.0856 \pm 0.0856	0.0 \pm 0.0
knn2	0.9684 \pm 0.0009	0.0939 \pm 0.0939	0.0 \pm 0.0
StronglyEntanglingLayers-60	0.9496 \pm 0.0043	0.121 \pm 0.121	360.0 \pm 0.0
StronglyEntanglingLayers-40	0.9451 \pm 0.0025	0.1264 \pm 0.1264	240.0 \pm 0.0
SimplifiedTwoDesign-40	0.9409 \pm 0.013	0.1305 \pm 0.1305	82.0 \pm 0.0
SimplifiedTwoDesign-60	0.94 \pm 0.0188	0.1306 \pm 0.1306	122.0 \pm 0.0
SimplifiedTwoDesign-20	0.9341 \pm 0.013	0.1379 \pm 0.1379	42.0 \pm 0.0
StronglyEntanglingLayers-20	0.9335 \pm 0.0031	0.139 \pm 0.139	120.0 \pm 0.0
BasicEntanglerLayers-60	0.9279 \pm 0.0145	0.1442 \pm 0.1442	120.0 \pm 0.0
BasicEntanglerLayers-40	0.9244 \pm 0.0183	0.1473 \pm 0.1473	80.0 \pm 0.0
RRQNN-120-2q	0.9134 \pm 0.0037	0.1588 \pm 0.1588	76.0 \pm 2.26
BasicEntanglerLayers-20	0.8926 \pm 0.0115	0.1766 \pm 0.1766	40.0 \pm 0.0
RRQNN-120-1q	0.8881 \pm 0.0039	0.1803 \pm 0.1803	75.6 \pm 4.43
SimplifiedTwoDesign-10	0.8547 \pm 0.0316	0.2045 \pm 0.2045	22.0 \pm 0.0
StronglyEntanglingLayers-10	0.8279 \pm 0.0077	0.2237 \pm 0.2237	60.0 \pm 0.0
RRQNN-60-2q	0.8223 \pm 0.0124	0.2274 \pm 0.2274	39.5 \pm 0.97
RRQNN-60-1q	0.8122 \pm 0.0252	0.2332 \pm 0.2332	39.1 \pm 2.08
StronglyEntanglingLayers-9	0.8093 \pm 0.0175	0.2354 \pm 0.2354	54.0 \pm 0.0
SimplifiedTwoDesign-9	0.8036 \pm 0.0369	0.2382 \pm 0.2382	20.0 \pm 0.0
RRQNN-40-1q	0.7834 \pm 0.0176	0.2509 \pm 0.2509	25.7 \pm 2.36
RRQNN-40-2q	0.7621 \pm 0.0234	0.2628 \pm 0.2628	25.8 \pm 2.53
BasicEntanglerLayers-10	0.7491 \pm 0.0341	0.2696 \pm 0.2696	20.0 \pm 0.0
SVR-RBF	0.7471 \pm 0.0049	0.2349 \pm 0.2349	2125.4 \pm 30.29
BasicEntanglerLayers-9	0.7395 \pm 0.0627	0.2736 \pm 0.2736	18.0 \pm 0.0
SimplifiedTwoDesign-6	0.7387 \pm 0.0645	0.2741 \pm 0.2741	14.0 \pm 0.0
StronglyEntanglingLayers-7	0.7225 \pm 0.0239	0.284 \pm 0.284	42.0 \pm 0.0
SimplifiedTwoDesign-7	0.6982 \pm 0.0764	0.2942 \pm 0.2942	16.0 \pm 0.0
BasicEntanglerLayers-7	0.6962 \pm 0.046	0.2966 \pm 0.2966	14.0 \pm 0.0
RRQNN-20-1q	0.6859 \pm 0.1251	0.2981 \pm 0.2981	11.6 \pm 0.52
BasicEntanglerLayers-6	0.637 \pm 0.0692	0.3237 \pm 0.3237	12.0 \pm 0.0
BasicEntanglerLayers-5	0.5627 \pm 0.0153	0.3567 \pm 0.3567	10.0 \pm 0.0
SimplifiedTwoDesign-5	0.561 \pm 0.099	0.3556 \pm 0.3556	12.0 \pm 0.0
StronglyEntanglingLayers-6	0.501 \pm 0.0322	0.3809 \pm 0.3809	36.0 \pm 0.0
RRQNN-20-2q	0.424 \pm 0.089	0.4084 \pm 0.4084	10.5 \pm 1.35
SimplifiedTwoDesign-4	0.3444 \pm 0.1176	0.4354 \pm 0.4354	10.0 \pm 0.0
StronglyEntanglingLayers-5	0.1851 \pm 0.0486	0.4868 \pm 0.4868	30.0 \pm 0.0
StronglyEntanglingLayers-4	0.0755 \pm 0.01	0.5187 \pm 0.5187	24.0 \pm 0.0
SimplifiedTwoDesign-3	0.04 \pm 0.0396	0.5285 \pm 0.5285	8.0 \pm 0.0
SimplifiedTwoDesign-2	0.0255 \pm 0.0093	0.5326 \pm 0.5326	6.0 \pm 0.0
StronglyEntanglingLayers-3	0.0225 \pm 0.0003	0.5334 \pm 0.5334	18.0 \pm 0.0
BasicEntanglerLayers-3	0.017 \pm 0.0095	0.5349 \pm 0.5349	6.0 \pm 0.0
BasicEntanglerLayers-4	0.0086 \pm 0.0064	0.5371 \pm 0.5371	8.0 \pm 0.0
MLP500-1d	-inf \pm inf	0.5423 \pm 0.5423	2001.0 \pm 0.0
SVR-linear	-inf \pm inf	0.5402 \pm 0.5402	2.0 \pm 0.0
MLP100-1d	-inf \pm inf	0.5397 \pm 0.5397	401.0 \pm 0.0
MLP100-100-1d	-inf \pm inf	0.5443 \pm 0.5443	10501.0 \pm 0.0
MLP500-500-1d	-inf \pm inf	0.5422 \pm 0.5422	252501.0 \pm 0.0
MLP100-ReLU	-44.6664 \pm 4.8512	0.5168 \pm 0.5168	401.0 \pm 0.0
MLP100-100-ReLU	-3.7456 \pm 0.3964	0.461 \pm 0.461	10501.0 \pm 0.0
StronglyEntanglingLayers-1	-3.3459 \pm 0.0	1.1246 \pm 1.1246	6.0 \pm 0.0
SVR-poly	-16.7074 \pm 3.8739	0.5323 \pm 0.5323	2960.0 \pm 16.84
MLP500-ReLU	-14.2385 \pm 1.5953	0.4933 \pm 0.4933	2001.0 \pm 0.0
MLP500-500-ReLU	-1.3581 \pm 0.3378	0.4313 \pm 0.4313	252501.0 \pm 0.0
RRQNN-10-1q	-0.095 \pm 0.1484	0.5633 \pm 0.5633	4.3 \pm 2.45
SVR-sigmoid	-0.0616 \pm 0.0137	75.8538 \pm 75.8538	3346.6 \pm 3.13
RRQNN-5-1q	-0.0304 \pm 0.0483	0.5475 \pm 0.5475	2.8 \pm 0.92
BasicEntanglerLayers-2	-0.0005 \pm 0.0002	0.5396 \pm 0.5396	4.0 \pm 0.0
StronglyEntanglingLayers-2	-0.0002 \pm 0.0001	0.5395 \pm 0.5395	12.0 \pm 0.0
SimplifiedTwoDesign-1	-0.0002 \pm 0.0001	0.5395 \pm 0.5395	4.0 \pm 0.0
BasicEntanglerLayers-1	-0.0002 \pm 0.0001	0.5395 \pm 0.5395	2.0 \pm 0.0

Table B14 Results of the benchmark Function 13

Model	R^2 -score \pm std	RMSE \pm std	#Params \pm std
RF	0.9964 \pm 0.001	0.0205 \pm 0.0205	206958.8 \pm 254.69
DT	0.9955 \pm 0.0008	0.0233 \pm 0.0233	3274.0 \pm 5.91
StronglyEntanglingLayers-60	0.9906 \pm 0.0019	0.0337 \pm 0.0337	360.0 \pm 0.0
StronglyEntanglingLayers-40	0.9882 \pm 0.0016	0.0379 \pm 0.0379	240.0 \pm 0.0
knn3	0.9792 \pm 0.0023	0.0482 \pm 0.0482	0.0 \pm 0.0
knn2	0.9791 \pm 0.002	0.049 \pm 0.049	0.0 \pm 0.0
RRQNN-120-1q	0.9784 \pm 0.0028	0.0512 \pm 0.0512	77.3 \pm 4.88
knn4	0.9757 \pm 0.0032	0.0513 \pm 0.0513	0.0 \pm 0.0
StronglyEntanglingLayers-20	0.9743 \pm 0.0052	0.0558 \pm 0.0558	120.0 \pm 0.0
RRQNN-120-2q	0.9717 \pm 0.0038	0.0588 \pm 0.0588	80.6 \pm 3.34
SimplifiedTwoDesign-20	0.9624 \pm 0.0231	0.0651 \pm 0.0651	42.0 \pm 0.0
BasicEntanglerLayers-60	0.9513 \pm 0.0112	0.0769 \pm 0.0769	120.0 \pm 0.0
BasicEntanglerLayers-40	0.9435 \pm 0.0224	0.0819 \pm 0.0819	80.0 \pm 0.0
RRQNN-60-1q	0.9384 \pm 0.0096	0.0868 \pm 0.0868	39.6 \pm 2.95
SimplifiedTwoDesign-40	0.9368 \pm 0.0987	0.0707 \pm 0.0707	82.0 \pm 0.0
SVR-RBF	0.9339 \pm 0.0022	0.0861 \pm 0.0861	761.8 \pm 28.4
RRQNN-60-2q	0.9097 \pm 0.0142	0.1049 \pm 0.1049	40.0 \pm 2.0
RRQNN-40-1q	0.901 \pm 0.0284	0.109 \pm 0.109	25.4 \pm 2.91
StronglyEntanglingLayers-10	0.8993 \pm 0.0236	0.1106 \pm 0.1106	60.0 \pm 0.0
SimplifiedTwoDesign-60	0.8986 \pm 0.1135	0.094 \pm 0.094	122.0 \pm 0.0
BasicEntanglerLayers-20	0.8818 \pm 0.0413	0.1191 \pm 0.1191	40.0 \pm 0.0
SimplifiedTwoDesign-10	0.8764 \pm 0.0432	0.1213 \pm 0.1213	22.0 \pm 0.0
StronglyEntanglingLayers-9	0.8702 \pm 0.0268	0.1256 \pm 0.1256	54.0 \pm 0.0
RRQNN-40-2q	0.8527 \pm 0.0226	0.1341 \pm 0.1341	28.2 \pm 1.75
SimplifiedTwoDesign-9	0.8348 \pm 0.0419	0.1413 \pm 0.1413	20.0 \pm 0.0
StronglyEntanglingLayers-7	0.781 \pm 0.0435	0.1632 \pm 0.1632	42.0 \pm 0.0
StronglyEntanglingLayers-6	0.7804 \pm 0.0253	0.1639 \pm 0.1639	36.0 \pm 0.0
SimplifiedTwoDesign-7	0.7707 \pm 0.0545	0.1665 \pm 0.1665	16.0 \pm 0.0
SimplifiedTwoDesign-6	0.7586 \pm 0.0651	0.1707 \pm 0.1707	14.0 \pm 0.0
RRQNN-20-1q	0.7423 \pm 0.0609	0.1768 \pm 0.1768	11.9 \pm 1.1
BasicEntanglerLayers-9	0.7282 \pm 0.0435	0.182 \pm 0.182	18.0 \pm 0.0
BasicEntanglerLayers-10	0.7169 \pm 0.0408	0.1859 \pm 0.1859	20.0 \pm 0.0
MLP500-500-ReLU	0.679 \pm 0.0231	0.1653 \pm 0.1653	252501.0 \pm 0.0
RRQNN-20-2q	0.6596 \pm 0.0529	0.2038 \pm 0.2038	13.3 \pm 0.95
BasicEntanglerLayers-7	0.6534 \pm 0.0616	0.2055 \pm 0.2055	14.0 \pm 0.0
StronglyEntanglingLayers-5	0.629 \pm 0.0451	0.213 \pm 0.213	30.0 \pm 0.0
SimplifiedTwoDesign-4	0.626 \pm 0.1174	0.212 \pm 0.212	10.0 \pm 0.0
SimplifiedTwoDesign-5	0.6043 \pm 0.0631	0.2197 \pm 0.2197	12.0 \pm 0.0
RRQNN-10-1q	0.5878 \pm 0.0484	0.2244 \pm 0.2246	6.2 \pm 1.14
BasicEntanglerLayers-6	0.5593 \pm 0.0306	0.2324 \pm 0.2324	12.0 \pm 0.0
BasicEntanglerLayers-5	0.5503 \pm 0.0538	0.2345 \pm 0.2345	10.0 \pm 0.0
StronglyEntanglingLayers-4	0.5416 \pm 0.0771	0.2365 \pm 0.2365	24.0 \pm 0.0
MLP100-100-ReLU	0.4466 \pm 0.0343	0.198 \pm 0.198	10501.0 \pm 0.0
BasicEntanglerLayers-4	0.4109 \pm 0.0819	0.2683 \pm 0.2683	8.0 \pm 0.0
BasicEntanglerLayers-3	0.4037 \pm 0.0434	0.2704 \pm 0.2704	6.0 \pm 0.0
SimplifiedTwoDesign-3	0.3661 \pm 0.0254	0.2788 \pm 0.2788	8.0 \pm 0.0
StronglyEntanglingLayers-3	0.3264 \pm 0.0005	0.2875 \pm 0.2875	18.0 \pm 0.0
RRQNN-5-1q	0.2935 \pm 0.1795	0.2921 \pm 0.2921	2.6 \pm 0.7
MLP500-500-1d	-inf \pm inf	0.353 \pm 0.353	252501.0 \pm 0.0
MLP100-100-1d	-inf \pm inf	0.3561 \pm 0.3561	10501.0 \pm 0.0
SVR-linear	-inf \pm inf	0.3752 \pm 0.3752	2.0 \pm 0.0
MLP500-1d	-inf \pm inf	0.3515 \pm 0.3515	2001.0 \pm 0.0
MLP100-ReLU	-8.0018 \pm 0.9045	0.3277 \pm 0.3276	401.0 \pm 0.0
SVR-poly	-3.2176 \pm 0.3383	0.3163 \pm 0.3163	1974.8 \pm 21.11
StronglyEntanglingLayers-1	-24.7687 \pm 0.0	1.7782 \pm 1.7782	6.0 \pm 0.0
MLP100-1d	-11.2508 \pm 0.7487	0.3693 \pm 0.3693	401.0 \pm 0.0
MLP500-ReLU	-1.3199 \pm 0.099	0.2518 \pm 0.2518	2001.0 \pm 0.0
SimplifiedTwoDesign-2	-0.2722 \pm 0.2339	0.3935 \pm 0.3935	6.0 \pm 0.0
SVR-sigmoid	-0.0609 \pm 0.0139	75.832 \pm 75.832	3347.0 \pm 2.54
BasicEntanglerLayers-2	-0.0002 \pm 0.0003	0.3504 \pm 0.3504	4.0 \pm 0.0
BasicEntanglerLayers-1	-0.0001 \pm 0.0001	0.3503 \pm 0.3503	2.0 \pm 0.0
SimplifiedTwoDesign-1	-0.0001 \pm 0.0001	0.3503 \pm 0.3503	4.0 \pm 0.0
StronglyEntanglingLayers-2	-0.0001 \pm 0.0001	0.3503 \pm 0.3503	12.0 \pm 0.0

Table B15 Results of the benchmark Function 14

Model	R^2 -score \pm std	RMSE \pm std	#Params \pm std
StronglyEntanglingLayers-60	0.9869 \pm 0.0042	0.0703 \pm 0.0703	360.0 \pm 0.0
StronglyEntanglingLayers-40	0.9722 \pm 0.0066	0.103 \pm 0.103	240.0 \pm 0.0
RF	0.9348 \pm 0.0028	0.1404 \pm 0.1404	206129.6 \pm 329.46
SimplifiedTwoDesign-60	0.9283 \pm 0.0291	0.1638 \pm 0.1638	122.0 \pm 0.0
DT	0.9153 \pm 0.0063	0.1795 \pm 0.1795	3250.2 \pm 8.6
RRQNN-120-1q	0.8962 \pm 0.0256	0.1992 \pm 0.1992	74.3 \pm 3.09
knn3	0.8935 \pm 0.0074	0.1802 \pm 0.1802	0.0 \pm 0.0
BasicEntanglerLayers-60	0.8926 \pm 0.0253	0.2028 \pm 0.2028	120.0 \pm 0.0
knn4	0.8887 \pm 0.0082	0.1777 \pm 0.1777	0.0 \pm 0.0
knn2	0.8765 \pm 0.0054	0.2036 \pm 0.2036	0.0 \pm 0.0
SimplifiedTwoDesign-40	0.8639 \pm 0.0515	0.2253 \pm 0.2253	82.0 \pm 0.0
BasicEntanglerLayers-40	0.8326 \pm 0.0623	0.2508 \pm 0.2508	80.0 \pm 0.0
SimplifiedTwoDesign-20	0.519 \pm 0.055	0.431 \pm 0.431	42.0 \pm 0.0
BasicEntanglerLayers-20	0.4799 \pm 0.0574	0.4482 \pm 0.4482	40.0 \pm 0.0
StronglyEntanglingLayers-20	0.3995 \pm 0.0716	0.4814 \pm 0.4814	120.0 \pm 0.0
RRQNN-120-2q	0.1587 \pm 0.1807	0.5679 \pm 0.5679	63.2 \pm 6.09
SimplifiedTwoDesign-10	0.0384 \pm 0.0279	0.6103 \pm 0.6103	22.0 \pm 0.0
StronglyEntanglingLayers-10	0.0296 \pm 0.0025	0.6131 \pm 0.6131	60.0 \pm 0.0
StronglyEntanglingLayers-9	0.0255 \pm 0.0037	0.6144 \pm 0.6144	54.0 \pm 0.0
SimplifiedTwoDesign-9	0.0254 \pm 0.0179	0.6144 \pm 0.6144	20.0 \pm 0.0
SimplifiedTwoDesign-7	0.0171 \pm 0.009	0.617 \pm 0.617	16.0 \pm 0.0
BasicEntanglerLayers-10	0.0116 \pm 0.0042	0.6188 \pm 0.6188	20.0 \pm 0.0
StronglyEntanglingLayers-7	0.0101 \pm 0.0029	0.6192 \pm 0.6192	42.0 \pm 0.0
BasicEntanglerLayers-9	0.0087 \pm 0.0053	0.6197 \pm 0.6197	18.0 \pm 0.0
SimplifiedTwoDesign-6	0.0081 \pm 0.0025	0.6199 \pm 0.6199	14.0 \pm 0.0
BasicEntanglerLayers-7	0.0062 \pm 0.0022	0.6204 \pm 0.6204	14.0 \pm 0.0
SimplifiedTwoDesign-5	0.0055 \pm 0.0028	0.6206 \pm 0.6206	12.0 \pm 0.0
StronglyEntanglingLayers-6	0.0053 \pm 0.0025	0.6207 \pm 0.6207	36.0 \pm 0.0
BasicEntanglerLayers-6	0.0033 \pm 0.0015	0.6214 \pm 0.6214	12.0 \pm 0.0
SimplifiedTwoDesign-3	0.0028 \pm 0.0015	0.6215 \pm 0.6215	8.0 \pm 0.0
StronglyEntanglingLayers-5	0.0026 \pm 0.0017	0.6215 \pm 0.6215	30.0 \pm 0.0
BasicEntanglerLayers-5	0.0026 \pm 0.0017	0.6216 \pm 0.6216	10.0 \pm 0.0
SimplifiedTwoDesign-4	0.0018 \pm 0.0025	0.6218 \pm 0.6218	10.0 \pm 0.0
StronglyEntanglingLayers-4	0.0003 \pm 0.0015	0.6223 \pm 0.6223	24.0 \pm 0.0
BasicEntanglerLayers-4	0.0003 \pm 0.0009	0.6223 \pm 0.6223	8.0 \pm 0.0
MLP100-ReLU	-inf \pm inf	0.6219 \pm 0.6219	401.0 \pm 0.0
MLP500-Id	-inf \pm inf	0.6238 \pm 0.6238	2001.0 \pm 0.0
MLP500-500-Id	-inf \pm inf	0.6297 \pm 0.6297	252501.0 \pm 0.0
MLP500-ReLU	-inf \pm inf	0.6216 \pm 0.6216	2001.0 \pm 0.0
MLP500-500-ReLU	-inf \pm inf	0.6202 \pm 0.6202	252501.0 \pm 0.0
MLP100-100-Id	-inf \pm inf	0.6257 \pm 0.6257	10501.0 \pm 0.0
MLP100-Id	-inf \pm inf	0.6228 \pm 0.6228	401.0 \pm 0.0
SVR-linear	-inf \pm inf	0.6236 \pm 0.6236	2.0 \pm 0.0
SVR-poly	-inf \pm inf	0.6243 \pm 0.6243	3079.4 \pm 21.02
MLP100-100-ReLU	-inf \pm 89.9682	0.6203 \pm 0.6203	10501.0 \pm 0.0
SVR-RBF	-33.4997 \pm 8.4931	0.623 \pm 0.623	3077.2 \pm 20.05
StronglyEntanglingLayers-1	-2.648 \pm 0.0	1.1887 \pm 1.1887	6.0 \pm 0.0
RRQNN-40-1q	-0.7305 \pm 0.1318	0.8181 \pm 0.8181	17.5 \pm 2.46
RRQNN-60-2q	-0.7104 \pm 0.0715	0.8138 \pm 0.8138	24.8 \pm 3.94
RRQNN-20-1q	-0.7038 \pm 0.1607	0.8116 \pm 0.8116	10.2 \pm 3.16
RRQNN-40-2q	-0.6138 \pm 0.0478	0.7905 \pm 0.7905	14.7 \pm 2.5
RRQNN-60-1q	-0.3615 \pm 0.18	0.7248 \pm 0.7248	29.3 \pm 3.37
RRQNN-20-2q	-0.3269 \pm 0.1202	0.7162 \pm 0.7162	8.7 \pm 2.98
RRQNN-10-1q	-0.2542 \pm 0.2212	0.6946 \pm 0.6946	5.9 \pm 1.73
RRQNN-5-1q	-0.0845 \pm 0.1826	0.6463 \pm 0.6463	2.7 \pm 0.95
SVR-sigmoid	-0.0633 \pm 0.0141	75.9053 \pm 75.9053	3347.0 \pm 1.7
SimplifiedTwoDesign-2	-0.0007 \pm 0.0007	0.6226 \pm 0.6226	6.0 \pm 0.0
BasicEntanglerLayers-2	-0.0005 \pm 0.0004	0.6225 \pm 0.6225	4.0 \pm 0.0
BasicEntanglerLayers-3	-0.0002 \pm 0.0008	0.6224 \pm 0.6224	6.0 \pm 0.0
StronglyEntanglingLayers-3	-0.0001 \pm 0.0005	0.6224 \pm 0.6224	18.0 \pm 0.0
BasicEntanglerLayers-1	-0.0001 \pm 0.0001	0.6224 \pm 0.6224	2.0 \pm 0.0
SimplifiedTwoDesign-1	-0.0001 \pm 0.0001	0.6224 \pm 0.6224	4.0 \pm 0.0
StronglyEntanglingLayers-2	-0.0001 \pm 0.0001	0.6224 \pm 0.6224	12.0 \pm 0.0

Table B16 Results of the benchmark Function 15

Model	R^2 -score \pm std	RMSE \pm std	#Params \pm std
RF	0.9929 \pm 0.0013	0.0341 \pm 0.0341	40415.4 \pm 1084.41
DT	0.9861 \pm 0.0048	0.0479 \pm 0.0479	545.2 \pm 19.26
knn3	0.8694 \pm 0.0088	0.135 \pm 0.135	0.0 \pm 0.0
knn4	0.8606 \pm 0.0106	0.1377 \pm 0.1377	0.0 \pm 0.0
StronglyEntanglingLayers-60	0.8476 \pm 0.0048	0.1608 \pm 0.1608	360.0 \pm 0.0
knn2	0.8257 \pm 0.0066	0.1584 \pm 0.1584	0.0 \pm 0.0
BasicEntanglerLayers-60	0.8083 \pm 0.0268	0.18 \pm 0.18	120.0 \pm 0.0
SimplifiedTwoDesign-40	0.8045 \pm 0.0644	0.1798 \pm 0.1798	82.0 \pm 0.0
SimplifiedTwoDesign-60	0.8038 \pm 0.0775	0.1793 \pm 0.1793	122.0 \pm 0.0
SimplifiedTwoDesign-20	0.7988 \pm 0.0294	0.1843 \pm 0.1843	42.0 \pm 0.0
StronglyEntanglingLayers-40	0.7963 \pm 0.0109	0.1859 \pm 0.1859	240.0 \pm 0.0
BasicEntanglerLayers-40	0.7823 \pm 0.022	0.192 \pm 0.192	80.0 \pm 0.0
StronglyEntanglingLayers-20	0.7102 \pm 0.0349	0.2214 \pm 0.2214	120.0 \pm 0.0
BasicEntanglerLayers-20	0.6264 \pm 0.0716	0.2507 \pm 0.2507	40.0 \pm 0.0
RRQNN-120-2q	0.5784 \pm 0.0327	0.2673 \pm 0.2673	74.3 \pm 3.06
RRQNN-120-1q	0.5101 \pm 0.0311	0.2882 \pm 0.2882	70.4 \pm 3.31
SimplifiedTwoDesign-10	0.4561 \pm 0.0741	0.3031 \pm 0.3031	22.0 \pm 0.0
SimplifiedTwoDesign-9	0.3705 \pm 0.0623	0.3265 \pm 0.3265	20.0 \pm 0.0
BasicEntanglerLayers-10	0.3439 \pm 0.0736	0.3332 \pm 0.3332	20.0 \pm 0.0
SimplifiedTwoDesign-7	0.3012 \pm 0.0201	0.3443 \pm 0.3443	16.0 \pm 0.0
StronglyEntanglingLayers-10	0.2989 \pm 0.0174	0.3449 \pm 0.3449	60.0 \pm 0.0
BasicEntanglerLayers-9	0.2911 \pm 0.0314	0.3468 \pm 0.3468	18.0 \pm 0.0
StronglyEntanglingLayers-9	0.2769 \pm 0.0092	0.3503 \pm 0.3503	54.0 \pm 0.0
StronglyEntanglingLayers-7	0.264 \pm 0.0062	0.3534 \pm 0.3534	42.0 \pm 0.0
StronglyEntanglingLayers-6	0.2606 \pm 0.0034	0.3542 \pm 0.3542	36.0 \pm 0.0
StronglyEntanglingLayers-5	0.2529 \pm 0.0092	0.3561 \pm 0.3561	30.0 \pm 0.0
SimplifiedTwoDesign-6	0.2526 \pm 0.0061	0.3561 \pm 0.3561	14.0 \pm 0.0
SimplifiedTwoDesign-5	0.2454 \pm 0.0031	0.3579 \pm 0.3579	12.0 \pm 0.0
BasicEntanglerLayers-7	0.2452 \pm 0.0144	0.3579 \pm 0.3579	14.0 \pm 0.0
BasicEntanglerLayers-6	0.2331 \pm 0.0197	0.3608 \pm 0.3608	12.0 \pm 0.0
SimplifiedTwoDesign-4	0.233 \pm 0.0061	0.3608 \pm 0.3608	10.0 \pm 0.0
SimplifiedTwoDesign-3	0.206 \pm 0.046	0.3669 \pm 0.3669	8.0 \pm 0.0
BasicEntanglerLayers-4	0.18 \pm 0.0383	0.373 \pm 0.373	8.0 \pm 0.0
BasicEntanglerLayers-5	0.1698 \pm 0.0863	0.3749 \pm 0.3749	10.0 \pm 0.0
BasicEntanglerLayers-3	0.158 \pm 0.0254	0.378 \pm 0.378	6.0 \pm 0.0
RRQNN-60-1q	0.1312 \pm 0.0538	0.3838 \pm 0.3838	34.2 \pm 2.44
StronglyEntanglingLayers-3	0.0817 \pm 0.0006	0.3948 \pm 0.3948	18.0 \pm 0.0
RRQNN-60-2q	0.0104 \pm 0.0947	0.4094 \pm 0.4094	33.8 \pm 1.99
MLP100-100-1d	-inf \pm inf	0.424 \pm 0.424	10501.0 \pm 0.0
MLP500-1d	-inf \pm inf	0.4124 \pm 0.4124	2001.0 \pm 0.0
SVR-poly	-inf \pm inf	0.4398 \pm 0.4398	2540.8 \pm 69.14
SVR-linear	-inf \pm inf	0.4592 \pm 0.4592	2.0 \pm 0.0
MLP500-500-1d	-inf \pm inf	0.4159 \pm 0.4159	252501.0 \pm 0.0
MLP100-100-ReLU	-4.3603 \pm 0.327	0.3675 \pm 0.3675	10501.0 \pm 0.0
MLP100-1d	-30.7737 \pm 2.2589	0.4198 \pm 0.4198	401.0 \pm 0.0
MLP500-500-ReLU	-3.187 \pm 0.1907	0.3597 \pm 0.3597	252501.0 \pm 0.0
MLP100-ReLU	-21.9474 \pm 2.5968	0.3867 \pm 0.3867	401.0 \pm 0.0
SVR-RBF	-2.1458 \pm 0.1812	0.3615 \pm 0.3615	2001.0 \pm 15.5
StronglyEntanglingLayers-1	-15.0329 \pm 0.0	1.6495 \pm 1.6495	6.0 \pm 0.0
MLP500-ReLU	-10.5866 \pm 0.7134	0.3792 \pm 0.3792	2001.0 \pm 0.0
SimplifiedTwoDesign-2	-1.0341 \pm 0.5449	0.5814 \pm 0.5814	6.0 \pm 0.0
RRQNN-20-1q	-0.3672 \pm 0.0839	0.4815 \pm 0.4815	12.4 \pm 0.97
RRQNN-10-1q	-0.3653 \pm 0.2911	0.4788 \pm 0.4788	6.1 \pm 1.91
RRQNN-40-1q	-0.3019 \pm 0.0668	0.4699 \pm 0.4699	22.7 \pm 1.49
RRQNN-40-2d	-0.2814 \pm 0.058	0.4662 \pm 0.4662	24.9 \pm 2.02
RRQNN-20-2d	-0.2268 \pm 0.0936	0.456 \pm 0.456	13.0 \pm 1.25
BasicEntanglerLayers-2	-0.2167 \pm 0.6627	0.4447 \pm 0.4447	4.0 \pm 0.0
StronglyEntanglingLayers-4	-0.1799 \pm 0.1321	0.4469 \pm 0.4469	24.0 \pm 0.0
SVR-sigmoid	-0.0636 \pm 0.0139	75.9175 \pm 75.9175	3345.2 \pm 1.93
RRQNN-5-1q	-0.033 \pm 0.0998	0.4183 \pm 0.4183	3.7 \pm 0.67
StronglyEntanglingLayers-2	-0.0002 \pm 0.0003	0.412 \pm 0.412	12.0 \pm 0.0
SimplifiedTwoDesign-1	-0.0002 \pm 0.0003	0.412 \pm 0.412	4.0 \pm 0.0
BasicEntanglerLayers-1	-0.0002 \pm 0.0003	0.412 \pm 0.412	2.0 \pm 0.0

Table B17 Results of the benchmark Function 16

Model	R^2 -score \pm std	RMSE \pm std	#Params \pm std
RF	0.9992 \pm 0.0001	0.0099 \pm 0.0099	210822.0 \pm 66.59
knn4	0.9981 \pm 0.0001	0.0152 \pm 0.0152	0.0 \pm 0.0
knn3	0.998 \pm 0.0001	0.0158 \pm 0.0158	0.0 \pm 0.0
DT	0.9979 \pm 0.0001	0.0161 \pm 0.0161	3346.8 \pm 1.99
knn2	0.9973 \pm 0.0001	0.0185 \pm 0.0185	0.0 \pm 0.0
RRQNN-120-2q	0.9948 \pm 0.0006	0.0259 \pm 0.0259	86.6 \pm 2.95
StronglyEntanglingLayers-20	0.994 \pm 0.0014	0.0272 \pm 0.0272	120.0 \pm 0.0
RRQNN-60-2q	0.993 \pm 0.0008	0.0297 \pm 0.0297	45.1 \pm 3.03
RRQNN-40-2q	0.9921 \pm 0.001	0.0314 \pm 0.0314	29.2 \pm 1.75
StronglyEntanglingLayers-40	0.9916 \pm 0.0041	0.0318 \pm 0.0318	240.0 \pm 0.0
StronglyEntanglingLayers-10	0.9909 \pm 0.0012	0.0338 \pm 0.0338	60.0 \pm 0.0
MLP500-500-ReLU	0.9887 \pm 0.0015	0.0368 \pm 0.0368	252501.0 \pm 0.0
StronglyEntanglingLayers-9	0.9884 \pm 0.0043	0.0377 \pm 0.0377	54.0 \pm 0.0
RRQNN-60-1q	0.9882 \pm 0.0015	0.0383 \pm 0.0383	42.3 \pm 2.5
StronglyEntanglingLayers-60	0.9874 \pm 0.0063	0.0389 \pm 0.0389	360.0 \pm 0.0
SimplifiedTwoDesign-20	0.9872 \pm 0.0088	0.0383 \pm 0.0383	42.0 \pm 0.0
RRQNN-120-1q	0.9856 \pm 0.0036	0.0423 \pm 0.0423	80.4 \pm 4.55
StronglyEntanglingLayers-7	0.9848 \pm 0.0057	0.0432 \pm 0.0432	42.0 \pm 0.0
SimplifiedTwoDesign-10	0.9842 \pm 0.0058	0.044 \pm 0.044	22.0 \pm 0.0
RRQNN-60-1q	0.9842 \pm 0.0044	0.0444 \pm 0.0444	27.0 \pm 2.75
SVR-RBF	0.982 \pm 0.0005	0.0482 \pm 0.0482	37.2 \pm 3.68
SimplifiedTwoDesign-9	0.9795 \pm 0.0077	0.0502 \pm 0.0502	20.0 \pm 0.0
SimplifiedTwoDesign-7	0.9786 \pm 0.0101	0.0509 \pm 0.0509	16.0 \pm 0.0
RRQNN-20-2q	0.9786 \pm 0.0037	0.0518 \pm 0.0518	14.4 \pm 0.97
StronglyEntanglingLayers-6	0.9763 \pm 0.0078	0.0539 \pm 0.0539	36.0 \pm 0.0
RRQNN-20-1q	0.9754 \pm 0.0168	0.0538 \pm 0.0538	13.4 \pm 1.65
StronglyEntanglingLayers-5	0.9731 \pm 0.0079	0.0577 \pm 0.0577	30.0 \pm 0.0
SimplifiedTwoDesign-6	0.9701 \pm 0.0103	0.0607 \pm 0.0607	14.0 \pm 0.0
RRQNN-10-1q	0.9678 \pm 0.008	0.0634 \pm 0.0634	6.6 \pm 0.52
MLP100-100-ReLU	0.9647 \pm 0.0021	0.0641 \pm 0.0641	10501.0 \pm 0.0
SimplifiedTwoDesign-5	0.9527 \pm 0.0212	0.0756 \pm 0.0756	12.0 \pm 0.0
SimplifiedTwoDesign-4	0.9455 \pm 0.0146	0.0823 \pm 0.0823	10.0 \pm 0.0
BasicEntanglerLayers-10	0.9454 \pm 0.0096	0.0827 \pm 0.0827	20.0 \pm 0.0
BasicEntanglerLayers-20	0.9406 \pm 0.039	0.0834 \pm 0.0834	40.0 \pm 0.0
BasicEntanglerLayers-40	0.935 \pm 0.0233	0.0895 \pm 0.0895	80.0 \pm 0.0
StronglyEntanglingLayers-4	0.933 \pm 0.0103	0.0917 \pm 0.0917	24.0 \pm 0.0
BasicEntanglerLayers-9	0.9284 \pm 0.0285	0.0935 \pm 0.0935	18.0 \pm 0.0
SimplifiedTwoDesign-3	0.9205 \pm 0.0336	0.0983 \pm 0.0983	8.0 \pm 0.0
BasicEntanglerLayers-7	0.9023 \pm 0.0465	0.1087 \pm 0.1087	14.0 \pm 0.0
SimplifiedTwoDesign-40	0.9022 \pm 0.1	0.0961 \pm 0.0961	82.0 \pm 0.0
SVR-poly	0.8953 \pm 0.0012	0.1112 \pm 0.1112	1152.6 \pm 24.11
SimplifiedTwoDesign-60	0.8943 \pm 0.0569	0.1103 \pm 0.1103	122.0 \pm 0.0
BasicEntanglerLayers-6	0.8866 \pm 0.0437	0.1178 \pm 0.1178	12.0 \pm 0.0
BasicEntanglerLayers-60	0.8852 \pm 0.0462	0.118 \pm 0.118	120.0 \pm 0.0
BasicEntanglerLayers-5	0.8591 \pm 0.0627	0.1305 \pm 0.1305	10.0 \pm 0.0
RRQNN-5-1q	0.8585 \pm 0.0192	0.1334 \pm 0.1334	3.0 \pm 0.0
BasicEntanglerLayers-4	0.854 \pm 0.0465	0.1343 \pm 0.1343	8.0 \pm 0.0
MLP500-ReLU	0.8313 \pm 0.0114	0.1208 \pm 0.1208	2001.0 \pm 0.0
BasicEntanglerLayers-3	0.8264 \pm 0.0734	0.1457 \pm 0.1457	6.0 \pm 0.0
SimplifiedTwoDesign-2	0.7415 \pm 0.2337	0.1628 \pm 0.1628	6.0 \pm 0.0
StronglyEntanglingLayers-3	0.4872 \pm 0.0005	0.2544 \pm 0.2544	18.0 \pm 0.0
BasicEntanglerLayers-2	0.2692 \pm 0.0001	0.3036 \pm 0.3036	4.0 \pm 0.0
SVR-linear	0.1631 \pm 0.0329	0.2398 \pm 0.2398	2.0 \pm 0.0
MLP500-1d	0.1547 \pm 0.0647	0.2404 \pm 0.2404	2001.0 \pm 0.0
MLP100-100-1d	0.1526 \pm 0.0864	0.2427 \pm 0.2427	10501.0 \pm 0.0
MLP500-500-1d	0.1427 \pm 0.0598	0.2417 \pm 0.2417	252501.0 \pm 0.0
MLP100-ReLU	0.0345 \pm 0.023	0.2128 \pm 0.2128	401.0 \pm 0.0
StronglyEntanglingLayers-1	-13.3279 \pm 0.0	1.3444 \pm 1.3444	6.0 \pm 0.0
MLP100-1d	-1.0527 \pm 0.0718	0.2551 \pm 0.2551	401.0 \pm 0.0
SVR-sigmoid	-0.0671 \pm 0.0138	76.049 \pm 76.049	3346.2 \pm 3.05
BasicEntanglerLayers-1	-0.0001 \pm 0.0002	0.3552 \pm 0.3552	2.0 \pm 0.0
SimplifiedTwoDesign-1	-0.0001 \pm 0.0002	0.3552 \pm 0.3552	4.0 \pm 0.0
StronglyEntanglingLayers-2	-0.0001 \pm 0.0002	0.3552 \pm 0.3552	12.0 \pm 0.0

Table B18 Results of the benchmark Function 17

Model	R^2 -score \pm std	RMSE \pm std	#Params \pm std
RF	0.9982 \pm 0.0001	0.0159 \pm 0.0159	210829.8 \pm 52.5
knn4	0.9962 \pm 0.0002	0.0233 \pm 0.0233	0.0 \pm 0.0
knn3	0.996 \pm 0.0002	0.0238 \pm 0.0238	0.0 \pm 0.0
DT	0.9957 \pm 0.0003	0.025 \pm 0.025	3346.4 \pm 2.5
knn2	0.9948 \pm 0.0001	0.0275 \pm 0.0275	0.0 \pm 0.0
StronglyEntanglingLayers-20	0.9906 \pm 0.0012	0.0371 \pm 0.0371	120.0 \pm 0.0
StronglyEntanglingLayers-40	0.99 \pm 0.0033	0.0378 \pm 0.0378	240.0 \pm 0.0
RRQNN-120-2q	0.9893 \pm 0.0012	0.0396 \pm 0.0396	83.1 \pm 3.03
StronglyEntanglingLayers-60	0.9872 \pm 0.006	0.0424 \pm 0.0424	360.0 \pm 0.0
RRQNN-60-2q	0.9807 \pm 0.0028	0.0529 \pm 0.0529	41.9 \pm 1.85
RRQNN-120-1q	0.9771 \pm 0.0032	0.0577 \pm 0.0577	74.3 \pm 4.62
StronglyEntanglingLayers-10	0.9758 \pm 0.0052	0.0592 \pm 0.0592	60.0 \pm 0.0
StronglyEntanglingLayers-9	0.9738 \pm 0.0045	0.0618 \pm 0.0618	54.0 \pm 0.0
SVR-RBF	0.9706 \pm 0.0004	0.0656 \pm 0.0656	279.4 \pm 13.53
RRQNN-40-2q	0.9689 \pm 0.0036	0.0673 \pm 0.0673	26.8 \pm 1.03
RRQNN-60-1q	0.9663 \pm 0.0032	0.0701 \pm 0.0701	40.6 \pm 3.17
MLP500-500-ReLU	0.9623 \pm 0.0027	0.0723 \pm 0.0723	252501.0 \pm 0.0
StronglyEntanglingLayers-7	0.9612 \pm 0.0062	0.0751 \pm 0.0751	42.0 \pm 0.0
RRQNN-40-1q	0.9599 \pm 0.0041	0.0765 \pm 0.0765	26.6 \pm 2.8
BasicEntanglerLayers-20	0.9515 \pm 0.0063	0.0841 \pm 0.0841	40.0 \pm 0.0
BasicEntanglerLayers-40	0.9487 \pm 0.0117	0.0861 \pm 0.0861	80.0 \pm 0.0
StronglyEntanglingLayers-6	0.9464 \pm 0.0083	0.0883 \pm 0.0883	36.0 \pm 0.0
MLP100-100-ReLU	0.9434 \pm 0.0037	0.0859 \pm 0.0859	10501.0 \pm 0.0
RRQNN-20-2q	0.9413 \pm 0.0037	0.0926 \pm 0.0926	14.0 \pm 0.94
RRQNN-20-1q	0.9269 \pm 0.0186	0.1027 \pm 0.1027	14.0 \pm 0.82
BasicEntanglerLayers-60	0.9258 \pm 0.038	0.1019 \pm 0.1019	120.0 \pm 0.0
StronglyEntanglingLayers-5	0.9224 \pm 0.0232	0.1056 \pm 0.1056	30.0 \pm 0.0
RRQNN-10-1q	0.9014 \pm 0.0189	0.1196 \pm 0.1196	6.8 \pm 0.42
BasicEntanglerLayers-9	0.9011 \pm 0.0177	0.1199 \pm 0.1199	18.0 \pm 0.0
BasicEntanglerLayers-10	0.8922 \pm 0.0239	0.1249 \pm 0.1249	20.0 \pm 0.0
BasicEntanglerLayers-7	0.8738 \pm 0.0177	0.1357 \pm 0.1357	14.0 \pm 0.0
SimplifiedTwoDesign-20	0.8725 \pm 0.0202	0.1363 \pm 0.1363	42.0 \pm 0.0
StronglyEntanglingLayers-4	0.8666 \pm 0.0199	0.1394 \pm 0.1394	24.0 \pm 0.0
SimplifiedTwoDesign-10	0.8615 \pm 0.0074	0.1424 \pm 0.1424	22.0 \pm 0.0
SimplifiedTwoDesign-9	0.8567 \pm 0.0133	0.1447 \pm 0.1447	20.0 \pm 0.0
BasicEntanglerLayers-6	0.8566 \pm 0.0265	0.1445 \pm 0.1445	12.0 \pm 0.0
SimplifiedTwoDesign-40	0.8496 \pm 0.0415	0.1474 \pm 0.1474	82.0 \pm 0.0
SimplifiedTwoDesign-6	0.8353 \pm 0.0194	0.155 \pm 0.155	14.0 \pm 0.0
BasicEntanglerLayers-5	0.8214 \pm 0.0511	0.1603 \pm 0.1603	10.0 \pm 0.0
SimplifiedTwoDesign-7	0.8211 \pm 0.0381	0.1611 \pm 0.1611	16.0 \pm 0.0
SimplifiedTwoDesign-5	0.7973 \pm 0.0331	0.1718 \pm 0.1718	12.0 \pm 0.0
SimplifiedTwoDesign-60	0.7881 \pm 0.0512	0.1749 \pm 0.1749	122.0 \pm 0.0
SVR-poly	0.7807 \pm 0.0019	0.1649 \pm 0.1649	1710.0 \pm 18.67
SimplifiedTwoDesign-3	0.7781 \pm 0.0353	0.1798 \pm 0.1798	8.0 \pm 0.0
SimplifiedTwoDesign-4	0.7768 \pm 0.0331	0.1804 \pm 0.1804	10.0 \pm 0.0
BasicEntanglerLayers-4	0.7752 \pm 0.0325	0.181 \pm 0.181	8.0 \pm 0.0
MLP500-ReLU	0.7646 \pm 0.0066	0.1475 \pm 0.1475	2001.0 \pm 0.0
RRQNN-5-1q	0.7367 \pm 0.0284	0.1961 \pm 0.1961	3.0 \pm 0.0
SimplifiedTwoDesign-2	0.6778 \pm 0.1634	0.2131 \pm 0.2131	6.0 \pm 0.0
BasicEntanglerLayers-3	0.6572 \pm 0.071	0.2232 \pm 0.2232	6.0 \pm 0.0
StronglyEntanglingLayers-3	0.4267 \pm 0.0006	0.2897 \pm 0.2897	18.0 \pm 0.0
BasicEntanglerLayers-2	0.1247 \pm 0.0003	0.358 \pm 0.358	4.0 \pm 0.0
MLP100-1d	-8.9433 \pm 0.7556	0.3424 \pm 0.3424	401.0 \pm 0.0
MLP500-1d	-2.1398 \pm 0.7623	0.3348 \pm 0.3348	2001.0 \pm 0.0
SVR-linear	-2.0909 \pm 0.0988	0.3382 \pm 0.3382	2.0 \pm 0.0
MLP500-500-1d	-2.0752 \pm 0.4734	0.3333 \pm 0.3333	252501.0 \pm 0.0
StronglyEntanglingLayers-1	-12.6286 \pm 0.0	1.4127 \pm 1.4127	6.0 \pm 0.0
MLP100-ReLU	-1.8903 \pm 0.1	0.2627 \pm 0.2627	401.0 \pm 0.0
MLP100-100-1d	-1.8496 \pm 0.4923	0.3376 \pm 0.3376	10501.0 \pm 0.0
SVR-sigmoid	-0.0653 \pm 0.0141	75.9855 \pm 75.9855	3344.2 \pm 3.05
StronglyEntanglingLayers-2	-0.0001 \pm 0.0001	0.3827 \pm 0.3827	12.0 \pm 0.0
SimplifiedTwoDesign-1	-0.0001 \pm 0.0001	0.3827 \pm 0.3827	4.0 \pm 0.0
BasicEntanglerLayers-1	-0.0001 \pm 0.0001	0.3827 \pm 0.3827	2.0 \pm 0.0

Table B19 Results of the benchmark Function 18

Model	R^2 -score \pm std	RMSE \pm std	#Params \pm std
RF	0.9998 \pm 0.0	0.0074 \pm 0.0074	206308.8 \pm 279.84
DT	0.9996 \pm 0.0	0.0106 \pm 0.0106	3250.8 \pm 8.02
StronglyEntanglingLayers-40	0.9975 \pm 0.0008	0.026 \pm 0.026	240.0 \pm 0.0
knn4	0.9975 \pm 0.0002	0.0262 \pm 0.0262	0.0 \pm 0.0
knn3	0.9973 \pm 0.0001	0.0269 \pm 0.0269	0.0 \pm 0.0
StronglyEntanglingLayers-20	0.9969 \pm 0.0006	0.0292 \pm 0.0292	120.0 \pm 0.0
StronglyEntanglingLayers-60	0.9966 \pm 0.0009	0.0302 \pm 0.0302	360.0 \pm 0.0
MLP500-500-ReLU	0.9964 \pm 0.001	0.0312 \pm 0.0312	252501.0 \pm 0.0
knn2	0.9964 \pm 0.0002	0.0315 \pm 0.0315	0.0 \pm 0.0
SimplifiedTwoDesign-20	0.9959 \pm 0.0025	0.0326 \pm 0.0326	42.0 \pm 0.0
RRQNN-120-2q	0.9959 \pm 0.001	0.0336 \pm 0.0336	84.3 \pm 3.5
RRQNN-60-1q	0.9941 \pm 0.002	0.0401 \pm 0.0401	43.8 \pm 2.3
RRQNN-40-1q	0.9939 \pm 0.0015	0.0408 \pm 0.0408	28.5 \pm 2.59
RRQNN-60-2q	0.9937 \pm 0.0021	0.0416 \pm 0.0416	44.4 \pm 2.17
RRQNN-120-1q	0.9935 \pm 0.0041	0.0412 \pm 0.0412	79.2 \pm 3.77
StronglyEntanglingLayers-10	0.993 \pm 0.0019	0.0437 \pm 0.0437	60.0 \pm 0.0
StronglyEntanglingLayers-9	0.9908 \pm 0.0038	0.0496 \pm 0.0496	54.0 \pm 0.0
BasicEntanglerLayers-20	0.9903 \pm 0.0037	0.051 \pm 0.051	40.0 \pm 0.0
RRQNN-40-2q	0.9901 \pm 0.0032	0.0518 \pm 0.0518	29.2 \pm 0.79
SimplifiedTwoDesign-10	0.99 \pm 0.0041	0.0516 \pm 0.0516	22.0 \pm 0.0
SVR-RBF	0.9895 \pm 0.0002	0.054 \pm 0.054	60.0 \pm 2.31
SimplifiedTwoDesign-40	0.9891 \pm 0.0126	0.0486 \pm 0.0486	82.0 \pm 0.0
StronglyEntanglingLayers-7	0.9874 \pm 0.0063	0.0575 \pm 0.0575	42.0 \pm 0.0
RRQNN-20-1q	0.9867 \pm 0.0073	0.0586 \pm 0.0586	13.7 \pm 0.48
SimplifiedTwoDesign-9	0.9848 \pm 0.0043	0.0643 \pm 0.0643	20.0 \pm 0.0
BasicEntanglerLayers-40	0.9829 \pm 0.0104	0.0662 \pm 0.0662	80.0 \pm 0.0
BasicEntanglerLayers-10	0.9809 \pm 0.004	0.0723 \pm 0.0723	20.0 \pm 0.0
SimplifiedTwoDesign-6	0.9803 \pm 0.003	0.0737 \pm 0.0737	14.0 \pm 0.0
SimplifiedTwoDesign-7	0.9802 \pm 0.007	0.073 \pm 0.073	16.0 \pm 0.0
RRQNN-20-2q	0.9784 \pm 0.0082	0.0762 \pm 0.0762	14.0 \pm 0.94
BasicEntanglerLayers-9	0.9759 \pm 0.0087	0.0807 \pm 0.0807	18.0 \pm 0.0
BasicEntanglerLayers-60	0.9752 \pm 0.0115	0.0805 \pm 0.0805	120.0 \pm 0.0
StronglyEntanglingLayers-6	0.971 \pm 0.0089	0.0886 \pm 0.0886	36.0 \pm 0.0
MLP100-100-ReLU	0.9706 \pm 0.0052	0.0846 \pm 0.0846	10501.0 \pm 0.0
SimplifiedTwoDesign-60	0.9654 \pm 0.0244	0.0911 \pm 0.0911	122.0 \pm 0.0
StronglyEntanglingLayers-5	0.9647 \pm 0.0057	0.0986 \pm 0.0986	30.0 \pm 0.0
SimplifiedTwoDesign-5	0.9635 \pm 0.026	0.0962 \pm 0.0962	12.0 \pm 0.0
BasicEntanglerLayers-7	0.9617 \pm 0.0129	0.1016 \pm 0.1016	14.0 \pm 0.0
RRQNN-10-1q	0.9535 \pm 0.0221	0.111 \pm 0.111	5.6 \pm 0.52
BasicEntanglerLayers-6	0.9463 \pm 0.0192	0.1204 \pm 0.1204	12.0 \pm 0.0
BasicEntanglerLayers-5	0.9229 \pm 0.0359	0.1424 \pm 0.1424	10.0 \pm 0.0
BasicEntanglerLayers-3	0.8958 \pm 0.0078	0.1697 \pm 0.1697	6.0 \pm 0.0
BasicEntanglerLayers-4	0.8928 \pm 0.0084	0.1721 \pm 0.1721	8.0 \pm 0.0
SimplifiedTwoDesign-4	0.8883 \pm 0.0797	0.1697 \pm 0.1697	10.0 \pm 0.0
SimplifiedTwoDesign-3	0.8098 \pm 0.2732	0.2042 \pm 0.2042	8.0 \pm 0.0
StronglyEntanglingLayers-4	0.7358 \pm 0.0102	0.2704 \pm 0.2704	24.0 \pm 0.0
RRQNN-5-1q	0.6312 \pm 0.1337	0.3152 \pm 0.3152	1.9 \pm 0.99
MLP500-ReLU	0.5853 \pm 0.0219	0.2399 \pm 0.2399	2001.0 \pm 0.0
SimplifiedTwoDesign-2	0.2962 \pm 0.2557	0.435 \pm 0.435	6.0 \pm 0.0
StronglyEntanglingLayers-3	0.0328 \pm 0.0004	0.5174 \pm 0.5174	18.0 \pm 0.0
MLP500-500-1d	-inf \pm inf	0.5289 \pm 0.5289	252501.0 \pm 0.0
SVR-linear	-inf \pm inf	0.5434 \pm 0.5434	2.0 \pm 0.0
MLP100-1d	-inf \pm inf	0.5266 \pm 0.5266	401.0 \pm 0.0
MLP100-100-1d	-inf \pm inf	0.5313 \pm 0.5313	10501.0 \pm 0.0
MLP500-1d	-inf \pm inf	0.5278 \pm 0.5278	2001.0 \pm 0.0
StronglyEntanglingLayers-1	-5.6605 \pm 0.0	1.3578 \pm 1.3578	6.0 \pm 0.0
MLP100-ReLU	-2.0448 \pm 0.0571	0.3919 \pm 0.3919	401.0 \pm 0.0
SVR-poly	-0.4032 \pm 0.0242	0.4461 \pm 0.4461	2589.0 \pm 28.93
SVR-sigmoid	-0.059 \pm 0.014	75.7652 \pm 75.7652	3347.0 \pm 1.41
BasicEntanglerLayers-2	-0.0003 \pm 0.0002	0.5262 \pm 0.5262	4.0 \pm 0.0
StronglyEntanglingLayers-2	-0.0001 \pm 0.0001	0.5261 \pm 0.5261	12.0 \pm 0.0
SimplifiedTwoDesign-1	-0.0001 \pm 0.0001	0.5261 \pm 0.5261	4.0 \pm 0.0
BasicEntanglerLayers-1	-0.0001 \pm 0.0001	0.5261 \pm 0.5261	2.0 \pm 0.0

Table B20 Results of the benchmark Function 19

Model	R^2 -score \pm std	RMSE \pm std	#Params \pm std
RF	0.9981 \pm 0.0004	0.0127 \pm 0.0127	211067.8 \pm 25.98
StronglyEntanglingLayers-40	0.9965 \pm 0.0015	0.0176 \pm 0.0176	240.0 \pm 0.0
knn3	0.9963 \pm 0.0006	0.0181 \pm 0.0181	0.0 \pm 0.0
knn4	0.9961 \pm 0.0008	0.0185 \pm 0.0185	0.0 \pm 0.0
DT	0.9959 \pm 0.0003	0.0194 \pm 0.0194	3348.2 \pm 1.03
StronglyEntanglingLayers-20	0.9956 \pm 0.0012	0.0199 \pm 0.0199	120.0 \pm 0.0
RRQNN-120-1q	0.9954 \pm 0.0023	0.0199 \pm 0.0199	80.0 \pm 3.56
StronglyEntanglingLayers-60	0.9953 \pm 0.0059	0.0189 \pm 0.0189	360.0 \pm 0.0
knn2	0.9953 \pm 0.0005	0.0206 \pm 0.0206	0.0 \pm 0.0
RRQNN-120-2q	0.9948 \pm 0.0016	0.0218 \pm 0.0218	84.7 \pm 5.42
RRQNN-60-1q	0.9941 \pm 0.0017	0.0232 \pm 0.0232	39.8 \pm 2.74
RRQNN-40-1q	0.992 \pm 0.0031	0.0268 \pm 0.0268	25.5 \pm 3.14
RRQNN-60-2q	0.9907 \pm 0.0021	0.0289 \pm 0.0289	41.6 \pm 2.67
StronglyEntanglingLayers-10	0.9888 \pm 0.0033	0.0316 \pm 0.0316	60.0 \pm 0.0
RRQNN-40-2q	0.987 \pm 0.0026	0.0345 \pm 0.0345	27.9 \pm 1.73
RRQNN-20-1q	0.9843 \pm 0.0028	0.0377 \pm 0.0377	12.9 \pm 1.2
StronglyEntanglingLayers-9	0.9837 \pm 0.0056	0.0381 \pm 0.0381	54.0 \pm 0.0
StronglyEntanglingLayers-7	0.9729 \pm 0.0117	0.0488 \pm 0.0488	42.0 \pm 0.0
SVR-RBF	0.9515 \pm 0.0003	0.0658 \pm 0.0658	68.4 \pm 3.63
StronglyEntanglingLayers-6	0.9496 \pm 0.0241	0.0663 \pm 0.0663	36.0 \pm 0.0
RRQNN-20-2q	0.9356 \pm 0.0369	0.0747 \pm 0.0747	14.4 \pm 1.07
RRQNN-10-1q	0.9251 \pm 0.0329	0.0808 \pm 0.0808	5.6 \pm 0.7
StronglyEntanglingLayers-5	0.8786 \pm 0.0455	0.1032 \pm 0.1032	30.0 \pm 0.0
MLP500-500-ReLU	0.871 \pm 0.0157	0.096 \pm 0.096	252501.0 \pm 0.0
BasicEntanglerLayers-60	0.7833 \pm 0.0327	0.1404 \pm 0.1404	120.0 \pm 0.0
BasicEntanglerLayers-40	0.7798 \pm 0.0264	0.1416 \pm 0.1416	80.0 \pm 0.0
StronglyEntanglingLayers-4	0.7604 \pm 0.0096	0.1479 \pm 0.1479	24.0 \pm 0.0
BasicEntanglerLayers-20	0.7381 \pm 0.0229	0.1546 \pm 0.1546	40.0 \pm 0.0
MLP100-100-ReLU	0.7061 \pm 0.015	0.1335 \pm 0.1335	10501.0 \pm 0.0
RRQNN-5-1q	0.6213 \pm 0.2314	0.1807 \pm 0.1807	2.2 \pm 0.63
BasicEntanglerLayers-10	0.5887 \pm 0.0507	0.1935 \pm 0.1935	20.0 \pm 0.0
BasicEntanglerLayers-9	0.5826 \pm 0.0413	0.1951 \pm 0.1951	18.0 \pm 0.0
BasicEntanglerLayers-7	0.5289 \pm 0.048	0.2072 \pm 0.2072	14.0 \pm 0.0
BasicEntanglerLayers-6	0.4597 \pm 0.0653	0.2218 \pm 0.2218	12.0 \pm 0.0
BasicEntanglerLayers-5	0.4371 \pm 0.0581	0.2265 \pm 0.2265	10.0 \pm 0.0
SimplifiedTwoDesign-20	0.4289 \pm 0.0088	0.2284 \pm 0.2284	42.0 \pm 0.0
SimplifiedTwoDesign-10	0.421 \pm 0.0046	0.23 \pm 0.23	22.0 \pm 0.0
SimplifiedTwoDesign-9	0.4194 \pm 0.011	0.2303 \pm 0.2303	20.0 \pm 0.0
SimplifiedTwoDesign-7	0.4003 \pm 0.0201	0.234 \pm 0.234	16.0 \pm 0.0
BasicEntanglerLayers-3	0.3893 \pm 0.0062	0.2362 \pm 0.2362	6.0 \pm 0.0
SimplifiedTwoDesign-6	0.3575 \pm 0.0375	0.2422 \pm 0.2422	14.0 \pm 0.0
SimplifiedTwoDesign-5	0.3235 \pm 0.0496	0.2484 \pm 0.2484	12.0 \pm 0.0
SimplifiedTwoDesign-40	0.3144 \pm 0.1263	0.2494 \pm 0.2494	82.0 \pm 0.0
BasicEntanglerLayers-4	0.3075 \pm 0.0922	0.251 \pm 0.251	8.0 \pm 0.0
SimplifiedTwoDesign-4	0.2777 \pm 0.0131	0.2569 \pm 0.2569	10.0 \pm 0.0
SimplifiedTwoDesign-3	0.2635 \pm 0.0287	0.2593 \pm 0.2593	8.0 \pm 0.0
SimplifiedTwoDesign-60	0.2365 \pm 0.1772	0.2625 \pm 0.2625	122.0 \pm 0.0
StronglyEntanglingLayers-3	0.0588 \pm 0.0017	0.2933 \pm 0.2932	18.0 \pm 0.0
SVR-linear	-inf \pm inf	0.3088 \pm 0.3088	2.0 \pm 0.0
MLP100-100-1d	-inf \pm inf	0.3057 \pm 0.3057	10501.0 \pm 0.0
MLP500-500-1d	-inf \pm inf	0.3037 \pm 0.3037	252501.0 \pm 0.0
MLP500-1d	-inf \pm inf	0.303 \pm 0.303	2001.0 \pm 0.0
SVR-poly	-7.6729 \pm 0.8861	0.2785 \pm 0.2785	1416.2 \pm 33.1
MLP100-1d	-5.7086 \pm 0.5095	0.3307 \pm 0.3307	401.0 \pm 0.0
StronglyEntanglingLayers-1	-36.4897 \pm 0.0	1.8507 \pm 1.8507	6.0 \pm 0.0
MLP100-ReLU	-1.9414 \pm 0.1276	0.2834 \pm 0.2834	401.0 \pm 0.0
SimplifiedTwoDesign-2	-1.0527 \pm 1.1087	0.4175 \pm 0.4175	6.0 \pm 0.0
BasicEntanglerLayers-2	-0.7469 \pm 2.3605	0.36 \pm 0.36	4.0 \pm 0.0
MLP500-ReLU	-0.4175 \pm 0.0646	0.2067 \pm 0.2067	2001.0 \pm 0.0
SVR-sigmoid	-0.0626 \pm 0.014	75.897 \pm 75.897	3347.8 \pm 1.75
StronglyEntanglingLayers-2	-0.0001 \pm 0.0001	0.3023 \pm 0.3023	12.0 \pm 0.0
SimplifiedTwoDesign-1	-0.0001 \pm 0.0001	0.3023 \pm 0.3023	4.0 \pm 0.0
BasicEntanglerLayers-1	-0.0001 \pm 0.0001	0.3023 \pm 0.3023	2.0 \pm 0.0

Table B21 Results of the benchmark Function 20

Model	R^2 -score \pm std	RMSE \pm std	#Params \pm std
RF	0.998 \pm 0.0002	0.0209 \pm 0.0209	211172.0 \pm 0.0
DT	0.9979 \pm 0.0002	0.0217 \pm 0.0217	3349.0 \pm 0.0
StronglyEntanglingLayers-60	0.9912 \pm 0.0013	0.0439 \pm 0.0439	360.0 \pm 0.0
StronglyEntanglingLayers-40	0.9891 \pm 0.0014	0.049 \pm 0.049	240.0 \pm 0.0
SimplifiedTwoDesign-20	0.983 \pm 0.0036	0.061 \pm 0.061	42.0 \pm 0.0
knn4	0.9761 \pm 0.0016	0.0698 \pm 0.0698	0.0 \pm 0.0
knn3	0.9759 \pm 0.0005	0.0708 \pm 0.0708	0.0 \pm 0.0
knn2	0.9687 \pm 0.0009	0.0818 \pm 0.0818	0.0 \pm 0.0
StronglyEntanglingLayers-20	0.9552 \pm 0.0134	0.0983 \pm 0.0983	120.0 \pm 0.0
BasicEntanglerLayers-60	0.9521 \pm 0.0115	0.1022 \pm 0.1022	120.0 \pm 0.0
SimplifiedTwoDesign-40	0.952 \pm 0.0348	0.0981 \pm 0.0981	82.0 \pm 0.0
BasicEntanglerLayers-40	0.9492 \pm 0.0104	0.1054 \pm 0.1054	80.0 \pm 0.0
SimplifiedTwoDesign-60	0.9336 \pm 0.0313	0.1181 \pm 0.1181	122.0 \pm 0.0
RRQNN-120-2q	0.9282 \pm 0.016	0.1251 \pm 0.1251	77.0 \pm 2.4
RRQNN-120-1q	0.9195 \pm 0.0196	0.1322 \pm 0.1322	74.8 \pm 2.53
BasicEntanglerLayers-20	0.875 \pm 0.0395	0.1641 \pm 0.1641	40.0 \pm 0.0
RRQNN-60-1q	0.6856 \pm 0.0951	0.2607 \pm 0.2607	36.9 \pm 2.85
SimplifiedTwoDesign-10	0.6843 \pm 0.0485	0.2632 \pm 0.2632	22.0 \pm 0.0
SimplifiedTwoDesign-9	0.6664 \pm 0.0484	0.2706 \pm 0.2706	20.0 \pm 0.0
RRQNN-60-2q	0.6487 \pm 0.063	0.2775 \pm 0.2775	36.6 \pm 3.17
StronglyEntanglingLayers-10	0.6328 \pm 0.0382	0.2843 \pm 0.2843	60.0 \pm 0.0
StronglyEntanglingLayers-9	0.6163 \pm 0.0304	0.2908 \pm 0.2908	54.0 \pm 0.0
BasicEntanglerLayers-10	0.6117 \pm 0.0644	0.2917 \pm 0.2917	20.0 \pm 0.0
StronglyEntanglingLayers-7	0.5746 \pm 0.0188	0.3063 \pm 0.3063	42.0 \pm 0.0
BasicEntanglerLayers-9	0.5707 \pm 0.0484	0.3073 \pm 0.3073	18.0 \pm 0.0
SimplifiedTwoDesign-7	0.5667 \pm 0.0137	0.3092 \pm 0.3092	16.0 \pm 0.0
SimplifiedTwoDesign-6	0.5613 \pm 0.0191	0.3111 \pm 0.3111	14.0 \pm 0.0
SimplifiedTwoDesign-5	0.5443 \pm 0.0127	0.3171 \pm 0.3171	12.0 \pm 0.0
RRQNN-40-1q	0.5388 \pm 0.0376	0.3188 \pm 0.3188	25.3 \pm 1.89
StronglyEntanglingLayers-6	0.5388 \pm 0.0097	0.319 \pm 0.319	36.0 \pm 0.0
StronglyEntanglingLayers-5	0.5347 \pm 0.0207	0.3204 \pm 0.3204	30.0 \pm 0.0
BasicEntanglerLayers-7	0.5324 \pm 0.0326	0.321 \pm 0.321	14.0 \pm 0.0
SimplifiedTwoDesign-3	0.528 \pm 0.004	0.3227 \pm 0.3227	8.0 \pm 0.0
BasicEntanglerLayers-6	0.5241 \pm 0.0194	0.324 \pm 0.324	12.0 \pm 0.0
RRQNN-40-2q	0.5121 \pm 0.0294	0.3279 \pm 0.3279	23.2 \pm 1.81
BasicEntanglerLayers-5	0.5101 \pm 0.0083	0.3288 \pm 0.3288	10.0 \pm 0.0
SimplifiedTwoDesign-4	0.5083 \pm 0.0725	0.3287 \pm 0.3287	10.0 \pm 0.0
RRQNN-20-2q	0.4773 \pm 0.0384	0.3394 \pm 0.3394	14.1 \pm 1.79
BasicEntanglerLayers-3	0.4607 \pm 0.0003	0.345 \pm 0.345	6.0 \pm 0.0
RRQNN-10-1q	0.4589 \pm 0.0479	0.3453 \pm 0.3453	5.1 \pm 0.57
RRQNN-20-1q	0.4574 \pm 0.0353	0.3459 \pm 0.3459	13.7 \pm 1.34
BasicEntanglerLayers-4	0.4534 \pm 0.1026	0.3461 \pm 0.3461	8.0 \pm 0.0
StronglyEntanglingLayers-3	0.4457 \pm 0.0024	0.3497 \pm 0.3497	18.0 \pm 0.0
StronglyEntanglingLayers-4	0.4412 \pm 0.0671	0.3506 \pm 0.3506	24.0 \pm 0.0
RRQNN-5-1q	0.3077 \pm 0.0649	0.3905 \pm 0.3905	2.2 \pm 0.92
SimplifiedTwoDesign-2	0.213 \pm 0.1424	0.4153 \pm 0.4153	6.0 \pm 0.0
MLP500-500-ReLU	0.0999 \pm 0.0543	0.3166 \pm 0.3166	252501.0 \pm 0.0
SVR-RBF	0.0684 \pm 0.0963	0.3084 \pm 0.3084	1864.0 \pm 45.15
SVR-linear	-inf \pm inf	0.4917 \pm 0.4917	2.0 \pm 0.0
MLP100-100-Id	-inf \pm inf	0.4713 \pm 0.4713	10501.0 \pm 0.0
MLP500-500-Id	-inf \pm inf	0.4738 \pm 0.4738	252501.0 \pm 0.0
MLP500-Id	-inf \pm inf	0.4695 \pm 0.4695	2001.0 \pm 0.0
MLP100-ReLU	-7.388 \pm 1.0141	0.4414 \pm 0.4414	401.0 \pm 0.0
SVR-poly	-4.9575 \pm 0.5369	0.4583 \pm 0.4583	2582.4 \pm 14.07
MLP100-Id	-34.1345 \pm 4.6982	0.4698 \pm 0.4698	401.0 \pm 0.0
StronglyEntanglingLayers-1	-10.0324 \pm 0.0	1.5604 \pm 1.5604	6.0 \pm 0.0
MLP500-ReLU	-1.6165 \pm 0.1583	0.3647 \pm 0.3647	2001.0 \pm 0.0
SVR-sigmoid	-0.0594 \pm 0.014	75.7758 \pm 75.7758	3346.8 \pm 2.7
MLP100-100-ReLU	-0.0549 \pm 0.0522	0.3257 \pm 0.3257	10501.0 \pm 0.0
BasicEntanglerLayers-2	-0.0003 \pm 0.0004	0.4698 \pm 0.4698	4.0 \pm 0.0
StronglyEntanglingLayers-2	-0.0001 \pm 0.0002	0.4698 \pm 0.4698	12.0 \pm 0.0
BasicEntanglerLayers-1	-0.0001 \pm 0.0002	0.4698 \pm 0.4698	2.0 \pm 0.0
SimplifiedTwoDesign-1	-0.0001 \pm 0.0002	0.4698 \pm 0.4698	4.0 \pm 0.0

Table B22 Results of the benchmark Function 21

Model	R^2 -score \pm std	RMSE \pm std	#Params \pm std
RF	1.0 \pm 0.0	0.0 \pm 0.0	207287.8 \pm 559.86
DT	1.0 \pm 0.0	0.0 \pm 0.0	3273.2 \pm 10.35
StronglyEntanglingLayers-60	0.9948 \pm 0.0011	0.0414 \pm 0.0414	360.0 \pm 0.0
StronglyEntanglingLayers-40	0.9944 \pm 0.0009	0.0431 \pm 0.0431	240.0 \pm 0.0
knn3	0.9936 \pm 0.0007	0.0452 \pm 0.0452	0.0 \pm 0.0
knn4	0.9934 \pm 0.0009	0.0457 \pm 0.0457	0.0 \pm 0.0
SimplifiedTwoDesign-20	0.9924 \pm 0.0029	0.0493 \pm 0.0493	42.0 \pm 0.0
knn2	0.9922 \pm 0.0005	0.0504 \pm 0.0504	0.0 \pm 0.0
StronglyEntanglingLayers-20	0.9888 \pm 0.0018	0.0609 \pm 0.0609	120.0 \pm 0.0
RRQNN-120-1q	0.9886 \pm 0.002	0.0615 \pm 0.0615	77.8 \pm 4.29
SVR-RBF	0.9871 \pm 0.0002	0.068 \pm 0.068	253.8 \pm 4.57
SimplifiedTwoDesign-40	0.986 \pm 0.0231	0.0568 \pm 0.0568	82.0 \pm 0.0
RRQNN-120-2q	0.9841 \pm 0.0019	0.0722 \pm 0.0722	81.4 \pm 3.86
RRQNN-60-1q	0.9839 \pm 0.0038	0.0727 \pm 0.0727	38.3 \pm 2.36
RRQNN-40-1q	0.9837 \pm 0.0065	0.0719 \pm 0.0719	27.8 \pm 1.99
BasicEntanglerLayers-40	0.9808 \pm 0.007	0.0786 \pm 0.0786	80.0 \pm 0.0
BasicEntanglerLayers-60	0.9794 \pm 0.012	0.0804 \pm 0.0804	120.0 \pm 0.0
BasicEntanglerLayers-20	0.9763 \pm 0.0122	0.0858 \pm 0.0858	40.0 \pm 0.0
RRQNN-60-2q	0.9745 \pm 0.007	0.0913 \pm 0.0913	42.6 \pm 3.37
SimplifiedTwoDesign-10	0.973 \pm 0.0092	0.0936 \pm 0.0936	22.0 \pm 0.0
StronglyEntanglingLayers-10	0.9727 \pm 0.0066	0.0945 \pm 0.0945	60.0 \pm 0.0
SimplifiedTwoDesign-60	0.9626 \pm 0.0444	0.0955 \pm 0.0955	122.0 \pm 0.0
SimplifiedTwoDesign-9	0.9613 \pm 0.0134	0.1118 \pm 0.1118	20.0 \pm 0.0
RRQNN-40-2q	0.9608 \pm 0.0192	0.1109 \pm 0.1109	27.0 \pm 1.89
StronglyEntanglingLayers-9	0.9584 \pm 0.0115	0.1165 \pm 0.1165	54.0 \pm 0.0
MLP500-500-ReLU	0.955 \pm 0.0119	0.1145 \pm 0.1145	252501.0 \pm 0.0
RRQNN-20-1q	0.954 \pm 0.0099	0.1227 \pm 0.1227	12.2 \pm 1.48
BasicEntanglerLayers-10	0.9535 \pm 0.0149	0.1229 \pm 0.1229	20.0 \pm 0.0
StronglyEntanglingLayers-7	0.944 \pm 0.0157	0.1351 \pm 0.1351	42.0 \pm 0.0
BasicEntanglerLayers-9	0.9405 \pm 0.0314	0.1366 \pm 0.1366	18.0 \pm 0.0
SimplifiedTwoDesign-7	0.9344 \pm 0.0333	0.1436 \pm 0.1436	16.0 \pm 0.0
BasicEntanglerLayers-7	0.9219 \pm 0.039	0.1565 \pm 0.1565	14.0 \pm 0.0
RRQNN-20-2q	0.913 \pm 0.0379	0.1664 \pm 0.1664	13.4 \pm 0.84
SimplifiedTwoDesign-6	0.8919 \pm 0.0066	0.1892 \pm 0.1892	14.0 \pm 0.0
SimplifiedTwoDesign-5	0.8909 \pm 0.0003	0.1902 \pm 0.1902	12.0 \pm 0.0
StronglyEntanglingLayers-6	0.8624 \pm 0.0234	0.213 \pm 0.213	36.0 \pm 0.0
BasicEntanglerLayers-6	0.8174 \pm 0.1059	0.238 \pm 0.238	12.0 \pm 0.0
MLP100-100-ReLU	0.805 \pm 0.0124	0.2186 \pm 0.2186	10501.0 \pm 0.0
BasicEntanglerLayers-5	0.7754 \pm 0.1279	0.2625 \pm 0.2625	10.0 \pm 0.0
StronglyEntanglingLayers-5	0.7724 \pm 0.0148	0.2746 \pm 0.2746	30.0 \pm 0.0
RRQNN-10-1q	0.77 \pm 0.0339	0.2754 \pm 0.2754	5.4 \pm 0.7
StronglyEntanglingLayers-4	0.724 \pm 0.0002	0.3026 \pm 0.3026	24.0 \pm 0.0
RRQNN-5-1q	0.7234 \pm 0.0007	0.3029 \pm 0.3029	2.8 \pm 0.42
SimplifiedTwoDesign-3	0.6336 \pm 0.0002	0.3486 \pm 0.3486	8.0 \pm 0.0
BasicEntanglerLayers-3	0.6336 \pm 0.0002	0.3486 \pm 0.3486	6.0 \pm 0.0
BasicEntanglerLayers-4	0.6334 \pm 0.0002	0.3487 \pm 0.3487	8.0 \pm 0.0
SimplifiedTwoDesign-4	0.6195 \pm 0.0443	0.3548 \pm 0.3548	10.0 \pm 0.0
SimplifiedTwoDesign-2	0.1699 \pm 0.1466	0.5229 \pm 0.5229	6.0 \pm 0.0
SVR-linear	-inf \pm inf	0.6391 \pm 0.6391	2.0 \pm 0.0
MLP100-100-Id	-inf \pm inf	0.5818 \pm 0.5818	10501.0 \pm 0.0
MLP500-500-Id	-inf \pm inf	0.5809 \pm 0.5809	252501.0 \pm 0.0
MLP500-1d	-inf \pm inf	0.5778 \pm 0.5778	2001.0 \pm 0.0
StronglyEntanglingLayers-1	-7.4063 \pm 0.0	1.6698 \pm 1.6698	6.0 \pm 0.0
MLP100-1d	-65.5222 \pm 12.3134	0.5809 \pm 0.5809	401.0 \pm 0.0
MLP100-ReLU	-4.419 \pm 0.1903	0.4795 \pm 0.4795	401.0 \pm 0.0
SVR-poly	-1.1102 \pm 0.1002	0.4851 \pm 0.4851	2186.8 \pm 34.37
SVR-sigmoid	-0.0606 \pm 0.0145	75.8234 \pm 75.8234	3346.2 \pm 2.57
MLP500-ReLU	-0.0182 \pm 0.101	0.3437 \pm 0.3437	2001.0 \pm 0.0
BasicEntanglerLayers-2	-0.0004 \pm 0.0004	0.576 \pm 0.576	4.0 \pm 0.0
StronglyEntanglingLayers-3	-0.0004 \pm 0.0004	0.576 \pm 0.576	18.0 \pm 0.0
StronglyEntanglingLayers-2	-0.0002 \pm 0.0002	0.576 \pm 0.576	12.0 \pm 0.0
BasicEntanglerLayers-1	-0.0002 \pm 0.0002	0.576 \pm 0.576	2.0 \pm 0.0
SimplifiedTwoDesign-1	-0.0002 \pm 0.0002	0.576 \pm 0.576	4.0 \pm 0.0

Table B23 Results of the benchmark Function 22

# Param	Clustering Algorithm	ARI	Silhouette	Jaccard	Fowlkes–Mallows
5	KMeans(n_clusters=22)	0.027	0.214	0.028	0.069
5	Birch(n_clusters=22)	0.036	0.207	0.012	0.078
5	AgglomerativeClustering(n=22)	0.041	0.221	0.029	0.083
10	KMeans(n_clusters=22)	0.025	0.107	0.017	0.067
10	Birch(n_clusters=22)	0.012	0.102	0.018	0.054
10	AgglomerativeClustering(n=22)	0.011	0.106	0.020	0.054
20	KMeans(n_clusters=22)	-0.002	0.042	0.012	0.043
20	Birch(n_clusters=22)	-0.004	0.057	0.029	0.041
20	AgglomerativeClustering(n=22)	-0.004	0.057	0.029	0.041
40	KMeans(n_clusters=22)	0.006	0.015	0.024	0.049
40	Birch(n_clusters=22)	0.010	0.025	0.030	0.054
40	AgglomerativeClustering(n=22)	0.010	0.025	0.030	0.054
60	KMeans(n_clusters=22)	0.011	0.004	0.020	0.054
60	Birch(n_clusters=22)	-0.000	0.025	0.027	0.043
60	AgglomerativeClustering(n=22)	-0.003	0.022	0.014	0.041
120	KMeans(n_clusters=22)	-0.001	-0.006	0.025	0.047
120	Birch(n_clusters=22)	-0.000	0.016	0.023	0.043
120	AgglomerativeClustering(n=22)	-0.000	0.016	0.023	0.043

Table C24 RRQNN - 1q - Clustering metrics for different RRQNN parameter counts and clustering algorithms.

# Param	Clustering Algorithm	ARI	Silhouette	Jaccard	Fowlkes–Mallows
5	KMeans(n_clusters=22)	0.027	0.214	0.028	0.069
5	Birch(n_clusters=22)	0.036	0.207	0.012	0.078
5	AgglomerativeClustering(n=22)	0.041	0.221	0.029	0.083
10	KMeans(n_clusters=22)	0.025	0.107	0.017	0.067
10	Birch(n_clusters=22)	0.012	0.102	0.018	0.054
10	AgglomerativeClustering(n=22)	0.011	0.106	0.020	0.054
20	KMeans(n_clusters=22)	-0.002	0.042	0.012	0.043
20	Birch(n_clusters=22)	-0.004	0.057	0.029	0.041
20	AgglomerativeClustering(n=22)	-0.004	0.057	0.029	0.041
40	KMeans(n_clusters=22)	0.006	0.015	0.024	0.049
40	Birch(n_clusters=22)	0.010	0.025	0.030	0.054
40	AgglomerativeClustering(n=22)	0.010	0.025	0.030	0.054
60	KMeans(n_clusters=22)	0.011	0.004	0.020	0.054
60	Birch(n_clusters=22)	-0.000	0.025	0.027	0.043
60	AgglomerativeClustering(n=22)	-0.003	0.022	0.014	0.041
120	KMeans(n_clusters=22)	-0.001	-0.006	0.025	0.047
120	Birch(n_clusters=22)	-0.000	0.016	0.023	0.043
120	AgglomerativeClustering(n=22)	-0.000	0.016	0.023	0.043

Table C25 RRQNN - 1q - Clustering metrics for different operator counts and algorithms - considering binarized architecture vectors.

# Param	Clustering Algorithm	ARI	Silhouette	Jaccard	Fowlkes–Mallows
20	KMeans(n_clusters=22)	0.000	0.040	0.031	0.047
20	Birch(n_clusters=22)	0.010	0.051	0.018	0.053
20	AgglomerativeClustering(n=22)	0.009	0.054	0.027	0.052
40	KMeans(n_clusters=22)	-0.008	-0.003	0.008	0.040
40	Birch(n_clusters=22)	0.008	0.029	0.019	0.052
40	AgglomerativeClustering(n=22)	0.008	0.029	0.019	0.052
60	KMeans(n_clusters=22)	0.009	0.004	0.028	0.052
60	Birch(n_clusters=22)	0.008	0.023	0.023	0.052
60	AgglomerativeClustering(n=22)	0.008	0.023	0.023	0.052
120	KMeans(n_clusters=22)	0.004	-0.009	0.025	0.051
120	Birch(n_clusters=22)	0.003	0.017	0.012	0.047
120	AgglomerativeClustering(n=22)	0.003	0.017	0.012	0.047

Table C26 RRQNN - 2q - Clustering metrics for different operator counts and algorithms.

# Param	Clustering Algorithm	ARI	Silhouette	Jaccard	Fowlkes–Mallows
20	KMeans(n_clusters=22)	0.001	0.042	0.015	0.046
20	Birch(n_clusters=22)	0.005	0.052	0.030	0.048
20	AgglomerativeClustering(n=22)	0.002	0.052	0.025	0.045
40	KMeans(n_clusters=22)	-0.003	0.015	0.024	0.044
40	Birch(n_clusters=22)	0.008	0.026	0.023	0.053
40	AgglomerativeClustering(n=22)	0.008	0.026	0.023	0.053
60	KMeans(n_clusters=22)	0.016	0.002	0.010	0.065
60	Birch(n_clusters=22)	0.006	0.018	0.024	0.051
60	AgglomerativeClustering(n=22)	0.006	0.018	0.024	0.051
120	KMeans(n_clusters=22)	-0.001	-0.003	0.010	0.051
120	Birch(n_clusters=22)	0.003	0.011	0.019	0.047
120	AgglomerativeClustering(n=22)	0.008	0.015	0.019	0.052

Table C27 RRQNN - 2q - Clustering metrics for different operator counts and algorithms - considering binarized architecture vectors.

Function Number	Quantum Model	Classical Model	p-value
1	StronglyEntanglingLayers-20	knn4	0.375
1	StronglyEntanglingLayers-20	knn3	0.557
1	StronglyEntanglingLayers-40	knn3	0.064
2	StronglyEntanglingLayers-20	MLP500-500-ReLU	0.064
2	StronglyEntanglingLayers-60	knn4	0.375
2	StronglyEntanglingLayers-60	knn3	0.557
2	StronglyEntanglingLayers-60	MLP500-500-ReLU	0.232
2	SimplifiedTwoDesign-40	knn4	0.105
2	SimplifiedTwoDesign-40	knn3	0.105
2	StronglyEntanglingLayers-40	knn4	0.492
2	StronglyEntanglingLayers-40	knn3	0.846
2	StronglyEntanglingLayers-40	MLP500-500-ReLU	0.492
2	SimplifiedTwoDesign-20	knn4	0.432
2	SimplifiedTwoDesign-20	knn3	0.432
2	SimplifiedTwoDesign-20	MLP500-500-ReLU	0.922
4	SimplifiedTwoDesign-40	MLP500-500-ReLU	0.084
4	StronglyEntanglingLayers-40	knn4	0.084
4	StronglyEntanglingLayers-40	knn3	0.322
4	SimplifiedTwoDesign-20	knn4	0.322
4	SimplifiedTwoDesign-20	knn3	0.193
4	SimplifiedTwoDesign-20	MLP500-500-ReLU	0.922
5	StronglyEntanglingLayers-20	knn2	0.193
5	StronglyEntanglingLayers-60	knn4	0.432
5	StronglyEntanglingLayers-60	knn3	0.432
5	SimplifiedTwoDesign-40	knn4	0.160
5	SimplifiedTwoDesign-40	knn3	0.131
5	SimplifiedTwoDesign-40	knn2	0.625
5	SimplifiedTwoDesign-20	knn4	0.846
5	SimplifiedTwoDesign-20	knn3	0.770
5	SimplifiedTwoDesign-20	knn2	0.375
6	StronglyEntanglingLayers-60	knn2	0.232
6	RRQNN-120-2q	knn2	0.193
6	StronglyEntanglingLayers-40	DT	0.232
6	StronglyEntanglingLayers-40	knn2	0.770
11	StronglyEntanglingLayers-20	DT	0.131
11	StronglyEntanglingLayers-9	DT	0.322
11	StronglyEntanglingLayers-10	DT	0.375
11	StronglyEntanglingLayers-7	DT	0.322
11	SimplifiedTwoDesign-10	DT	0.275
11	StronglyEntanglingLayers-5	DT	0.105
11	SimplifiedTwoDesign-7	DT	0.160
11	StronglyEntanglingLayers-6	DT	0.160
11	SimplifiedTwoDesign-6	DT	0.131
11	SimplifiedTwoDesign-9	DT	0.232
11	SimplifiedTwoDesign-20	DT	0.160
16	SimplifiedTwoDesign-60	knn4	0.193
16	SimplifiedTwoDesign-60	knn3	0.064

Table D28 Wilcoxon signed-rank test p-values comparing quantum and classical models for selected CEC2020 functions.